NUREG/CR-3025
SAND82-2477
R7
Printed August 1984

High-Pressure Melt Streaming (HiPS) Program Plan

W. Tarbell, J. Brockmann, M. Pilch

Prepared by
Sandia National Laboratories
Albuquerque, New Mexico 87185 and Livermore, California 94550
for the United States Department of Energy
under Contract DE-AC04-76DP00789

Prepared for
U. S. NUCLEAR REGULATORY COMMISSION

Available from

GPO Sales Program
Division of Technical Information and Document Control
U.S. Nuclear Regulatory Commission
Washington, D.C. 20555

and

National Technical Information Service
Springfield, Virginia 22161

SAND82-2477

NUREG/CR-3025

R7

HIGH-PRESSURE MELT STREAMING (HIPS) PROGRAM PLAN

W. Tarbell
J. Brockmann
M. Pilch

Sandia National Laboratories
Albuquerque, NM 87185

1984

ABSTRACT

The Zion Probabilistic Safety Study (ZPSS) envisions accident sequences that could lead to failure of the reactor vessel while the primary system is pressurized. The resulting ejection of molten core material into the reactor cavity followed by the blowdown of steam and hydrogen is shown to cause the debris to enter into the containment region.

The High Pressure Melt Streaming (HIPS) program has been developed to provide an experimental and analytical investigation of the scenario described above. One-tenth linear scale models of the Zion cavity region will be used to investigate the debris dispersal phenomena. Smaller-scale experiments (SPIT-tests) are also used to study high-velocity jets, jet-water interactions, and 1/20th scale cavity geometries. Both matrices are developed using a factorial design approach.

The document describes certain aspects of the ZPSS ex-vessel phenomena, the experimental matrices, test equipment, and instrumentation, and the program's analytical efforts. Preliminary data from SPIT testing are included.

TABLE OF CONTENTS

LIST OF FIGURES

LIST OF FIGURES CONT.

LIST OF TABLES

LIST OF TABLES CONT.

I. Introduction

Until the late 1970's the WASH-1400 Reactor Safety Study (RSS) (Ref. 1) represented the most thorough analysis of reactor safety ever conducted. The report demonstrated the use of event tree analysis to show the relationship between the sequence of events and the consequence of each. A number of critiques have judged the basic methodology to be sound for application to other plants (Refs. 2 and 3).

Since the publication of the RSS, the Nuclear Regulatory Commission has explored ways of applying probabilistic risk assessments (PRA) to specific nuclear power plants. The key product of these analyses is a quantification of the risk to the public in operating the plant. The intent is to provide a clear indication of the events and equipment contributing to the risk and thus provide a means for assessing actions designed to reduce the risk.

A PRA involves the identification of the events and sequence of events conceptionally possible during an accident. Each of these events is quantified in terms of frequency of occurrence during plant operation. Contained within the quantification process is the determination of the uncertainty associated with the assigned values. Sophisticated mathematical techniques are then employed to develop the risk associated with each accident.

This report is organized into eight sections: Section I provides a general review of the Zion Probabilistic Safety Study (ZPSS) (Ref 4) and the objectives of the HIPS Program, Section II reviews the major ex-vessel events and analyses as given in the ZPSS, Section III contains a discussion of other phenomena that may be important to the ex-vessel events, and Section IV is the scaling analysis used to design the HIPS experiments. Section V presents the test matrices for the HIPS experiments and the smaller scale SPIT tests. Sections VI and VII give detailed descriptions and analysis of the SPIT and HIPS equipment and test techniques. Section VIII concludes the report.

Very little is presently known about the phenomena involved in high-pressure melt ejection accident scenarios. It is anticipated that the combined experimental and analytical work undertaken in the HIPS program will likely cause the direction and scope of the effort to be altered. This document attempts to consider all aspects of the problem to avoid large scale changes.

I.1 Zion Probalistic Safety Study

The ZPSS was performed primarily in response to the NRC's perception that sites near high-population centers create unusual and excessive risk. This perception resulted principally from the transfer of the base PWR case of the RSS analysis to a high-population location. The stated objectives of the ZPSS are: quantify the risk of the Zion plant as constituted and operated, identify the key contributors to risk, and evaluate the potential risk reduction if alternate features are considered.

The study considers three primary areas: the plant, its containment, and the site. The ZPSS develops a set of scenarios for each of these areas and matches the resulting sequence to achieve outputs. The outputs are then used to develop a quantitative assessment of risk. The goal is to assemble the analyses into a set of risk curves representing each of the identified health effects (early fatalities, thyroid cancers, man-rems, etc.). Each curve then gives the frequency of exceeding a prescribed level of damage.

The ZPSS is the result of an extensive analysis development and evaluation effort. The authors of the document believe that it advances the state of the art in the probabilistic risk assessment in several areas beyond the basis provided by the RSS. In particular, the development and quantification of the containment event tree recognizes differences in the response of the system to different core melt scenarios. The study also shows that the uncertainty in the fission product source term is the major contributor to the uncertainty in the risk analysis.

The RSS identified a number of initiating events that would cause loss of coolant and result in heating and possible melting of the core. The assumption was made that the degradation of the core structure proceeds uniformly to give a molten pool in the lower plenum of the reactor pressure vessel. The highest probability event was assumed to be loss of system pressure (large break LOCA) and eventual thermal weakening of the lower head, ultimately causing a "hinge-type" failure. With the failure of the vessel, the molten core material pours into the cavity under the acceleration of gravity. The study did identify other failures that could occur while the system was at elevated pressure, but the results of these sequences did not significantly deviate from the large-break LOCA behavior. A key feature of the RSS is that containment failure can be caused by steam explosion or missile generation. If these mechanisms do not cause failure, then the long-term core/concrete interaction or the hydrogen gas burning will eventually overpressurize the containment or penetration of the basemat structure will occur. The analysis suggests a very low probability that the accident will terminate short of containment failure.

The ZPSS recognized several differences from the RSS in the key phenomena associated with the events leading to vessel failure. Detailed analysis of the core melt progression showed that coherent downward movement of large quantities of molten core material is unlikely. This conclusion results in a probability of 0.9 that less than 25% of the melted core will be in the lower plenum early in the accident. The analyses also recognize that core degradation (incoherent melting) can occur for transient and small-break LOCA sequences where the primary system will be at elevated pressure.

Failure of the vessel by steam explosion or by overpressurization is assumed to be physically unrealizable with a very low frequency of occurrence. The ZPSS conservatively estimates a probability of 0.1, that the accident will be terminated by in-vessel cooling of the core debris. Without permanent cooling, the debris will attack and fail the weld of one or more instrumentation tube penetrations in the lower head of the vessel. The loss of weld integrity causes the tube to slip out of the lower head and the molten debris to be ejected under pressure into the reactor cavity.

If the accident proceeds to the point where molten core material is ejected under pressure into the cavity, the ZPSS predicts the material will be "dispersed" into the containment building. The analysis considers that the wide distribution of the material, combined with the availability of water, assures that the configuration is coolable. By minimizing concrete attack and consequently gas release, the probability for the loss of containment integrity is considered low.

The ZPSS containment event tree is comprised of 19 nodes or branch points chosen in an iterative process during which the principal phenomena affecting containment integrity are addressed. Each node represents a decision characterized by a "yes-no" input. Probabilities assigned to each of the branches are included in the determination of the ultimate risk associated with the paths emanating from the branch. The probability of each node is conditional on preceding events, including the input plant state. The resulting event tree is comprised of 2^{19} (524,288) output nodes. During the analysis, many of the branches were removed (pared) as being "technically illogical" for the path followed. After the "paring" process, the containment event tree is reduced to a total of 1050 output nodes.

In order to disperse the core debris, the ZPSS proposes a number of hydrodynamic mechanisms induced by the blowdown of the primary system. The principal driving force is the energy provided by the high-pressure jet of steam and hydrogen from the primary system following the ejection of the core material. Establishing the existence of the dispersal mechanism is essential in verifying the calculated risk factors.

I.2 HIPS Program Objectives

The HIPS program is an experimental and analytical investigation of the phenomena associated with the behavior of molten core debris streaming into reactor cavity configurations. The experiments will involve high-temperature melts created at realistic pressure levels and injected into scaled reactor cavity geometries. The objectives of the HIPS program are as follows:

1. Confirm the existence of the debris dispersal mechanism.

2. Determine and assess other melt jet phenomena such as jet geometry, gas solubility, and aerosol generation.

3. Assess events discounted in the ZPSS, such as melt/water interaction, energetic concrete decomposition, and the combined effect of one or more events.

4. Reduce uncertainty in probability estimates of the fission product source term and dispersal mechanism.

The ZPSS analysis is hampered by the lack of experimental information concerning the ejection and behavior of high-temperature materials in confined geometries. The first objective of the HIPS program is to experimentally confirm the debris dispersal mechanisms given in the ZPSS. Despite the lack of confirmatory information, the authors of the ZPSS have assigned a probability of Ø.9 with a range of Ø.8 to Ø.99 that material dispersal will occur (positive branch of the event tree at Node I). All sequences that proceed from the negative branch at Node I are assigned the "placekeeper" probability of Ø.ØØØ1, causing their calculated frequencies to be small and thus consideration of subsequent events is neglected.

If the probability of dispersal is shown experimentally to be lower than (Ø.9), then the values assigned the negative branches must be correspondingly increased. Higher frequencies for the negative, non-dispersed branch will then require consideration of the probability of a non-coolable debris bed configuration in the cavity and ultimately, overpressurization of containment from concrete decomposition. The HIPS tests are specifically directed to confirm the existence of material dispersal mechanisms, and to establish probability estimates for complete dispersal.

If the experimental results show that the material is completely dispersed, then the uncertainty associated with this node can be verified or reduced. Conversely, if no material exits the cavity region, the results can then be used directly to reassess the probabilities associated with the node branches. Partial dispersal cannot be treated in the same manner.

Because the ZPSS event tree is constructed of binary (yes-no only) decision points (nodes) a partial or incomplete dispersal of material is not directly considered in the node probability. If the experiments show that only partial dispersal occurs, the results of the HIPS tests can be used to suggest a probable outcome by applying the ZPSS "gravity-drop" analyses to the portion of material not removed.

The second objective of the HIPS program will be to identify damage modes other than the 19 possibilities in the ZPSS containment matrix. Failure to consider a damage mode may mean that paths at subsequent nodes in the analysis are not representative of the actual events. Partial dispersal of the debris is an example of this possibility. The exact yes-no decision logic used in the ZPSS does not account for situations where portions of the debris are not removed from the cavity.

Melt crust formation is not considered within the context of the 19 damage modes presented in the ZPSS. The analyses assumes that coolability is guaranteed during a Large-Break LOCA sequence. Formation of a stable crust over the dispersed debris that may prevent cooling, despite the presence of water. Limited experimental evidence exists (Ref. 5), to suggest that the formation of a stable crust of decomposed concrete could prevent coolant from reaching the lower portions of the debris bed.

The effect of melt aerosol is a third example of a possible event not considered in the ZPSS. Experiments reported here have shown that high-pressure melt ejection sequences are accompanied by large aerosol generation. In an accident, these aerosols will contain radioactive fission products that will enter into the containment atmosphere. The aerosols will also pose a threat to containment safety features because of their potentially high heat content and may diminish the effectiveness of heat transfer processes within containment. Sufficiently large concentrations of aerosols could ultimately eliminate containment heat removal capability.

The third objective of the HIPS program is to determine if ex-vessel phenomena neglected in the ZPSS are of consequence to the calculated risk. Specifically, the ZPSS ascertains that a water-filled cavity has no effect on the dispersal of debris during transient and small-break LOCA scenarios. The analysis assume that the water is "pushed" out of the cavity by a steam bubble formed by quenching the melt jet. A large number of assumptions are made in this analysis including: heat transfer between the melt and water is instantaneous, inteference of expansion waves does not occur, and steam generation is isothermal. Experimental evidence of these assumptions is not provided in the ZPSS.

The ZPSS analysis does not consider the effect of concrete decomposition or the debris removal mechanism. Numerous

experimental investigations (Refs. 6, 7) have shown that molten material contacting concrete is accompanied by vigorous gas generation and concrete spallation. As a consequence, the dynamic debris configuration envisioned in the ZPSS may not form and subsequent dispersal may not occur.

Within the context of identified, but neglected, phenomena is the combined effect of two or more phenomena. The ejection of the core material under pressure from the vessel will likely involve a simultaneous vessel blowdown (of steam/water/hydrogen), steam explosion, concrete decomposition, core debris quenching, and oxidation of Zirconium and iron. The ZPSS considers all of these phenomena separately except the possibility of oxidation in the cavity environment (100% Zr oxidation in-vessel is assumed).

The effects of chemical oxidation are threefold: (1) the oxidation of Zr and steel is an additional hydrogen source, (2) the heats of reaction cause additional pressurization, and (3) the particles may, act as a distributed hydrogen ignition source. These effects will combine to cause more hydrogen to be available than the ZPSS assumes and the likelihood of burning to be greater.

The fourth objective of the HIPS program is to reduce uncertainties in the ZPSS analyses. The largest source of uncertainty in the ZPSS analysis is identified as the radionuclide source term for the site matrix calculations. Both the RSS and ZPSS assume that the major portion of the fission product source term is in the form of fine particles generated during ex-vessel steam explosions. Concrete decomposition aerosols are assumed to contribute very little to the radioactive source term. Neither study identifies the possibility of aerosols formed during melt deposition. The HIPS program will address this area by including fission product mocks in the melt composition, studying the aerosol formation mechanism, and analyzing the behavior of the particulate material in the cavity region.

I.3 Scope of HIPS Program

The scope of the HIPS program considers the ex-vessel events occurring during the small-break LOCA and transient accident scenarios. The large-break LOCA or "gravity-drop" sequence does not involve gas-driven debris dispersal and is therefore not considered in the program. The in-vessel processes of fuel melting and vessel attack are assumed to occur in the manner outlined in the ZPSS. The single-tube failure assumption will be used as the starting point in initiating the experimental sequence.

Phenomena outside the cavity region are highly dependent on the details of the containment structure. The behavior of the debris, gas, and aerosols escaping the cavity will be monitored to assess their contribution to the containment loading. Decay heating and long-term coolability of the debris will not be included in the initial HIPS test matrix.

II. Review of ZPSS Ex-Vessel Analyses

A PRA such as the ZPSS involves an extensive analysis of the many processes and events that may occur during a postulated reactor accident. The resulting document is therefore highly involved and lengthy. This section presents a review of the parts of the ZPSS document pertinent to the sequence of events from vessel failure to final debris disposition. The intent is to provide a convenient basis for subsequent discussion. Following a brief description of the plant, the ordering is the same as that used in the ZPSS beginning with "Section 3.2, Accident Sequences."

II.1 Description of the Zion Reactor Plant

The two-unit Zion nuclear plant is located approximately 40 miles north of Chicago, Illinois, near Lake Michigan. Commercial service dates for the units are in December 1973 and September 1974 (Ref. 10). The nuclear-steam-supply system for each of the Zion units consists of a four-loop Westinghouse pressurized water reactor. Each reactor is rated at 3250 megawatts (thermal) and produces 1085 megawatts of electrical output.

Each reactor is housed in an individual containment building (Figure 1) consisting of a post-tensioned concrete shell over 1/4-inch-thick (6-mm) steel liner. The internal volume of the containment structures is approximately 77,000 cubic meters with a design pressure of 0.5 MPa (62 psia). The lower bound ultimate strength is estimated in Appendix 4.4.1 of the ZPSS to be 1.0 MPa (149 psia). The concrete consists of Portland-type cement incorporating limestone coarse aggregate and common-sand fine aggregate (Ref. 6).

The reactor pressure vessel (RPV) of each unit is placed in a cavity located in the floor of the containment building. The cavity allows access to the lower head of the RPV for instrumentation-tube placement. The access tunnel connects the cavity to the inclined "keyway" leading to the floor of the containment structure. Figure 2 gives two views of these features, showing the tapered cross-section of the access tunnel. Much of the in-containment equipment has been omitted from Figures 1 and 2 to improve clarity of the major features.

The ex-vessel interactions described later in this section are postulated to occur in the cavity, tunnel, keyway, and containment building. Figure 3 is a more detailed view of these areas showing the instrumentation tubes and sump pit. The 56 instrumentation tubes emanating from the RPV are arranged in a rectangular array that terminates in the cable seal room in the containment building. Not obvious in the figures is a continuous stainless-steel biological shield (6-mm thick) liner in the cavity and tunnel regions at a depth of 0.5 to 0.75 m below the concrete surface.

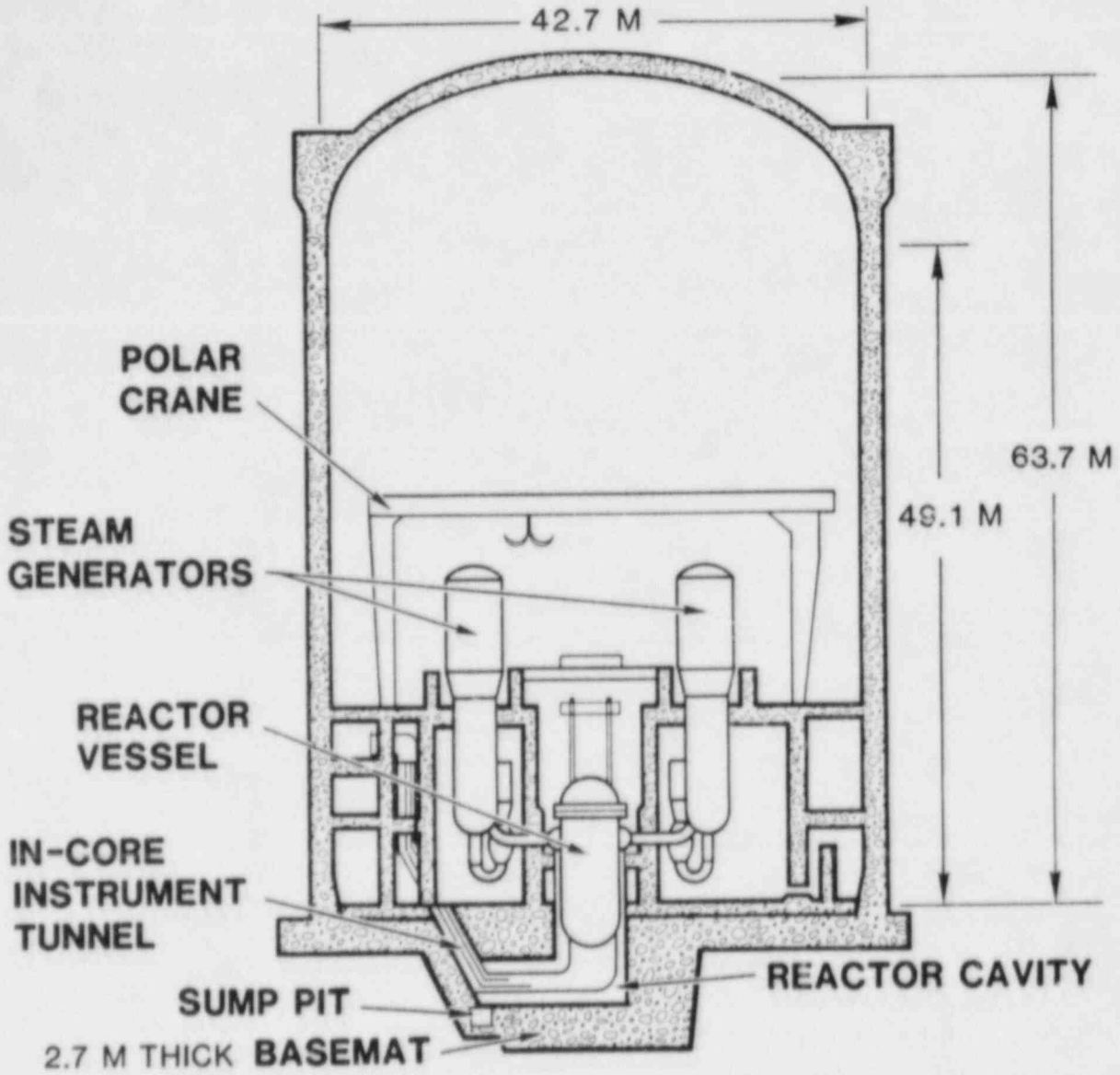

Figure 1. Schematic View ZION Reactor Containment Building

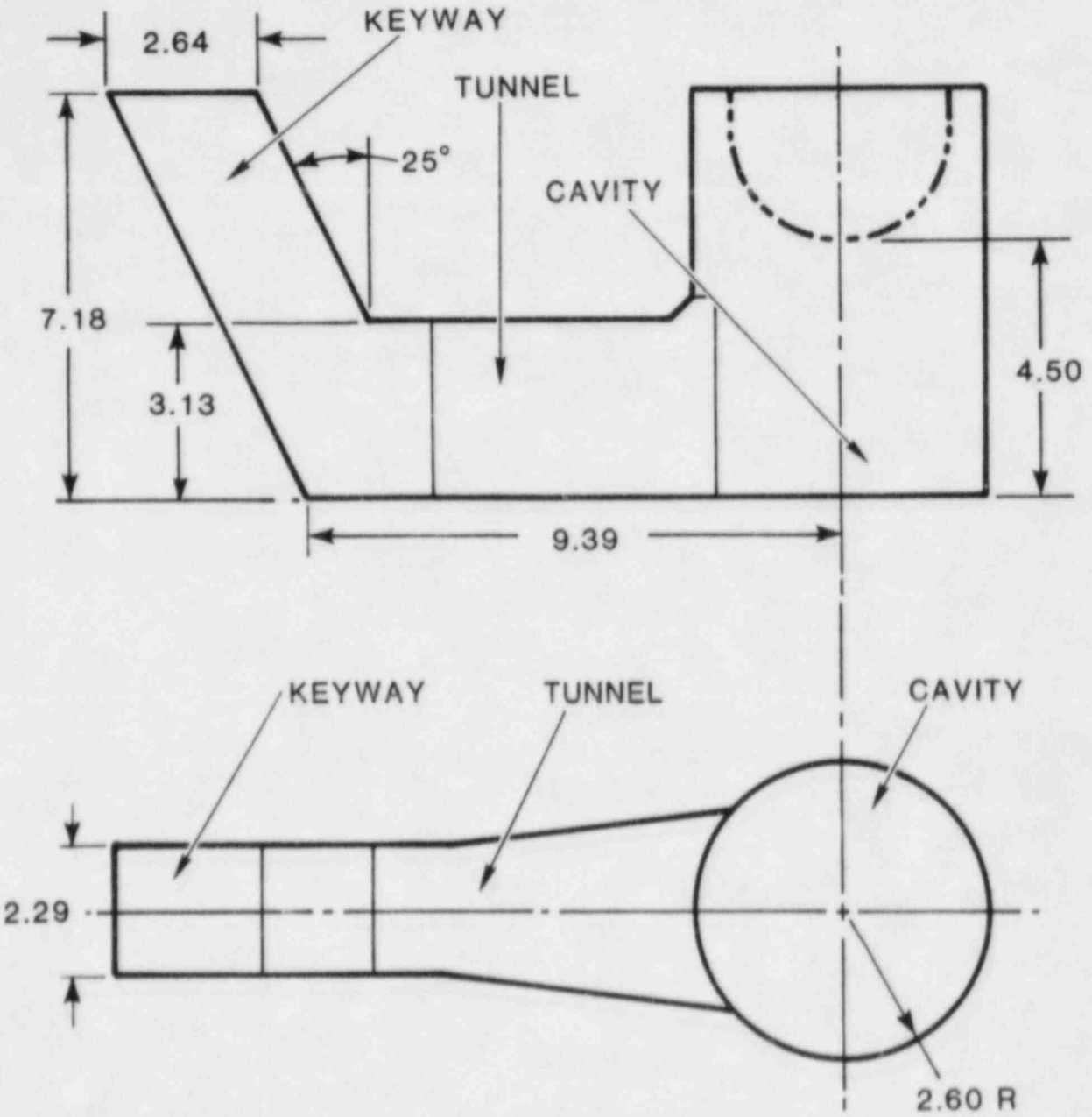

Figure 2. Plan View and Typical Dimensions of Zion Reactor Cavity
(Dimensions in Meters)

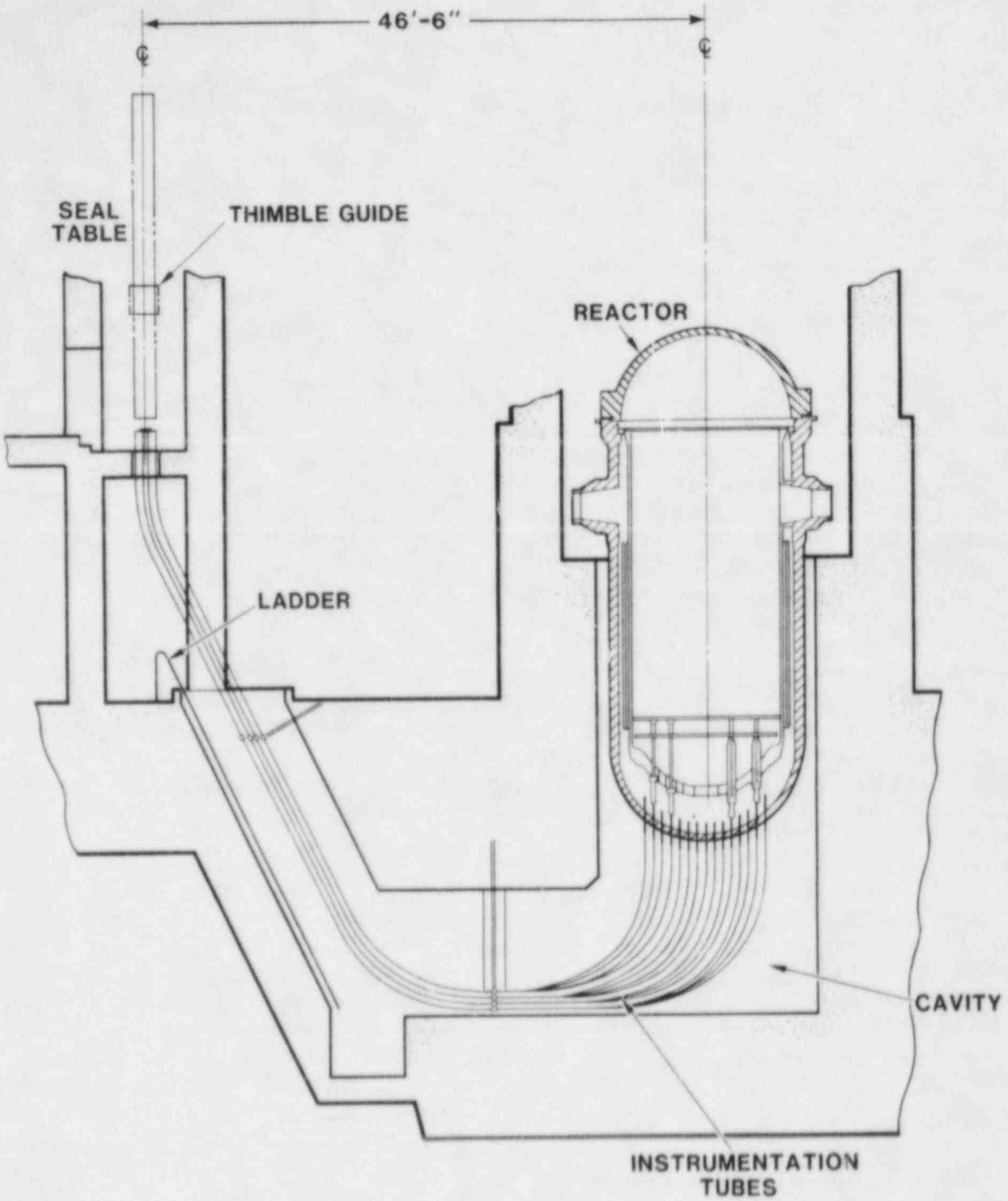

Figure 3. Details of ZION Reactor Cavity Region

II.2 Accident Sequences

The ZPSS considers a total of 68 accident-initiating events, that are assigned to one of 13 initiating event catagories in the event logic diagram. The sequence of events leading to degraded core scenarios are varied and depend on the initiating event and the operation or failure of plant safety systems. A common characteristic is the loss of coolant from the primary cooling system, causing overheating of the core.

In general, accidents are classified in one of three categories, depending upon the primary system pressure during the time of the accident. With one exception (interface LOCA), the sequences are: Large-Break LOCA (pressure < 1.4 MPa), small-break LOCA (pressure < 7 MPa), or transient events (up to the set-point of the pressurizer relief valves - 17 MPa) The ZPSS analysis recognizes differences in the behavior for the various classes of accidents, such as the timing of events, the amount of material involved, and the resulting interactions.

For the large-break LOCA sequence, a failure in the primary system is assumed to cause rapid depressurization allowing the primary system to discharge to an equilibrium condition with the containment atmosphere. Hydrogen generated by the oxidation of the core cladding is also released into the containment building. For this sequence, the ZPSS considers the primary system and containment building pressure following blowdown to be 0.3 MPa (44.1 psi).

The small-break LOCA sequence analysis assumes that the core is uncovered by loss of coolant through a smaller break. For this case, core degradation (loss of coherent structure) can occur while pressure exists within the primary system. The gas released through the break raises the containment atmospheric pressure slightly. The range of pressures in the primary system proposed in the ZPSS for this accident is 1.4 to 7.0 MPa (200 to 1029 psia) with the value of 7.0 MPa used for the calculations.

The transient event occurs when safety systems fail to respond to an accident-initiating event. In this situation, the system pressure and temperature continue to rise until the relief valves open. If sufficient coolant is lost through the valves, the core may become uncovered. The transient sequence results in exposure of the core at pressures close to system operating conditions. Pressures of 7.0 to 17.0 MPa (1029 to 2500 psia) are considered for this sequence. The upper limit corresponds to the set point of the pressurizer safety valves, and is used for the ZPSS analysis.

The three accident sequences result in two event chains in the transient analysis section of the ZPSS. A "Gravity Drop Model" is used for accidents where the system pressure is less than 1.4 MPa (large-break LOCA). In the analysis, the release

rate of core material into containment is related to the static head of molten material in the vessel. This treatment parallels that associated with the lower head failure given in the WASH-1400 analysis. The second event chain, the "Time-Phased Dispersive Model" is used where the primary system pressure is above 1.4 MPa. The sequence of events and their relative time scales characterize the small-break LOCA and transient events. In general, the model considers the high-velocity gas/melt stream exiting the RPV breach, combined with the steam/hydrogen blowdown, has a significant affect on the final debris configuration and distribution.

II.3 Vessel Failure

The onset of vessel failure represents the culmination of the in-vessel events and the entry state leading to the ex-vessel interactions. The ZPSS finds that portions of the core will melt causing material to fall or flow into the reactor vessel's lower plenum. If the supply of coolant to this region is inadequate, the large thermal energy of the core mass will cause attack of the vessel's steel wall. Internal structures such as the lower core support and the in-core instrumentation supports may also be attacked.

The ZPSS theorizes that molten core material entering into the lower plenum region immediately begins to attack the vessel wall. Any existing water will be vaporized or displaced by the core debris and additional water will vaporize off the upper debris surface. In order to consider the range of possible system characteristics, the ZPSS analysis considers a range of variables including: system pressure levels of 0.1, 7.0 and 17.0 MPa, heat fluxes on the inside surface of the vessel of 315 and 630 kW/m^2 (100,000 and 200,000 $B/hr-ft^2$), and three separate debris accumulation scenarios. Two types of failure modes are identified; the first considers the partial penetration welds retaining the instrumentation tubes (Figure 4) that fail when the temperature of the weld material exceeds 1100°C (2000°F). The force exerted by the static debris head and the system pressure (if present) causes the tube to "slip out" of the vessel head.

The second failure sequence occurs when a portion of the vessel head wall is heated to a temperature above 1100°C (2000°F) causing a plastic flow zone to emanate horizontally from the weakest location along a circumferential line around the bottom head. The wall begins to tear along this line from the weakest point and causes the head to "hinge" downward as the tear progresses.

The ZPSS analysis finds that the molten core material will be uniformly distributed in the vessel head. The authors of the ZPSS point out that a uniform distribution is unlikely due to the influence of non-coherent melting and the core support structures.

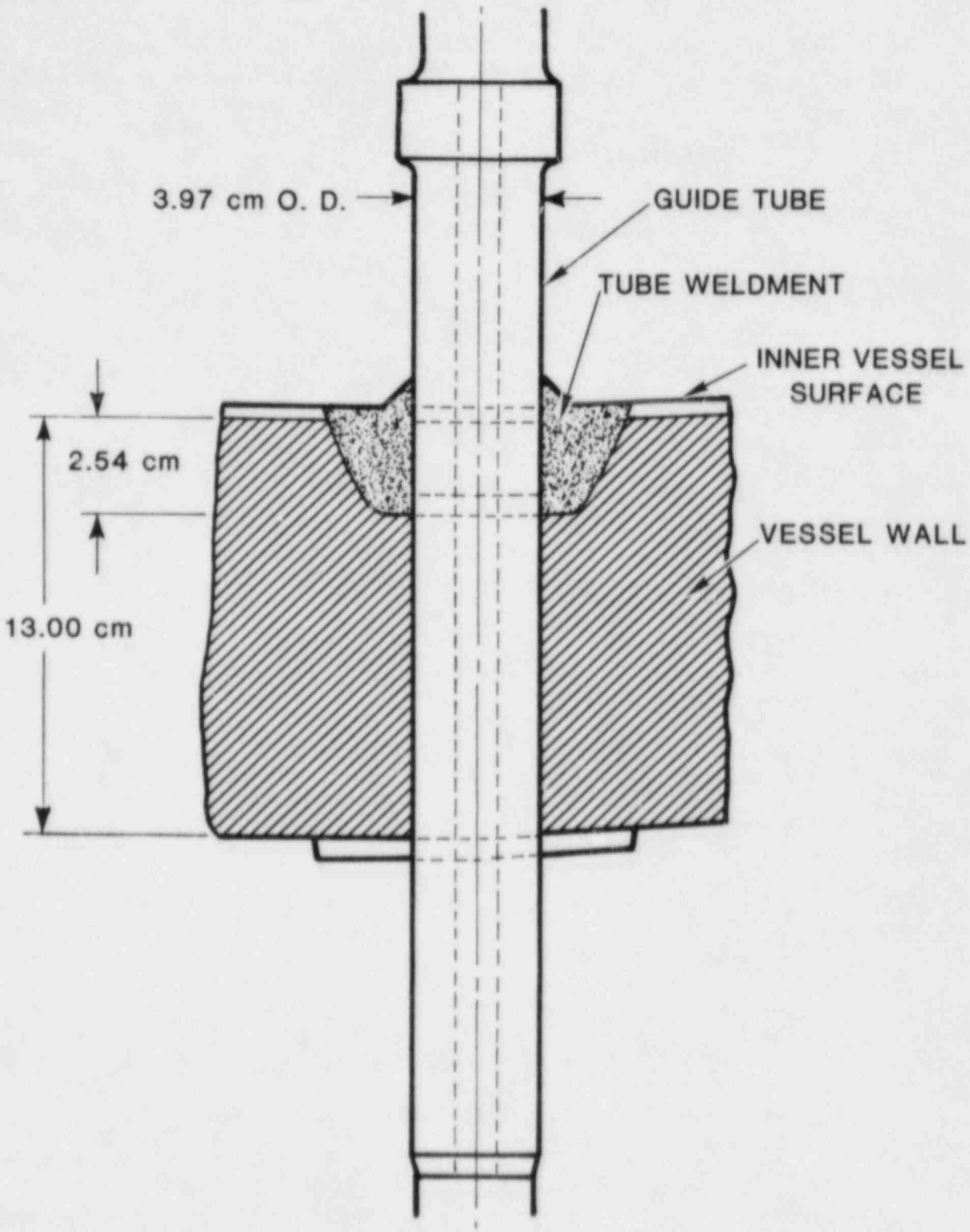

Figure 4. Instrumentation Nozzel - Vessel Weld

They further state that their expectation is that the core material will accumulate primarily in the central portion of the plenum region. The combination of core debris accumulation in the central region, the thickness of the partial penetration welds (relative to the head-thickness), and the shear stress loading on the welds will result in the failure of one or more instrument tubes long before other vessel failures can occur. Thus, the instrumentation tubes provide the principal manner and location for vessel failure.

In the eighteen cases analyzed, all but one showed "tube penetration" failures to occur. In twelve cases, only the instrumentation tubes fail, with the debris dispersed through the holes created by the tube ejection. In four other cases, tube ejection is followed by bottom head failure. For these latter cases, debris is lost through a combination of the holes in the head and the tear in one side of the vessel. In the one remaining case, bottom failure precedes tube failure.

A failed in-core instrumentation tube will cause an initial vessel breach 4 cm in diameter. The ZPSS analysis indicates that the heat flux of the flowing core debris will be sufficient to cause additional melting of the steel structure surrounding the breach. As a result of the ablation process, the available flow area of the breach will increase substantially during the period of discharge. For the sequences considered, the final breach size is assumed to be approximately 40 cm.

II.4 Jet-Stream Configuration

The ZPSS does not give a detailed description of the configuration of the jet stream emanating from the breach in the reactor pressure vessel. The analysis predicts that the jet will be composed of completely liquid core material with a diameter equivalent to the breach dimension. Additionally, the stream does not expand from the point of discharge till contact with the cavity floor. Bernoulli's equation is used to calculate the stream velocity with values of 70 m/sec for the transient sequence (17.0 MPa), 42 m/sec for the small-break LOCA (7.0 MPa) and 3 m/sec for the depressurized, large-break LOCA case.

II.5 Ex-Vessel Melt/Water Interactions

The design of the Zion plant will cause, in general, an accumulation of water in the reactor cavity during accident sequences. The amount of water accumulated is dependent on a number of circumstances during the accident such as the size of the break in the primary system (if any) and the availability or use of engineered safety systems. Conceivably, the extent of the water pool can range from a dry to a fully-filled cavity region. The ZPSS surmises that knowing the exact amount of water is not

necessary. It is only required to know if a "substantial amount" of water exists below the reactor vessel. Calculations are presented in the ZPSS for a fully-filled cavity and also a water depth of 0.5 m (6400 gal) for the partially-filled cavity case. The former is discussed in Section II.10.

The ZPSS cites several references to establish that a steam explosion will occur when the melt stream exits the RPV, penetrates the pool, and contacts the cavity floor. The amount of melt in the water at the time of floor contact is calculated to be approximately 7 kg for all partially-filled cases (0.5-m water depth). The interaction of this quantity of material with the water results in mechanical work (water vapor expansion) of negligible consequence to the containment integrity. The interaction may displace the water and a portion of the debris from the cavity region. The ZPSS concludes that the major influence of the limited work will be on the detailed disposition of water and core debris in the lower regions of the containment building.

The dispersal of core debris and water out of the cavity will result in rapid quenching and steam production. It is assumed in the analysis that all core debris material outside the vessel at the time of the interaction is involved in the quenching process. For the sequence analyzed, this amounts to approximately 70 kg. Additional steaming will occur as more core material and additional water enter the cavity.

II.6 Jet-Concrete Interaction

In the dry cavity case or when displacement of the water pool occurs, the melt jet stream will impinge directly on the concrete basemat. The extent of concrete ablation is evaluated using the imposed heat flux of the jet. The heat flux is highest for the transient event (22,200 kW/m^2) because the convective heat transfer coefficient is proportional to the square root of the jet velocity. The coefficient is also inversely related to the diameter of the stream, but an average diameter is used in all calculations. The imposed heat flux is assumed to cause rapid heating and melting of the concrete surface.

The depth of melt jet erosion determined in the ZPSS analysis varies from 4 to 18 cm for the transient and large-break LOCA sequences, respectively. The longer duration of the melt discharged at the lower driving pressure (80 seconds versus 4 seconds), causes a larger depth in the latter case. The authors state that the analysis is conservative and overpredicts the extent of erosion because the heats of decomposition and heat of fusion of the concrete are neglected. Also, the concrete melting temperature is assumed to be 1100°C, representing a lower bound of the expected spectrum of melt temperatures.

The amount of concrete decomposed by the jet is assumed to be the volume of material represented by the product of twice the jet diameter (to allow reversal of the jet) multiplied by the calculated depth of erosion. The pressure rise due to the amount of non-condensable gas released is negligible compared to the total containment capacity.

II.7 Dynamic Configuration of Molten Core Debris

The ZPSS ascertains that material discharged from the vessel impinges as a high-velocity jet on the concrete cavity floor and spreads outward. Initially, the flow is radial, but then the influence of the cavity walls causes the material to be directed into the instrument tunnel. It is estimated that, for the transient sequence, a Ø.1-meter-deep flow on the cavity floor will achieve a maximum velocity of 17 m/sec upon entering the tunnel. The ZPSS finds that the high velocity of the flow will cause a "hydraulic jump" to occur somewhere in the instrument tunnel region. The jump is depicted as a transition from a high-velocity, low-head state to a low-velocity, high-static-head behavior. The calculations show the jump height to be relatively insensitive to the initial depth of the flow. The small-break LOCA and transient sequences demonstrate similar behavior. The wave amplitude in the large-break LOCA case is considerably diminished relative to the other sequences. The configuration of the debris following the "jump" is used in all subsequent analyses.

II.8 Core Debris Relocation

A unique aspect of the ZPSS analyses relative to previous PRA's is the assumption that the high-pressure discharge of steam and hydrogen from the primary system will strongly affect the final disposition of the core debris. Four hydrodynamic phenomena are proposed that can result in debris material deposition outside the reactor cavity. The mechanisms have been characterized as: particle levitation, film sweepout, film entrainment and splashout. These mechanisms are shown schematically in Figure 5 and are discussed in more detail in subsequent paragraphs. As a result of these mechanisms, the ZPSS containment model assumes that the degraded core material is removed from the cavity very shortly (on the order of one second) after the initiation of the gaseous discharge.

The large-break LOCA, however, does not produce a high-velocity gas discharge to disperse the material. Consequently, except for the material potentially displaced during a steam explosion, the core material will accumulate on the floor of the cavity and instrument tunnel during this sequence.

A. Particle Levitation

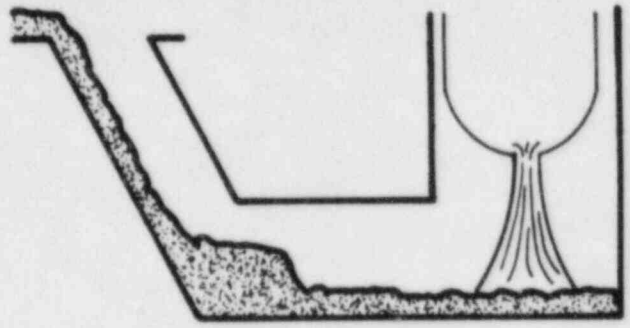

B. Film Sweepout

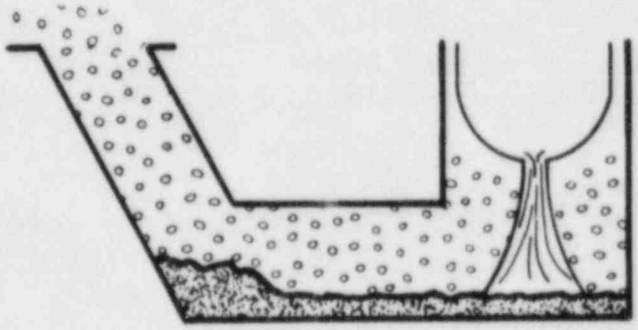

C. Film Entrainment

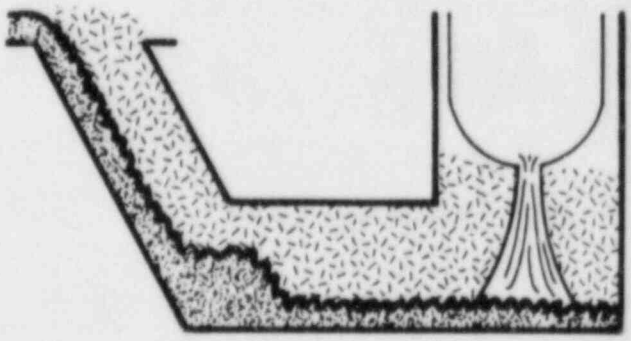

Figure 5. Material Removal Mechanisms

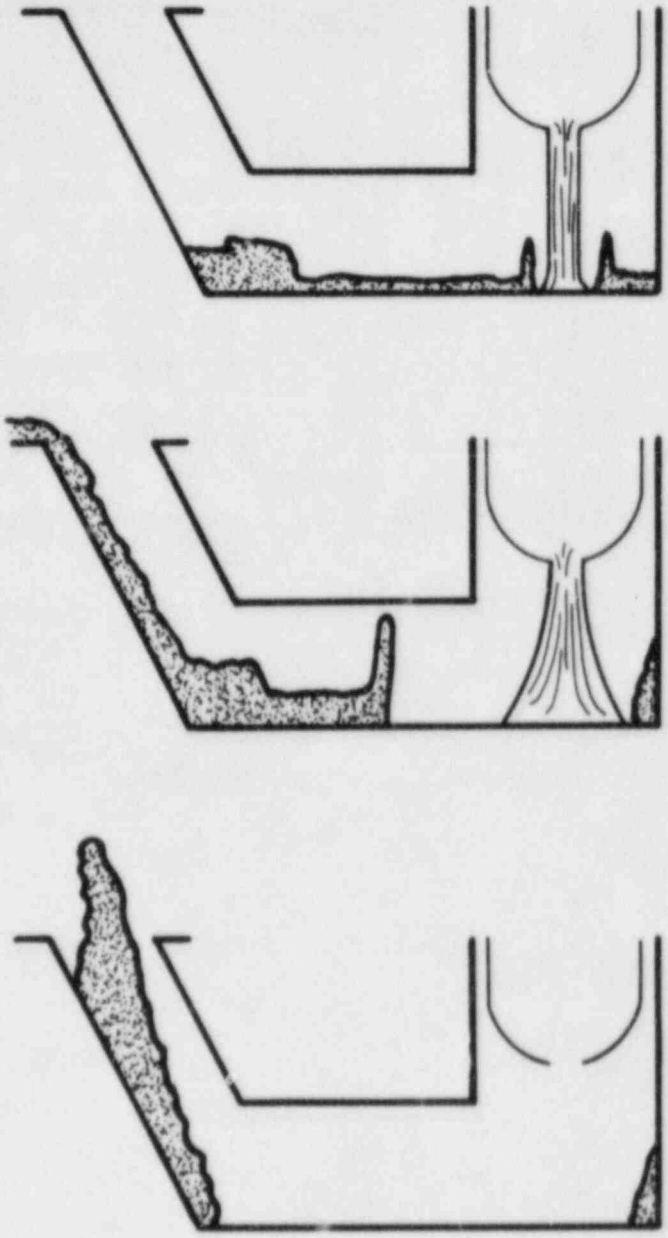

D. Splashout

Figure 5. (Continued)

II.8.1 Particle Levitation

Particle levitation occurs when the high-velocity gas mixture impinges on the surface of the melt pool causing the flow to stagnate and divert at right angles (Figure 5a). The downward pressure displaces the liquid to form a high-amplitude "ring" of melt material. The greatly distorted liquid surface combined with the high-velocity gas flow causes the ring to breakup and form particles. If the hydrodynamic drag force exceeds the gravity force, then particles can be entrained within the gas stream. The ZPSS analysis indicates that large particles (25-cm diameter in one example) can be entrained.

II.8.2 Film Sweepout

Film sweepout will occur when the hydrodynamic drag force exerted by gas blowing across the melt surface is greater than the surface tension of the degraded core material (Figure 5c). Small fragments of melt entrained in the gas stream are carried into the containment where they fall out of suspension as the gas slows.

II.8.3 Film Entrainment

Film entrainment arises when the gas stream causes waves on the melt pool surface. If amplitude of the wave crest is too large, erosion or breakup of the wave tip will occur and the fragments will be entrained in the stream (Figure 5c).

II.8.4 Splashout

Splashout occurs when the pressure exerted by the jet induces a radial movement at the base of the pool (Figure 5b). The movement may cause a major fraction of the degraded core material to be transported down the instrument tunnel to the upward sloping keyway. Velocities greater than 12 m/sec are needed to cause material to leave the tunnel region and enter the containment area. Calculations in the ZPSS give velocities of tens of meters per second under the conditions of small-break LOCA or transient accidents.

II.9 Debris Cooling on Containment Floor

The ZPSS assumes water (up to 15 cm deep) exists on the floor of the containment building when the degraded core material is dispersed from the reactor cavity. Large quantities of steam are produced as the debris material is quenched. A combination of localized steam explosions, normal water boiling processes, and radiation to the condensate on the walls and structures and

to the entrained water droplets will cause energy to be lost. The major influence of the steam explosions will be to disperse the water and core debris from the locality of the occurrence yielding a major relocation of the constituents around the containment floor. During the explosion process, a substantial amount of thermal energy is transferred from the melt to the water. The estimated energy extraction is about 3400 MW (time interval of 1 millisecond).

The fraction of the melt not participating in the steam explosions is assumed to be submerged in the water pool or have a line-of-sight path to airborne water droplets or to the containment structures covered by condensate. Based on the planer surface area of the containment inside the crane wall (700 m^2), the energy transfer rates by these mechanisms are estimated to range from 680 to 1900 MW/sec. These rates result in quenching times of 33 to 93 seconds for the small-break LOCA and transient cases, respectively. In all cases (except gravity-drop), the ZPSS finds that quenching will occur over an interval comparable to the blowdown of steam and hydrogen from the breach in the reactor vessel (i.e., less than a few tens-of-seconds).

II.10 Debris Interaction for a Water-Filled Cavity

In sequences where extended water injection occurs (with failure of recirculation), the reactor cavity and instrument tunnel could be filled with water. The discharge of core debris directly into the water results in substantial hydrodynamic fragmentation of the melt. The ZPSS model assumes that the core material is rapidly quenched to form a high-pressure steam bubble in the immediate vicinity of the vessel failure. The growth of the bubble causes compression waves in the water to initiate water movement away from the failure location. The release of degraded core materials from the pressure vessel is predicted to generate sufficient steam flow to extensively void the instrument tunnel before the high-pressure steam/hydrogen gas flow begins. The ZPSS concludes that the behavior of the water-filled cavity will essentially be the same as the fully-voided (dry) cases described in previous sections.

For the large-break LOCA sequence, the debris would penetrate the water and remain in the reactor cavity and quench at a rate governed by a critical-heat-flux limitation at the surface of the debris bed.

III. Alternative Ex-Vessel Accident Phenomena

Experimental evidence concerning some of the aspects of ex-vessel interactions was not available to the authors of the ZPSS at the time of the document's inception. Little is known about the discharge of dense molten material at high temperature and pressure. Most published reactor-safety analyses and experiments (Refs. 6 and 10) consider only interactions of gravity-driven melts with water or concrete. Therefore, experiments specifically designed to study a pressure-driven interaction scenario may identify other phenomena not recognized by the ZPSS analysis. The material in this section identifies potentially pertinent phenomena, primarily as an aid to developing a comprehensive test plan for the experimental programs.

III.1 Melt Temperature

The condition of the melt in the RPV directly affects the potential vessel failure modes and consequently the input conditions for the subsequent ex-vessel interactions. The ZPSS analysis for tube failure and thermal attack of the vessel structure does not explicitly indicate the melt temperature. The value can be inferred by reviewing the ZPSS plot of the non-dimensional parameters involved in the vessel attack (Fig. 3.1.7-2). Using 300°C and 1500°C for the initial and melting temperature of the pressure vessel, respectively, indicates that the core debris temperature is on the order of 2100°C. This value corresponds to that used in other sections of the report.

Catton of UCLA (Ref. 11) has proposed that the temperature of the degraded core material may, in fact, be just above the steel melting temperature. This opinion is based on the assumption that the energy required to melt the reactor internals, combined with the dilution of the fuel/clad mixture will cause the debris temperature to be depressed.

A lower debris temperature than assumed in the ZPSS will influence subsequent accident events. First, the reduced heat flux will cause the vessel attack to be slower than visualized in the ZPSS, lengthening the time to failure. The increase in time may then cause the vessel temperature profile (both laterally and axially) to be more uniform increasing the potential for more than one tube penetration to fail. The possibility of multiple, simultaneous tube penetration failures cannot be discounted. If a number of instrument tubes fail, the initial and possibly the final breach diameters and hence flow rates will be greater than the values assumed in the ZPSS. The longer time to failure will also allow further depressurization of the primary system.

A second consequence of a lower melt temperature is the effect on the debris relocation mechanism. Although the exact composition of the debris is not known, it is expected that the

mixture properties will behave similarly to other ternary compositions. Thus, the density, viscosity, and surface tension will be related to the melt temperature. Each of these terms is considered in the equations governing the relocation mechanism. A lower melt temperature will also reduce the heat flux of the jet stream after exit from the vessel. Thus, the potential and energetics of steam explosions, concrete decomposition, and steam generation will decrease with lower temperatures.

A lower debris temperature will also increase the potential for forming a stable crust above the molten material. A stable crust layer will disrupt the dispersal mechanisms that rely on removing material from the surface of the molten pool. The crust will also form an effective insulating layer that will reduce the heat transfer from the upper surface of the pool. This will cause the downward and sideward heat flux to increase and the concrete interaction to be more vigorous and longer. A longer concrete interaction period will increase the pressure load on containment by the release of water vapor and non-condensable (possibly flammable) gas species.

III.2 Gas Solubility in Melt

Several of the Zion accident sequences depict the development of a molten pool of core debris while pressure exists in the reactor vessel. The pressurizing gas is assumed to be principally water vapor and hydrogen from the oxidation of fuel cladding and structural materials. The ZPSS analysis does not consider the potential for gas in solution with the melt and the effect of the dissolved gases on the ex-vessel phenomena.

Gas solubility for metals and metal oxides is generally a function of both temperature and pressure. Reactor accidents must consider the potential for both hydrogen and oxygen dissociated from water to be soluble in the molten debris species. As an example, consider the solubility of hydrogen in iron that is known to obey Sievert's law:

$$1/2\ H_2\ (\text{gas}) \rightleftharpoons [H] \text{ dissolved in Fe}$$

where:

[H] = concentration of dissolved atomic hydrogen.

The equilibrium constant is:

$$K = \frac{[H]}{\left(P_{H_2}\right)^{1/2}}$$

or

$$\log K = \frac{-1637}{T} + 2.3126 = \log \frac{(\%H) \times 10^4}{\left(P_{H_2}\right)^{1/2}}$$

where:

T = the melt temperature (K)
P_{H_2} = the partial pressure of hydrogen (atms).

Then:

$$\log (10^4\ \%H) = \frac{-1637}{T} + 2.3126 + \frac{1}{2} \log P_{H_2}$$

The ratio P_{H_2} / P_{total} may range from 0.01 to 1.0 for an accident situation. Representative values for conditions of interest to the accident are given in Table 1.

TABLE 1
Dissolved Hydrogen in Molten Iron

Temp (K)	P_{H_2} (MPa)	$[H_2]$ cm^3 (STP)/100 g Fe	$[H_2]$ cm^3 (STP)/cm^3 Fe
1810	15.0	383	26.8
	7.5	271	19.0
	4.1	200	14.0
	0.1	31	2.2
2800	15.0	800	55.9
	7.5	565	39.5
	4.1	418	29.2
	0.1	65	4.5

It is apparent from the results in Table 1 that the solubility of hydrogen is a strong function of the melt temperature. The concentration is less affected by the variation in system pressure. The amount of dissolved gas represents a large volumetric fraction of the melt composition at ambient conditions. Upon release to the atmosphere during ejection, the gas will nucleate as bubbles and attempt to migrate towards the boundary of the jet.

The data given in Table 1 are prototypic considering the quantity of steel expected to be present in the molten core debris composition. Reactor accident studies must also consider gas solubility in the oxidic phase of the melt. Data are scarce on the subject of gas solubility in molten oxides, but Blander's correlation (Ref. 12) for gas solubility in molten salts can be used as a first approximation:

$$\ln \quad RT \frac{[C]}{P} = -9.104 \times 10^{16} \quad \frac{r^2 \sigma}{T}$$

where:

R = gas constant
T = absolute melt temperature
[C] = concentration of gas dissolved in the oxide
P = partial pressure
r = radius of the gas molecule
σ = melt surface tension.

Assuming the radius of an H_2O and H_2 molecules to be 2 A and 1.2 A, respectively and the surface tension of a prototypic oxidic melt to be 200 dynes/cm, estimated solubilities can be obtained. The results of the analysis (assuming no chemical interaction between the gas and oxide) are given in Table 2.

TABLE 2
Solubility of H_2 and H_2O in an Oxidic Melt

Temperature (K)	P_{H_2} (MPa)	P_{H_2O} (MPa)	Concentration H_2 (l STP/l of oxide)	Concentration H_2O (l STP/l of oxide)
2800	7.5	7.5	3.27	0.59
	1.5	13.5	0.65	1.06
	0.2	14.8	0.07	1.17
1800	7.5	7.5	3.11	0.22
	1.5	13.5	0.62	0.39
	0.2	14.8	0.06	0.43

The smaller size of the hydrogen molecule causes it to be more soluble than water vapor at equivalent conditions. The solubilities estimated by this correlation are lower than that for iron. The amounts appear; however, to be adequate to cause disruption of the melt if the gases come out of solution.

The implication of the above analysis is that molten core materials, under pressure, have a significant potential for the cover gas to go into solution with the melt. The dissolved gas will cause disruption of the melt stream as the gas bubbles nucleate and attempt to diffuse out of the melt and into the environment. The melt stream must then be modeled as a two-phase mixture of gas and liquid. The gas diffusion may also cause portions of the melt to be removed from the stream as the gas bubbles expand, burst and fragment. The fragments represent a source term for aerosol particles and fission products, discussed in more detail in Section III.4.

III.3 Vessel Failure

In the ZPSS analysis, the bottom head was assumed to be covered uniformly by the core debris. The 56 instrument-tube penetrations are concentrated in the central portion of the lower plenum, where the drainage and accumulation of debris is expected to occur. The ZPSS predicts that all tubes are attacked in a similar manner, with only a slight variation in the debris static head at the individual locations. Because the tube penetrations are identical, it is logical to assume that the thermal attack of the partial welds is nearly equivalent at all locations. This behavior seems to be supported by the ZPSS results given in Appendix 3.4.6 that indicate for at least 12 (possibly 16) of the cases studied, the mode of failure is when instrument "tubes" slip out of the vessel.

The consequence of two or more tubes failing simultaneously will be to alter the ZPSS assumption of a single jet emanating from the vessel. For multiple failures, one or more jets will develop, depending on the relative locations of the failures. The attack of the vessel wall, or breach growth, will then proceed at more than one location and the flow area available to the debris will be initially larger and will increase in size at a higher rate than assumed in the analysis. The flow area for vessel blowdown will be changed in a similar manner. The subsections below attempt to determine the effect of these changes on the debris dispersal.

III.3.1 Mass Flow Rate

The mass discharged out of the vessel, $\dot{m}$, for a jet stream can be estimated by:

$$\dot{m} = \rho_F A_c U$$

where:

ρ_F = density of melt

$A_c = \pi r^2 = \pi(r_o + Bt)^2$ = the area of the breach

$B = dr/dt$ = constant = the breach growth rate

r_o = initial breach radius

$$U = \left[\frac{2(P_o - P_a)}{\rho_F}\right]^{1/2} \quad = \text{jet discharge velocity}$$

P_o, P_a = pressure of vessel and containment, respectively.

The expression for A_c is developed from the form given in the ZPSS analyses while U is determined from Bernoulli's equation for incompressable steady flow.

The total mass discharged at any point in time is then found by integrating $\dot{m}$ from time Ø to time t_i

$$m_i = \int_{\emptyset}^{t_i} \rho_F \pi(r_o + Bt)^2 U(t)\, dt$$

where U(t) may be a function of time if flow through the breach is not choked.

For multiple failures, the area term in the above equation must be modified according to:

$$A_c' = \sum_{i=1}^{n} A_i = n\pi(r_o + Bt)^2$$

where n = number of tubes failed.

To determine the total mass discharged at any point in time, the integral equation becomes:

$$m_i' = \int_{\emptyset}^{t_i} \rho_F n \pi(r_o + Bt)^2 U(t)\, dt$$

The effect of additional tube failures is to cause an integer-multiple increase in the area available for material discharge as compared to the single-failure case. Assuming that the density and velocity of the stream are constant, the mass discharge is then given by:

$$m_t = \rho_F n\pi \left(r_o^2 t' + r_o B t'^2 + \frac{B^2 t'^3}{3}\right) U$$

where t' is the time from start of discharge (t=Ø).

This behavior is illustrated in Figure 6 for a small-break LOCA accident, comparing mass discharge versus time for n = 1, 2, 4 and 10. The plot indicates that increasing the number of failed tubes greatly shortens the discharge time. The most significant change occurs when n goes from 1 to 2 with the effect becoming less pronounced as n increases, approaching an asymptotic value as represented by n=10.

III.3.2 Interaction of Multiple Breach Locations

The behavior modeled in Figure 6 assumes that the various tube failures do not interact. If two or more adjacent tubes fail, the breach patterns may grow to intersect. The average tube spacing is approximately 40 cm, so that failures in adjacent tube locations will overlap in less than 0.5 second for the transient case (dr/dt = 41 cm/sec) and slightly over 1 second for a small-break LOCA (dr/dt = 26 cm/sec). Assuming this behavior occurs, adjacent tube failures will evolve into an asymmetric single breach with a somewhat smaller effective flow area than two independent failures.

If the diameter of the jets emanating from multiple locations is equivalent to the size of the breach (as the ZPSS assumes), the jets will not interact until the breach locations grow to intersect. Upon impact with the cavity floor, the behavior of the jets becomes more complex. Motions in the melt pool induced by the stagnation of multiple jets may destructively or constructively interact, so that the dynamic configuration of the debris may be affected.

III.3.3 Vessel Blowdown and Material Removal

The average pressure exerted by the jet on the concrete floor provides the driving force that induces the radial movement of the debris and subsequent splashout. This pressure is inversely related to the area of the jet. Multiple failures will involve more surface area and hence a reduced mean pressure and less radial force on the debris pool. The decreased radial movement causes the wave height growth to be lessened and the traveling velocity of the wave to decrease. These changes would also serve to mitigate the material removal by causing the traveling velocity of the wave to decrease relative to the material velocity.

Multiple tube failures will also alter the blowdown of the vessel following melt ejection because the flow area for the discharge is increased. The increased flow out of the vessel will cause the gas velocity in the tunnel area to increase directly affecting the film sweepout, particle levitation, and film entrainment mechanisms. Each mechanism is proportional to the dynamic pressure of the gas, i.e., $\rho_g U_g^2$ where U_g

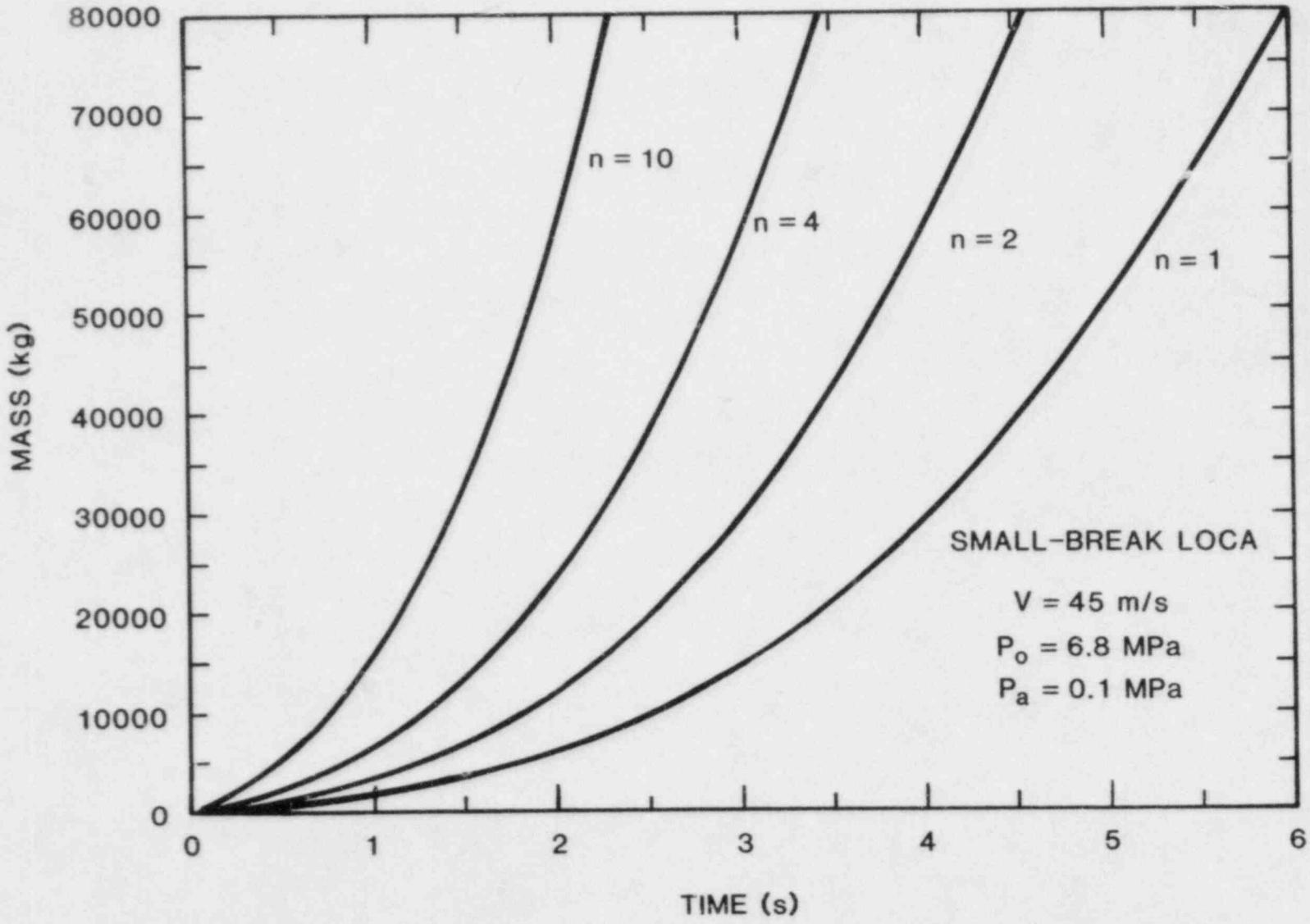

Figure 6. Mass Discharged for Multiple Tube Failures

and ρ_g are the velocity and density of the gas in the tunnel, respectively. Thus, an increased flow of gas out of the vessel will cause enhancement of three of the material removal mechanisms, but the duration of the blowdown will be correspondingly reduced.

The ZPSS considers breakup and entrainment of the molten material to be the principal removal mechanism. Following the initial dynamic processes, the velocity required for entrainment is given by:

$$U_e = \frac{3.7\left[g\,\mu(\rho_F - \rho_g)\right]^{1/4}}{(\rho g)^{1/2}}$$

where μ is the surface tension of the molten material and g is the acceleration due to gravity. If the gas velocity in the tunnel, U_g, exceeds U_e then material will be entrained in the gas stream.

In order for the particle to escape intact, its horizontal velocity must be converted to a nearly vertical velocity in the sloping instrument tunnel. For this to occur, the gas stream velocity must not change during the transition from the tunnel to the exit into containment. The criteria for escape is given by

$$L_3 < \frac{L_2^2}{4L_1}$$

where L_1 and L_2 are horizontal dimensions of the tunnel and L_3 is the vertical distance to the containment floor.

The material entrainment mechanism is only dependent on the gas velocity in the tunnel exceeding the entrainment velocity. Multiple tube failures will cause higher gas velocities in the tunnel than a single tube failure at corresponding pressure conditions, thus enhancing the material entrainment removal mechanism.

In summary, the net effect of multiple tube failures on the debris relocation appears to increase the likelihood of exceeding the criteria for material removal. This effect is balanced by a corresponding decrease in the duration of the blowdown of the RPV. Both effects must be considered when attempting to determine the extent of material removed. The ZPSS analysis showed only that the criteria for each mechanism were met, but did not carry out the calculations necessary to show that the combined influence is sufficient to cause all the material in the cavity to be removed.

III.4 Aerosol Production During Melt Discharge

The ZPSS considers aerosol production during in-vessel processes, steam explosions and core/concrete interactions in the cavity region. Aerosol formed during the melt discharge is not mentioned during the analyses. The high-pressure melt ejection experiments (SPIT tests) described in Appendix A have shown significant aerosol generation during the melt ejection sequence. The formation mechanisms active in the melt jet have tentatively been identified as condensation of vaporized melt species, bubble nucleation and breakup, and atomization. These processes may also be active in accident sequences.

Melt jet aerosols are important because of their potential for releasing fission products into the containment atmosphere. Secondary effects include the potential heat load from rapid oxidation of metallic particles, the burden placed on engineered safety devices by aerosol deposition, and the added potential to act as ignition sources for flammable gas species within the containment atmosphere.

III.5 Energetic Concrete Decomposition

High-temperature melts in contact with concrete produce very energetic reactions (Refs. 6 and 7). Gases thermally released from the concrete rapidly expand and are forceably driven through the melt to produce turbulent mixing. The magnitude of the forces has been observed to cause levitation of large melts.

Violent decomposition will affect the heat transfer in the cavity and the dispersal of the debris. A simple stagnation heat transfer correlation, as employed in the ZPSS, does not account for the influence of gas generation nor does it include the mechanical energy (velocity) of the impinging stream. The combination of large heat transfer rates and the high velocity of the jet may prove to be very efficient in eroding the basemat material. Enhanced erosion will increase gas generation and potentially disrupt the hydrodynamics of melt dispersal.

Melt/concrete interactions in other areas of the cavity can also influence the accident phenomena. As the melt flows over the cavity floor, the emerging gas from the floors and walls may cause disruption of the established flow patterns increasing the pressure loading on the containment. The upper sidewalls above the melt and the roof of the tunnel and keyway will also decompose due to the radiant heat flux from the melt, contributing to the overall pressure loading. If the gases react with the melt, the inventory of flammable gas species will be significantly altered.

III.6 Dynamic Debris Configuration

The ZPSS debris relocation mechanisms for the transient and small-break LOCA analyses are very dependent upon achieving a specific configuration for subsequent removal of material by the discharge of steam and hydrogen. The energetics of the melt/concrete interactions may be capable of disrupting the formation of a quiescent pool. The two-phase nature of the pool (with emerging gases) may make it capable of dissipating the jet pressure forces without relocation of the debris. The dynamic pool configuration shown in the ZPSS document (Fig. 3.2.8-1) may never form because of Helmholtz instabilities. If multiple jets exist, the stagnation pressure will be reduced and destructive interference of the pool dynamics may occur.

III.7 Geometric Features

The purpose of the reactor cavity, tunnel, and keyway is to provide access for the instrumentation tubes to the bottom of the RPV. The array formed by the tubes occupies a portion of the cross-sectional area of the tunnel and keyway. The presence of the tube array and its influence on the behavior of the debris and gas stream are ignored in the ZPSS. Viscous drag of the fluid over the tube walls removes energy from the flow, eventually reducing the mean velocity of the material.

The ZPSS analyses imply that the sump pit located at the end of the tunnel near the junction with the keyway does not influence the dispersal mechanism because the size of the sump (Ø.6m by Ø.6m) is small compared to the width of the tunnel at that location. Only splashout should be affected because the other three mechanisms are predominant on the surface of the debris pool.

The annular gap between the RPV and concrete cavity could provide a short-circuit flow path for the blowdown gases. A biological shield and associated insulation are placed around the vessel, effectively minimizing the available flow area. If these materials were damaged or displaced during the accident, diversion of the flow could result. Flow into the containment from the gap would reduce the energy available for debris removal.

IV. Scaling Analyses

The main objective of the HIPS experiments is to verify the debris relocation mechanism, and therefore the scaling analysis is based on satisfying the debris removal criterion. The high-pressure ejection of molten material into a concrete cavity involves a number of physical processes occuring within the same time frame. These processes include, but are not limited to; the movement and dispersal of the core debris, aerosol generation from the jet and from the melt/concrete and melt/water interactions, gas generation due to the decomposition of concrete and steam evolution, and the water quenching process.

IV.1 Program Strategy

The SPIT and HIPS test programs involve 1:20 and 1:10 linear scaled experiments, respectively. The results from the tests provide experimental information concerning the debris dispersal arguments presented in the ZPSS and will allow validation of the scaling analyses. The data will also furnish insight into other phenomena of interest and how they scale to the reactor situation.

IV.2 Summary of Scaling Analyses

Sections IV.3 through IV.5 contain detailed scaling analyses of the phenomena expected to be important during a high-pressure melt ejection into a reactor cavity. The analyses are presented for the 1:10 linear scaled model, with additional information concerning the 1:20 scale where required. Table 3 summarizes the phenomena and results of the analyses. All of the information, except debris removal mechanisms, are given in terms of scaling ratios. The removal mechanisms are evaluated in terms the criteria established by the ZPSS. The evaluations are based on the parameter values for the experiments and accidents (given in Table 4).

TABLE 3
Summary of Scaling Analyses

Phenomena	Scaling (Test/Accident)	
	SPIT	HIPS
Length	1/20	1/10
Area	1/400	1/100
Volume	1/8000	1/1000
Mass	1/8000	1/1000

TABLE 3 (Cont.)
Summary of Scaling Analyses

Phenomena	Scaling (Test/Accident) SPIT	HIPS
Time:		
Melt Ejection	1/1975	1/150 to 1/1400
Blowdown	1/20	1/10
Erosion Rate	1/(0.2 to 0.7)	1/(0.3 to 0.7)
Total Erosion:		
By Jet	1/(6 to 14)	1/(3 to 7)
By Pool	1/400	1/100
Thermal Mass	1/3200	1/398
Gas Generation:		
Jet Contact	1/1788	1/316
Pool Contact	1/8000	1/1000
Aerosol Particle Size Escaping Cavity	1/4.5	1/3.2
Debris Removal Mechanism		
Film Sweepout:	Exceeds Criteria	Exceeds Criteria
Film Entrainment:	Exceeds Criteria	Exceeds Criteria if Po $\geq$1.8 MPa
Particle Levitation:	Exceeds Criteria	Exceeds Criteria
Splashout:	Exceeds Criteria if wave thickness less than 27 cm	Exceeds Criteria if wave thickness less than 54 cm

The results show that the dimensions, mass and time are correctly scaled. The thermodynamic processes are less accurate with the test underpredicting all but one of the accident phenomena. Erosion rate is slightly over-influenced in the experiments, but when combined with the time scaling, the scaled total erosion is less in the experiment.

The aerosol particle size scaling is significant because the material escaping the cavity will have a smaller size range in the experiment than in the accident. This leads to the conclusion that the size distribution measured in the experiment will most probably be a lower bound on that expected for the accident.

Scaling of the debris dispersal mechanism insures that the ZPSS cutoff criteria are exceeded in the experiments. The ZPSS

TABLE 4

Parameter Values From the ZPSS and Experiment

Parameter (Symbol)	ZPSS Value	Experiment (Note a)
Density of Melt (ρ_F)	7000 kg/m^3	5900 kg/m^3
Pressure in Tunnel (P)	0.3 MPa	0.1 MPa
Melt Surface Tension (σ)	0.5 N-m	0.6N-m
Ratio of Specific Heats (k)	1.28-steam and H_2	1.30 - CO_2 1.40 - N_2
Acceleration of Gravity (g)	9.8 m/sec^2	9.8 m/sec^2
Height from Cavity to Containment Floor (h)	8, (maximum value)	0.4 m (0.2m)
Initial Area of Breach (A_r)	1.9 x 10^{-3} to 1.25m^2*	5.1 x 10^{-4}m^2**
Impact Area of Jet (A_j)	2 Times jet diameter	1.7 times jet diameter
Cross-sectional area of the Tunnel (A)	7.2 - 10.0m^2 (varies with length)	0.06 - 0.09m^2 (0.015 - 0.023)
Thickness of Wave ($\lambda/2$)	0.3m	?
Width of Tunnel (w)	3.2 - 2.3m (tapered)	0.3 - 0.2m (0.15 - 0.1)
Height of Tunnel	3.1m	0.3m (0.15m)
Density of gas (ρ_g)	600 kg/m^3	†1790 kg/m^3 (CO_2) 1250 kg/m^3 (N_2)
Temperature of Gas (T_o) (T)	625 K (In-vessel) 573 K (In tunnel)	? ?
Pressure in Vessel (P_o)	1.4 - 17.0 MPa	1.4 - 17.0 MPa
Particle Fragmentation Constant (C)	12	12
Aerodynamic Drag Coefficient (C_d)	0.5	?

* Dependent on breach size, assuming breach grows with time

** Can be varied to fit scaling criteria

† STP.

Notes:

a. - Values are given for 1/10th scale, 1/20th scale values when different are given in ( )

considers that exceeding the criteria is sufficient to insure debris removal from the cavity.

IV.3 Scaling of Debris Dispersal Mechanisms

The four debris relocation mechanisms identified in the ZPSS are described briefly in Section II.8. The analyses given in the ZPSS establishes cutoff criteria for each mechanism to determine if the conditions for existance are met in the accident situations. The calculations are made based on specifics of the plant and postulated accident conditions.

The cutoff criterion for each mechanism is expressed in terms of dimensionless parameters in Table 5. Film sweepout, film entrainment, and particle levitation are all based on one dimensionless grouping while the remaining mechanism, sweepout, is based on a second parameter. The definition of the dimensionless terms show that they are comprised of parameters related to the geometry of the cavity, the conditions in the RPV at the time breach occurs, and the thermophysical properties of the molten debris and gas. Subsequent sections discuss the scaling of each of the removal mechanisms.

IV.3.1 Time Scaling

Evaluating the cutoff criteria for each mechanism does not by itself establish the amount of material removed. It is assumed that the extent of material removed from the cavity is directly related to length of the time the cutoff criteria are exceeded. This suggests that the experiment not only must exceed the criterion but that the length of time the value is exceeded must also be scaled to that of the accident. The experiment to accident time scale can be determined by considering the discharge of the melt and the blowdown of gas. For the melt ejection period, the total mass discharged is given by:

$$m_f = \int_0^{t_e} \rho_f V_f A_r dt \qquad \text{(IV-1)}$$

where:

ρ_f = density of the melt
V_f = velocity of the melt through the breach
A_r = area of the breach
t_e = time required for melt ejection

Assuming that the pressure in the vessel is unchanged during the discharge period, the density and velocity are considered constant. Using the relationship developed for the breach growth rate, then equation (IV-1) becomes:

TABLE 5

Cutoff Criteria for Debris Removal Mechanisms

Removal Mechanism	Dimensionless Group	Cutoff Criterion
Film Sweepout	R_1	$R_1 \geq 9$
Film Entrainment	R_1	$R_1 \geq 13.7$
Particle Levitation	R_1	$R_1 \geq \left[\frac{4}{3}\frac{C}{C_D}\right]^{1/2}$
Splashout	R_2	$R_2 \geq 1$

$$R_1 = \frac{\rho_g V_g}{\left[g\sigma\rho_L\right]^{1/2}} = \frac{P_o}{\left[g\sigma\rho_L\right]^{1/2}}\left[\frac{A_r}{A}\right]^2 \cdot R_3$$

$$R_2 = \frac{V_L}{2gh} = \frac{P_o}{\left[gh\rho_L\right]}\left[\frac{A_r}{A_j}\right]\cdot\frac{2}{\lambda w}\cdot R_3$$

$$R_3 = \frac{P_o}{P}\frac{T}{T_o}\,k\left[\frac{2}{k+1}\right]^{\frac{k+1}{k-1}}$$

Definition of Terms

ρ - density
V - velocity
g - acceleration of gravity
A - area
P - pressure
T - temperature
w - width of tunnel
K - ratio of specific heats
h - height from tunnel to containment
σ - liquid surface tension
λ - wave thickness
C_d - aerodynamic drag coefficient
C - constant
R - gas constant

Subscripts:
g - gas stream
L - liquid
r - breach
o - in-vessel
j - jet impact area

$$m_f = \rho_f (Vol)_f = \rho_f V_f \int_o^{t_e} \pi (r_o + Bt)^2 dt \qquad \text{(IV-2)}$$

where:

Vol_f = volume occupied by the mass
r_o = initial breach radius
B = breach growth rate

Performing the integration yields:

$$Vol_f = V_f \, \pi \left(r_o^2 t_e + r_o B t_e + \frac{B^2 t_e^3}{3} \right) \qquad \text{(IV-3)}$$

The scaling criterion can then be established by taking the ratio of equation (IV-3) for the experiment and accident.

$$\frac{L^3)_E}{L^3)_A} \alpha \frac{Vol_f)_E}{Vol_f)_A} \qquad \frac{V_f \, \pi \left(r_o^2 t_e + r_o B t_e^2 + \frac{B^2 t_e^3}{3} \right)_E}{V_f \, \pi \left(r_o^2 t_e + r_o B t_e^2 + \frac{B^2 t_e^3}{3} \right)_A} \qquad \text{(IV-4)}$$

Equation (IV-4) suggests that the time scaling for the experiments is dependent on the length scale, initial breach radii and growth rate. The equation can be solved for the various accident and experiment conditions. The results of the analyses show that the scaling is principally dependent on the length scale and the size of the breach opening. These results are summarized as follows:

1:20 scale $t_E/t_A = 1/1975$ for $r_o = 1.25$ cm

1:10 scale $t_E/t_A = 1/245$ for $r_o = 1.25$ cm

$t_E/t_A = 1/981$ for $r_o = 2.5$ cm

The resulting scaling ratios are strongly influenced by both the length dimension ratios and the initial size of the breach. The two values of the breach growth rate (4.1 and 2.6 cm/sec) have an insignificant influence on the calculated ratios.

The time scaling analysis indicates that the desired time scale ratio at a given size scale may be achieved by adjusting the experimental initial breach radius. The HIPS experimental apparatus allows a range in the radius of approximately 1 to 3 cm. This range results in time scale ratios of 1/150 to 1/1400, respectively. This variation may be employed to adjust the scaling values of phenomena in the experiment.

A second time scale can be found by considering the blowdown of the pressure vessel to be given by the expression for the mass flowrate through the breach:

$$\dot{m}_r = \rho_g V_r A_r \qquad \text{(IV-5)}$$

where:

$\dot{m}_r$ = mass flowrate through the breach
ρ_g = density of gas
V_r = velocity of gas
A_r = breach cross-sectional area

The time required for blowdown can be found from the total mass in the system:

$$m_{total} = \int_{t_e}^{t_t} \dot{m}_r dt$$

where:

t_t = time when dispersal criteria are no longer exceeded

Assuming isentropic process, the density and velocity are constant for nearly the entire blowdown interval.

$$m_{total} = \dot{m}_r\, t \Big|_{t_e}^{t_t} = \rho_g V_r A_r (t_t - t_e) = \rho_g V_r A_r (t_{blowdown}) \qquad \text{(IV-6)}$$

Scaling is based on assuming that the linear dimensions of the experiment (E) are a known fraction of the accident (A) :

$$\frac{m_{total}\big)_A}{m_{total}\big)_E} = \frac{\rho_g V_r A_r t_{blowdown}\big)_A}{\rho_g V_r A_r t_{blowdown}\big)_E} \qquad \text{(IV-7)}$$

The gas density in the experiment and accident are nearly equivalent. Assuming that the pressure in the system is the same, then the velocity (from choked flow) through the breach is the same for both situations. Cancelling the common terms and rearranging to solve for $t_{blowdown}$, equation (IV-7) becomes:

$$\frac{t_{blowdown}\big)_E}{t_{blowdown}\big)_A} = \frac{A_r\big)_A}{A_r\big)_E} \cdot \frac{m_{total}\big)_E}{m_{total}\big)_A} \quad \frac{L^2\big)_A}{L^2\big)_E} \cdot \frac{L^3\big)_E}{L^3\big)_A} = \frac{L\big)_E}{L\big)_A}$$

The gas blowdown time is therefore scaled in the same manner as the length ratio, either 1:20 or 1:10 to that of the reactor accident.

IV.3.2 Film Sweepout

Film sweepout is identified as a liquid film that is dragged up and out of the cavity by the high-velocity gas stream caused by the reactor vessel blowdown. This mechanism occurs when the drag force on the wavy film surface is sufficient to lift the film against gravity. The necessary condition for initiation of film sweepout is obtained from the ZPSS as follows:

$$\frac{\rho_g V_g^2}{\left[g\sigma\rho_L\right]^{1/2}} \geq 9 \qquad \text{(IV-8)}$$

where:

ρ_g = gas density in the tunnel
V_g = gas velocity in the tunnel
g = acceleration due to gravity
σ = liquid surface tension
ρ_L = density of the molten core material

Equation (IV-8) can be written to solve for V_g:

$$Vg \geq \left[\frac{9\left[g\sigma\rho_L\right]^{1/2}}{\rho_g}\right]^{1/2} \qquad \text{(IV-9)}$$

Equation (IV-9) should be evaluated at the pressure, temperature, and gas species conditions existing in the tunnel during the experiment. By way of example, it is assumed that nitrogen at 100 psig and 570K is a typical lower bound of the possible range. Using Table 4 for the appropriate material properties gives:

$$Vg \geq 1.2 \text{ m/sec}$$

This value represents the gas velocity in the tunnel necessary to insure film sweepout and can be used to determine a corresponding system pressure. Using conservation of mass and the dimensions of the system:

$$\dot{m}_{tunnel} = \dot{m}_{breach}$$

$$\dot{m}_{tunnel} = \rho_g A_r V_g)_{tunnel}$$

$$\dot{m}_{breach} = P_o A_r \left[\frac{k}{RT} \left(\frac{2}{k+1} \right)^{\frac{k+1}{k-1}} \right]^{1/2} \qquad \text{(IV-10)}$$

where:

P_o = pressure in the vessel
k = ratio of specific heats
R = universal gas constant

Solving for the vessel pressure gives:

$$P_o = \frac{\rho_g A_r V_g)_{tunnel}}{A_r \left[\frac{k}{RT} \left(\frac{2}{k+1} \right)^{\frac{k+1}{k-1}} \right]^{1/2}} \qquad \text{(IV-11)}$$

Using the resultant above for V_g from above and values from Table 4 yields:

1:10 Scale $P \geq$ 0.028 MPa = 4 psi
1:20 Scale $P \geq$ 0.007 MPa = 1 psi

Thus, all pressures included in the test range (1.4 - 17.0 MPa) will cause the gas velocity to exceed the film sweepout criterion.

IV.3.3 Film Entrainment

Waves will form on the liquid pool in the cavity if the gas velocity is sufficiently large. Liquid entrainment into the gas results from wave crest erosion by the high-velocity gas stream. According to the ZPSS, film entrainment occurs when the following criterion is satisfied.

$$\frac{\rho_g V_g^2}{\left[g \sigma \rho_L \right]^{1/2}} \geq 13.7 \qquad \text{(IV-12)}$$

where:

σ = surface tension of the melt

This differs from the film sweepout criterion only by the constant of proportionality, so that equation (IV-9) becomes:

$$V_g \geq \left[\frac{13.7 \left[g \sigma \rho_L \right]^{1/2}}{\rho_g} \right]^{1/2} \qquad \text{(IV-13)}$$

Solving equation (IV-13) for an initial nitrogen pressure of 1.4 MPa (200 psig) gives:

$$Vg \geq 1.4 \text{ m/sec}$$

This criteria is easily satisfied for the range of system conditions under consideration ($P \geq 1.4$ MPa).

IV.3.4 Particle Levitation

Entrained particles can be swept out of the instrument tunnel if hydrodynamic drag forces are sufficient to lift the particle against gravity. This occurs when the following criterion is satisfied:

$$\frac{3}{4} C_d \left(\frac{\rho_g V_g^2}{g D \rho_L} \right) \geq 1 \qquad \text{(IV-14)}$$

where:

C_d = aerodynamic drag coefficient

D = entrained particle size

The entrained particle size is dependent on the dynamic pressure, $\rho_g V_g^2$. A reasonable approach is to assume the following:

$$D = \frac{C \sigma}{\rho_g V_g^2} \qquad \text{(IV-15)}$$

The constant C is unspecified for particles initially entrained into the gas stream, but once particles are entrained, they are subject to hydrodynamic fragmentation. The maximum

stable fragment sizes can be estimated with Equation IV-15 when the constant C is about 12 (Ref. 13).

Substituting Equation IV-15 into the particle levitation criterion yields the same variable grouping shown in the film sweepout and film entrainment criteria.

$$\frac{\left[\rho_g V_g^2\right]^2}{g\rho_L D} \geq \frac{4}{3}\left(\frac{C}{C_d}\right) \qquad \text{(IV-16)}$$

Therefore, the gas velocity can be found from:

$$V_g \geq \left(\frac{4}{3}\,\frac{C}{C_d}\right)^{1/4} \left[\frac{\left(g\sigma\rho_L\right)^{1/2}}{\rho_g}\right]^{1/2} \qquad \text{(IV-17)}$$

Evaluating the expression containing C can be done using values from the ZPSS.

$$\left(\frac{4}{3}\,\frac{C}{C_d}\right)^{1/4} = \left(\frac{4}{3}\,\frac{12}{\emptyset.5}\right)^{1/4} = 2.34$$

Comparing this result to the constant in equation (IV-9) and (IV-13) shows that the particle levitation criterion will also be exceeded for experimental conditions.

IV.3.5 Splashout

The ZPSS proposes that the dynamic configuration of the debris will cause a high-amplitude, small-wavelength wave to be accelerated down the instrument tunnel. Film mass is converted to wave mass which has an ever-increasing material velocity. Splashout will occur when the wave impacts the far tunnel wall if the wave mass has sufficient kinetic energy to overcome the gravity potential associated with lifting material up and out of the instrument tunnel. The necessary condition for sweepout is:

$$\frac{V_L^2}{2gh} \geq 1 \qquad \text{(IV-18)}$$

where:

V_L = the material velocity when the wave impacts the slanted keyway at the end of the tunnel

h = height which material must be lifted to remove it from the instrument tunnel.

In order to determine if the necessary criterion for mass removal is met in the tests, the dynamic gas pressure in the tunnel and material velocity for splashout must be related to known quantities.

The gas velocity in the tunnel can be written in terms of the mass flow rate ($\dot{m}$) in the tunnel.

$$\rho_g V_g^2 = \rho_g \left[\frac{\dot{m}}{\rho_g A} \right]^2 \qquad \text{(IV-19)}$$

Where, A is the cross-sectional area for gas flow in the tunnel.

The mass flow rate in the tunnel is equal to the choked-flow condition exiting the reactor vessel.

$$\dot{m} = P_o A_r \left[\frac{k}{RT_o} \left(\frac{2}{k+1} \right)^{\frac{k+1}{k-1}} \right]^{1/2} \qquad \text{(IV-20)}$$

The gas density in the instrument tunnel is given by the ideal gas law:

$$\rho_g = \frac{P}{RT} \qquad \text{(IV-21)}$$

where the terms (P,T) are obtained at a specified location in the tunnel.

Combining Equations IV-19 through IV-21 yields an expression for the dynamic pressure in terms of known quantities in the reactor vessel and instrument tunnel.

$$\rho_g V_g^2 = P_o \left[\frac{A_r}{A} \right]^2 \left[\frac{P_o}{P} \frac{T}{T_o} k \left(\frac{2}{k+1} \right)^{\frac{k+1}{k-1}} \right] \qquad \text{(IV-22)}$$

The material velocity of the high-amplitude, small-wavelength wave considered in the splashout model can also be related to known quantities. This is accomplished by applying Newton's Law to the wave. The resulting differential equation describing the wave position in the tunnel is given in the ZPSS as:

$$\frac{d^2x}{dt^2} = \frac{2\Delta P}{\lambda \rho_L} \qquad \text{(IV-23)}$$

where the ΔP term is the driving pressure $(P_o - P)$

The ZPSS expression for the position-dependent driving pressure is simplified by using a constant pressure equal in value to the actual driving pressure half-way down the tunnel.

$$\Delta P = \frac{\dot{m}^2}{\rho_g A_a A_j} = \frac{2\dot{m}^2}{\rho_g A_j L W} \qquad \text{(IV-24)}$$

where:

A_j = impact area on the instrument tunnel floor of the gas jet emanating from the reactor vessel

L = distance traveled by the wave at the point where it impacts the far tunnel wall

W = width of the tunnel

The mass flow rate in the tunnel is given by Equation IV-20 and the gas density in the tunnel is given by Equation IV-21.

The material velocity for the wave impacting the far wall of the instrument tunnel is obtained by integrating Equation IV-23.

$$V_L^2 = \frac{P_o^2}{\rho_L P} \left[\frac{A_r^2}{A_j}\right] \frac{4}{\lambda W} \frac{T}{T_o} k \left[\frac{2}{k+1}\right]^{\frac{k+1}{k-1}} \qquad \text{(IV-25)}$$

Combining equations (IV-18) and (IV-25) gives an expression for scaling based on known variables:

$$\frac{P_o^2}{gh\rho_L P} \left[\frac{A_r^2}{A_j}\right] \frac{2}{\lambda W} \frac{T}{T_o} k \left[\frac{2}{k+1}\right]^{\frac{k+1}{k-1}} \geq 1 \qquad \text{(IV-26)}$$

All of the terms in the above expression can be easily established, except for the wave thickness (λ). Rearranging equation (IV-26) and solving for λ using typical values for the other parameters yields:

For Po = 1.4 MPa N_2: $\lambda \leq 1.0$ m

For Po = 17.0 MPa N_2: $\lambda \leq 127$ m

For the lowest pressure value, the required wavelength thickness would be greater than the largest dimension of the scaled cavity in order to not satisfy the splashout criterion. Therefore, the pressure range of the experiments will cause the splashout criterion to be exceeded.

IV.4 Scaling Thermodynamic Phenomena

The previous Section considered only the hydrodynamic aspects of the debris removal mechanisms involved in the accident and experimental sequences. Scaling of the thermodynamic criteria are evaluated in this section.

IV.4.1 Concrete Erosion

Concrete erosion is thermal decomposition caused by contact with material at elevated temperature. Two types of interactions are defined for the high pressure discharge of material into a scaled reactor cavity:

(a) Pressurized ejection of the melt onto the concrete below the reactor vessel.

(b) Flow of melt over the concrete in the tunnel and keyway.

The rate and extent of erosion in the HIPS tests are important aspects of the ex-vessel debris behavior. Concrete erosion may influence the development and magnitude of the key hydrodynamic processes being studied in the tests.

Melt streaming onto a concrete surface will impose a heat flux that may be estimated by a stagnation heat flux correlation (Ref. 14) for a fluid impacting an ablating solid surface.

$$\dot{Q} = 0.55\left(\frac{C_p\nu}{K}\right)^{0.35} K(T_s - T_c)\left(\frac{2V\rho_L}{d_m\nu}\right)^{1/2} \qquad \text{(IV-27)}$$

where:

C_p = heat capacity

ν = viscosity

K = thermal conductivity

T_s = temperature of the melt stream

T_c = melting point of concrete

V = stream velocity

d_m = stream diameter

All the terms in the above equation are roughly equivalent in both the accident and experiment cases, except for the stream diameter. The appearance of terms involving the stream geometry distort the rate of concrete erosion from that expected in the accident. To a first approximation, the rate of concrete erosion ($\dot{\varepsilon}$) will be proportional to the imposed heat flux as given by Equation (IV-27).

$$\frac{\dot{\varepsilon}_E}{\dot{\varepsilon}_A} \alpha \frac{\dot{Q}_E}{\dot{Q}_A} \alpha \left(\frac{d_A}{d_E}\right)^{1/2} \alpha \left(\frac{D_A}{D_E}\right)^{1/2} \qquad \text{(IV-28)}$$

where D is the breach diameter and the subscripts E and A refer to the experiment and accident, respectively. Equation IV-28 suggests that concrete erosion is inversely proportional to the square root of the breach diameter. For the dimensions given in Table 4:

$$\frac{\dot{\varepsilon}_E}{\dot{\varepsilon}_A} = \left(\frac{2.5}{1.2}\right)^{1/2} = 1.4 \quad \text{or} \quad \left(\frac{2.5}{2.5}\right)^{1/2} = 1.0$$

These results are appropriate only for the initial rate, where the breach diameters are established by the geometry of the RPV and experimental apparatus. Ablation of the breach aperture may cause the scaling to change at later times. Erosion rate scaling taking into account the possible growth of the breach during ejection is of the form:

$$\frac{\dot{\varepsilon}_E}{\dot{\varepsilon}_A} \alpha \frac{\left(r_o + \frac{dr}{dt}(t)\right)_A^{1/2}}{\left(r_o + \frac{dr}{dt}(t)\right)_E^{1/2}} \qquad \text{(IV-29)}$$

where:

r_o = initial breach radius

dr/dt = breach growth rate

t = time

For t = o, the breach growth rate term is not operative and the equation reduces to equation (IV-28). For later times in the sequence, the breach growth becomes significant. Assuming the growth rates are nearly equilvalent for the test and accident, then the scaling is dependent on the initial breach radii and the duration of the event. Because the time scales for the ejection period are estimated to be in the range 1/150 to 1/1400, the second term in the denominator $(dr/dt)t_E$ is small relative to the accident. The erosion rate scaling then becomes a non-linear function of t.

Equation (IV-29) then becomes:

$$\frac{\dot{\varepsilon}_E}{\dot{\varepsilon}_A} \alpha \frac{\left(r_o + \frac{dr}{dt} t_A\right)_A^{1/2}}{\left(r_o\right)_E^{1/2}}$$

Thus, the ratio of test to accident erosion rates varies between 3.8 and 4.2 depending on the duration of the event. For the limiting case of the small-break LOCA $t_A \simeq 7$ seconds, so that the equation yields:

$$\frac{\dot{\varepsilon}_E}{\dot{\varepsilon}_A} \alpha \left(\frac{2.5 + 2.6(7)}{(1.2)^{1/2}} \right)^{1/2} = 3.8$$

where the parameter values are stated in cgs units.

The total extent of concrete erosion (ε) is the product of the erosion rate and the duration of melt streaming:

$$\frac{\varepsilon_E}{\varepsilon_A} = \frac{\dot{\varepsilon}_E}{\dot{\varepsilon}_A} \times \frac{t_E}{t_A} = (1.4 \text{ to } 5.1) \times (1/150 \text{ to } 1/1400) = (1/30 \text{ to } 1/1000)$$

Thus, the total concrete erosion by the jet in the tests will significantly underpredict the accident value.

The second area of consideration for scaling erosion is the effect induced by melt flowing along the tunnel floor and keyway. Previous melt/concrete interaction experiments (Refs. 6, 14) have shown that concrete erosion is dependent in a nearly linear manner on the depth or static head of the melt pool. The ratio of test to accident erosion in the tunnel location, is then given by:

$$\frac{\varepsilon_E}{\varepsilon_A} \alpha \frac{h_E}{h_A} \cdot \frac{t_E}{t_A} = \frac{M}{\rho_L A}\Big)_E \cdot \frac{\rho_L A}{M}\Big)_A \cdot \frac{t_E}{t_A} \qquad \text{(IV-30)}$$

where M is the amount of melt deposited on the tunnel floor (area A).

If the density of the melt in the accident and experiment is nearly the same, then:

$$\frac{\varepsilon_E}{\varepsilon_A} \alpha \frac{\frac{Mt}{A}\Big)_E}{\frac{Mt}{A}\Big)_A} \alpha \frac{\frac{L^3 t}{L^2}\Big)_E}{\frac{L^3 t}{L^2}\Big)_A} = \frac{Lt\Big)_E}{Lt\Big)_A} \qquad \text{(IV-31)}$$

For 1:10 linear scale:

$$\frac{\varepsilon_E}{\varepsilon_A} \alpha \frac{1}{10} \left(\frac{1}{150} \text{ to } \frac{1}{1400}\right) = \frac{1}{1500} \text{ to } \frac{1}{14000}$$

For 1:20 linear scale:

$$\frac{\varepsilon_E}{\varepsilon_A} \alpha \left(\frac{1}{300} \text{ to } \frac{1}{28000}\right)$$

The results of the above calculations indicate that the erosion caused by the melt pool in the experiment will greatly underpredict the accident behavior.

IV.4.2 Thermal Mass

The total thermal energy of the melt mass at the time of vessel failure can be found by using values given in the ZPSS. For an assumed temperature of 2200 ^{o}C and a mass of 8 x 10^4 kg, the thermal energy of the melt is approximately 1.02 x 10^5 MJ.

The thermal mass of thermite is estimated to be on the order of 3.2 to 3.6 MJ/kg, depending on the degree of completion of the reaction and the heat losses in the melt generator apparatus. Using the lower value gives a total energy content of 256 MJ (80 kg mass) or 32 MJ (10 kg mass). The higher specific energy of the thermite compared to the accident is due principally to its higher reaction temperature.

Because stored energy of a system is based upon the mass of the system, then proper scaling for the 1:10 scale test should be of the form:

$$\frac{E_E}{E_A} \alpha \frac{m_E}{m_A} = \frac{1}{1000} \quad \text{(1:10 scale)} \qquad \text{(IV-32)}$$

Using values from above, the estimated scaling ratio is:

$$\frac{E_E}{E_A} \alpha \frac{256}{1.02 \times 10^5} \cong \frac{1}{400}$$

This result suggests that the energy content of the test in both scales is roughly 2-1/2 times greater than desired. The test value can be altered by lowering the temperature of the melt or increasing heat losses prior to ejection.

Degraded core material will continue to heat after ejection due to the decay of fission products. The decay heating curve can be used to estimate the amount of additional energy that is contributed by fission product heating during the accident sequence. This value can then be used to compare to the experiment to evaluate the adequacy of thermite as a debris simulant.

The expression for the decay power level at any point in time is given by (Ref 15):

$$P(t) = P_o A t^{-a} \qquad \text{(IV-33)}$$

where:

$P(t)$ = power level

P_o = power at time of shutdown

A, a = constants used to fit the data

It is reasonable to use P_o = 2400 MW (80% of 3000 MW) by assuming that some of the fission products are lost during the melting process prior to ejection. For the time interval from 150 seconds to 4×10^6 seconds after shutdown, the constants for

the expression are: A = 0.130, a = 0.283. The power generated during an accident is then obtained by integrating the power history over the duration of the event.

$$E_{ejection} = \int_{t_1}^{t_2} (.130)\ (2400)t^{-0.283}\ dt \qquad \text{(IV-34)}$$

where:

t_1, t_2 = the start and end times for the discharge.

The integration yields:

$$E_{ejection} = 312 \left[\frac{t\ \exp(1 - 0.283)}{1-0.283}\right]\Bigg|_{t_1}^{t_2} \qquad \text{(IV-35)}$$

The values for t_1 and t_2 are determined by estimating the time after the start of the accident that the ejection occurs and the expected interval for thermal interactions. Most of the accident sequences in the ZPSS indicate vessel failure between 1 and 10 hours after shutdown. The melt ejection and gas blowdown processes have a combined duration on the order of 50 to 100 seconds, depending on the type of failure and initial system pressure.

Evaluating equation (IV-35) for the two bounding times and using a conservative 100-second duration:

$$E_{ejection\ 1\ hr} = 435\ (361.7 - 354.7) = 3.0 \times 10^3\ MJ$$

$$E_{ejection\ 10\ hr} = 435\ (1852.4 - 1848.7) = 1.6 \times 10^3\ MJ$$

These values represent the amount of decay heat generated during the ejection interval. Given the larger value at 1 hour after shutdown, the decay heating represents a 2.9% additional contribution to the total thermal mass (1.02×10^5 MJ).

The result above indicates that decay heat provides only a small additional contribution to the total energy content of the system, for the time interval representing the discharge of the vessel. For the small-break LOCA and transient sequences where the time duration is even shorter than above, the added energy due to decay heating will be less than 2%. Thus, the lack of additional heating when using a thermite melt simulant is not a significant source of error.

IV.4.3 Gas Generation

The thermal decomposition of concrete releases water and carbon dioxide from within the matrix of the material. These releases occur over distinct temperature ranges allowing the gas generation to be related to the propagation of isotherms into the material. The velocity of propagation can be estimated from the relationship (Ref 5):

$$V = \frac{\dot{Q}}{\rho F_j + \int_{T_1}^{T_2} \rho c_p dT} ; \qquad \text{(IV-36)}$$

where:

V = isotherm velocity
$\dot{Q}$ = heat flux incident on the surface
ρ = density of concrete
c_p = specific heat
F_j = enthalpy of decomposition of jth species
T_1, T_2 = temperature limits of the decomposition process

If the heat flux is suddenly imposed, as would be the case in the accident or the test, the above relationship suggests that the isotherm velocities are dependent only on the thermophysical properties of concrete. Table 6 lists the main three concrete constituents that contribute to gas generation and their associated decomposition enthalpy values (From Ref. 6).

TABLE 6

Thermal Processes in the Decomposition of Concrete*

Constituent	Weight Percent (%)	Decomposition	
		Enthalpy (J/gm)	Temperature Range (C)
Free Water	2.7	81.6	30-230
Bound Water	2.0	120	360-485
Carbon Dioxide	22.0	960	600-1000

* Generic Limestone-Common Sand

Comparison of the data in Table 6 indicates that the two water loss mechanisms occur over different temperature ranges of nominally equivalent span. Thus, enthalpies for these events are approximately the same. The velocities associated with these two mechanisms will be nearly equal for the same imposed heat flux. The isotherm associated with the decarboxylation process will proceed at a slower rate because of its relatively larger temperature range and enthalpy of reaction.

The above analysis implies that the quantity of gas generated from concrete is related to the applied heat flux and the duration of the event. Using equation (IV-27) gives:

$$\frac{m_{g_E}}{m_{g_A}} \alpha \frac{\dot{Q}_E}{Q_A} \times \frac{t_E}{t_A} \times \frac{A_E}{A_A} \alpha \left(\frac{d_A}{d_E}\right)^{1/2} \times \frac{t_E}{t_A} \times \frac{A_E}{A_A} \qquad \text{(IV-37)}$$

where:

m_g = mass of gas released

A = area covered by jet stream

In order to evaluate equation (IV-37), the stream diameter must be known. One approach is to assume that the stream diameter is equivalent to the breach diameter in the reactor vessel or melt generator. Thus, for the 1:10 scale model:

$$\frac{m_{g_E}}{m_{g_A}} \alpha \left(\frac{5}{2.5}\right)^{1/2} \times \left(\frac{1}{150} \text{ to } \frac{1}{1400}\right) \times \frac{1}{100} = \left(\frac{1}{10600} \text{ to } \frac{1}{99000}\right)$$

The gas released during the experiment will vastly underpredict that expected during an accident.

This result is also subject to the same reservations stated previously concerning the dependence of the incident flux and time scales on the breach diameter. Variations in breach radius and growth rates will cause the ratio to vary within the indicated range.

The gas generation from the floor and sides of the tunnel in contact with the pool can also be related to the heat flux from the melt. As the melt moves across the tunnel floor, the heat flux is assumed to be a combination of conduction and convection. After the initial movement ceases, the heat transfer will be principally conduction with gas-injection induced turbulence in the pool. In both cases, the heat flux is proportional to the temperature difference (ΔT) between the melt and the concrete. The scaling is then:

$$\frac{m_{g_E}}{m_{g_A}} \alpha \frac{\Delta T_E}{\Delta T_A} \times \frac{t_E}{t_A} \times \frac{A_E}{A_A} \qquad \text{(IV-38)}$$

In this case the time scaling is obtained from the mechanisms controlling melt dispersal (blowdown of the vessel). If the temperature of the pool in the accident and experiment are nominally equivalent for 1:10 scale, equation (IV-38) becomes:

$$\frac{m_{g_E}}{m_{g_A}} \alpha \frac{1}{10} \times \frac{1}{100} = \frac{1}{1000}$$

The result indicates that the amount of gas generated in the test due to contact by the melt pool will scale in the same ratio as that desired for the relative masses of the melt.

IV.5 Scaling Aerosols

The aerosol/fission product source term to containment building is defined by:

1. Mass of aerosol input to containment (penetration)
2. Size distribution of aerosol
3. Size-dependent composition of the fission products and bulk material of the aerosol

The melt ejection aerosol/fission product source term is in addition to and distinct from source terms arising from in-vessel fuel disruption and melting (the so-called in-vessel source term) and from ex-vessel melt-concrete interaction (the so-called ex-vessel source term). The aerosol source term is important because it presents a potential radiological hazard and may affect the containment response to the accident.

Experiments (Appendix A) have demonstrated the formation of aerosols upon high-pressure ejection of a thermitically-generated melt. In the accident case, aerosols ejected into the reactor cavity must traverse the tunnel and keyway before they are released to containment. Material that does not escape the keyway is of little significance to the containment aerosol source term because it settles out onto the cavity floor or impacts on the bend of the keyway and is returned to the melt. Figure 7 illustrates the relationship between the melt ejection aerosol distribution, the size-dependent keyway penetration function, and the resulting aerosol source term to containment.

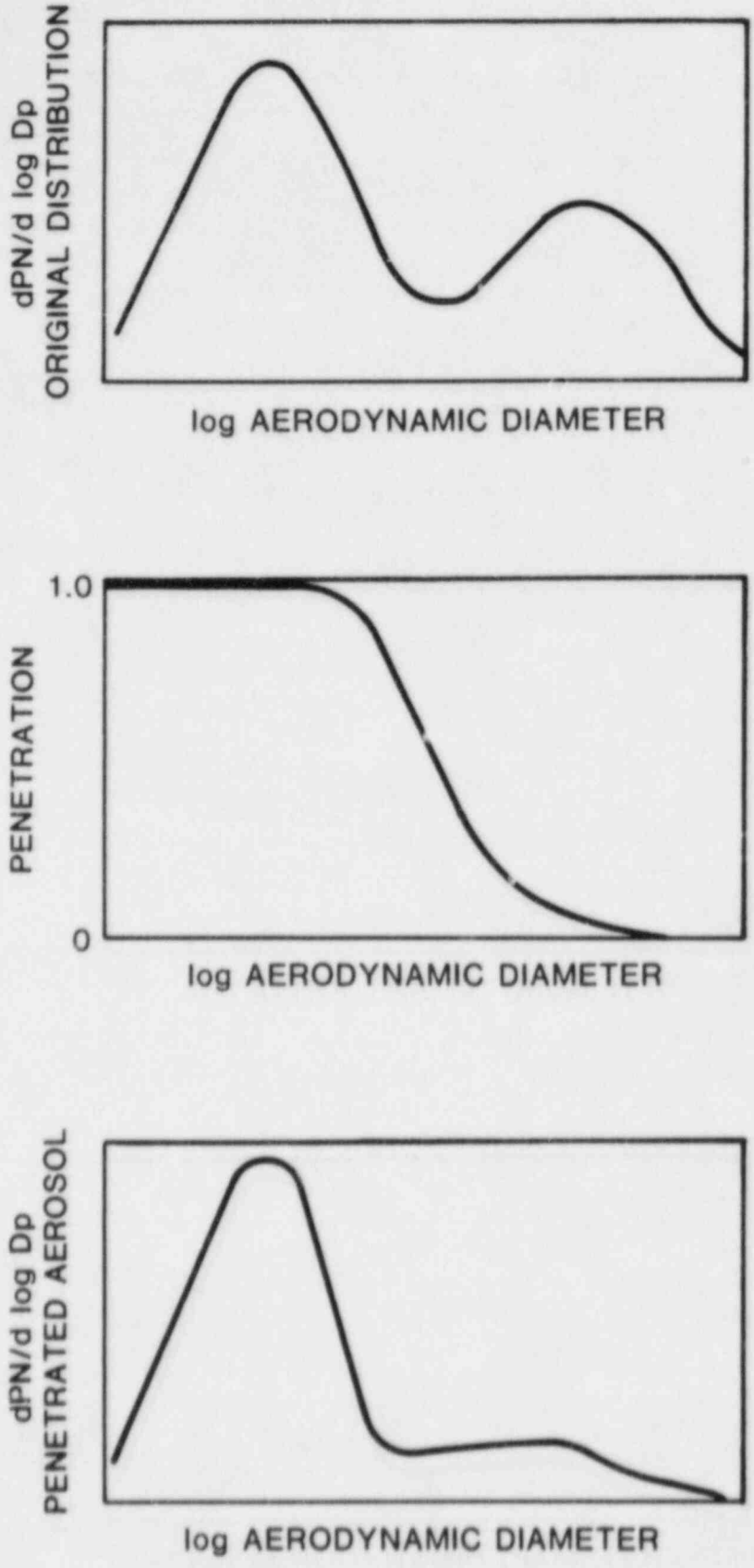

Figure 7. Penetration Aerosol Relationship to the Source Term

An aerosol source term to containment has two aspects of importance - radiological and physical - which are difficult to separate from one another. The melt ejection aerosol has a fission product component which presents a radiological hazard. These products are associated with bulk particles whose physical properties determine transport charcteristics and residence time in the containment atmosphere. It is therefore necessary to know the particle size distribution and associated fission product inventory to assess the radiological hazard for the accident scenario.

Physical properties of the aerosol may have a significant effect on containment response. At large concentrations, aerosols can plug filters and vents and interfere with the function of fan coolers, pumps, and heat transfer surfaces. In the melt ejection case, unoxidized metal in the aerosol particles may rapidly oxidize upon entering the containment atmosphere, providing an additional heat load. The particles could act as an ignition source for the hydrogen released during the blowdown process. In the event of an early containment failure, the aerosol would be the principal radiological hazard.

The existing data on melt ejection aerosol generation is inadequate to fully address the potential consequences of the above issues. The Phase I SPIT test data are of a qualitative nature that prove useful in suggesting phenomena which have not been considered in the ZPSS.

The scaled cavity tests have been formulated to study the melt relocation mechanisms of the ZPSS and are sized with these phenomena in mind. It is possible, however, to make some observations on the test scaling with respect to aerosol formation.

1. Aerosol generation due to bubble nucleation and diffusion will scale with path length through the melt (1:10).

2. Material aerosolized by pneumatic atomization is proportional to the material remaining in the pressure vessel and the surface area wetted by the melt. These functions are dependent upon the vessel geometry which is not scaled. Scaling for this mechanism is unclear but can be assumed to be between 1:100 and 1:1000.

3. Vaporized material from an undisrupted jet scales with surface area (L^2) and time of propagation. The kinetics of aerosol generation are dependent on the unscaled parameters of temperature and pressure. The time of propagation is dependent on jet velocity (unscaled) and the height of the vessel to the concrete or water pool surface. It is not certain that the aerosol generation scales linearly with jet height (1:10).

4. The velocity of the particles in the tunnel is dependent on slip and residence time. The smaller size of the experiments may reduce the extent of aerosol removed because of the shorter length scale.

These scaling observations lead to the conclusion that aerosol formation in these tests will not scale in a straightforward linear manner. If aerosol generation scales with melt volume, the concentrations will be at realistic levels because the cavity volume is scaled by the same factor. This does not consider the effect of the shorter jet height, which would act to decrease aerosol mass.

Another important issue to be addressed by scaling is the inertial impaction of particles at the end of the keyway. Aerosol size-dependent transport through the keyway in the scaled tests will not correspond directly to that expected for the accident case. Inertial impaction of particles at the transition from the tunnel to the keyway is assumed to be the principal removal mechanism during transport through the keyway. The Stokes Number (Stk) is the appropriate scaling parameter for impaction. Physically, it is the ratio of particle stopping distance to some characteristic length of the impaction geometry and is defined as:

$$Stk = \frac{\rho_p D_p^2 \; C(D_p) g}{18 \nu L} \qquad \text{(IV-39)}$$

where:

ρ_p = particle material density

D_p = particle diameter

$C(D_p)$ = Cunningham slip correction

g = acceleration due to gravity

ν = absolute viscosity of gas

L = characteristic linear dimension of impaction geometry

For similiar geometries of unequal size, it is reasonable to assume that the penetration (fraction of material into containment) as a function of Stokes number will be nominally the same. Therefore, the scaling relationship from equation (IV-39) becomes:

$$1 = \frac{Stk_E}{Stk_A} \alpha \frac{\left(D_p^2 \; L^{-1}\right)_E}{\left(D_p^2 \; L^{-1}\right)_A} \qquad \text{(IV-40)}$$

where the equivalent terms in the accident and experiment have been deleted. From equation (IV-40) the particle size dependency can be found:

$$\frac{D_{p_E}}{D_{p_A}} = \left(\frac{L_E}{L_A}\right)^{1/2} \qquad \text{(IV-41)}$$

For 1:10 scale:

$$\frac{D_{p_E}}{D_{p_A}} = \frac{1}{3.2}$$

For 1:20 scale:

$$\frac{D_{p_E}}{D_{p_A}} = \frac{1}{4.5}$$

Based on the Stokes number equivalency, the diameter of the particle entering the containment region is much larger in the experiments than in the accident. Thus, any material escaping the cavity in the scaled tests will almost certainly also escape in the reactor case. This behavior is illustrated in Figure 8, showing the loss of particles by impaction as a function of Stokes number.

If accurate data are obtained on the aerosol distributions generated from free jet experiments and scaled cavity experiments at equivalent conditions, penetration estimates for the test article can be made. These data will allow estimation of the Stokes Number dependence of penetration and estimation of the aerosol sizes leaving the reactor keyway.

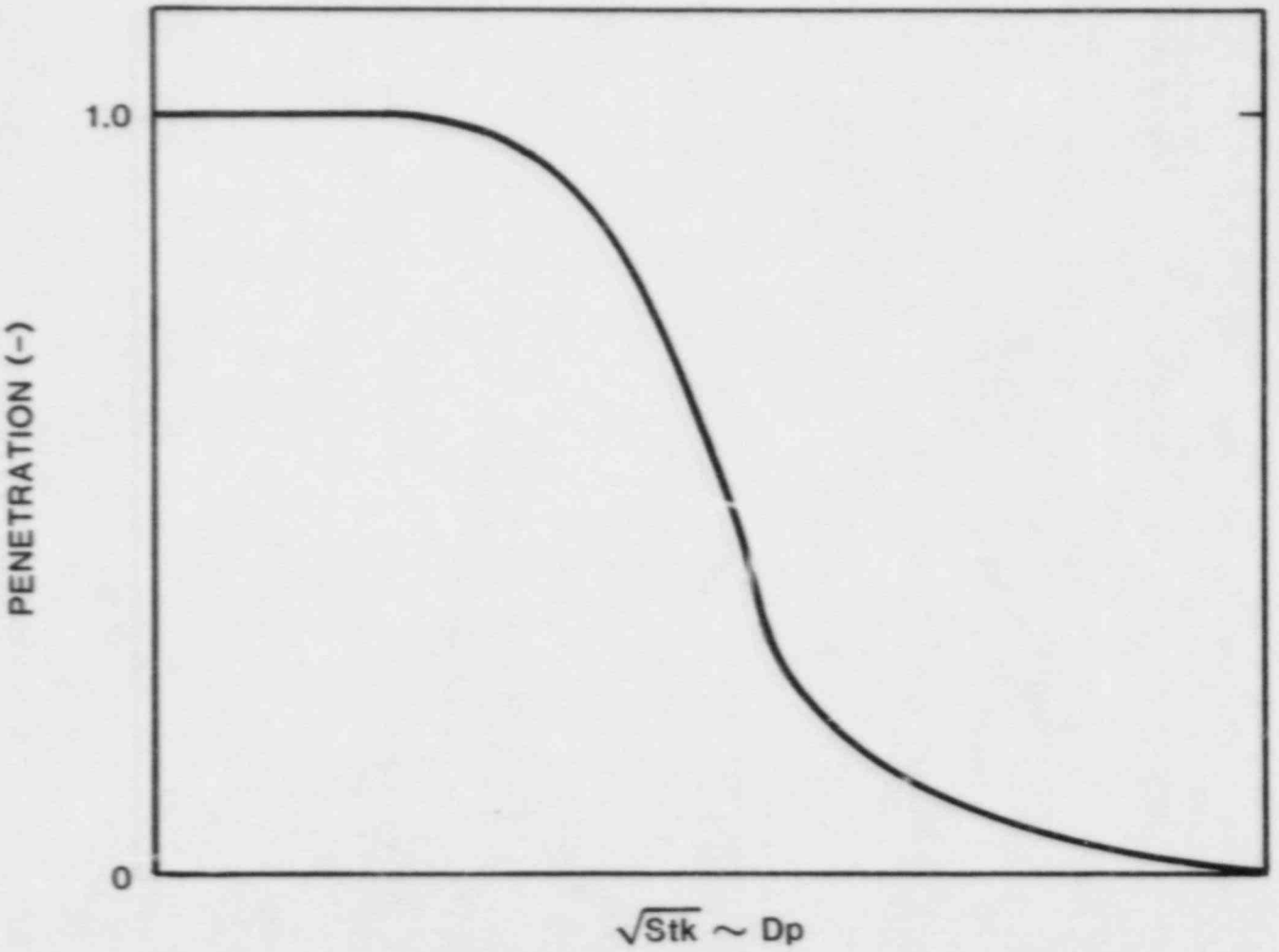

Figure 8. Particle Loss by Impaction

V. Experimental Programs

V.1 Program Overview

The results from the Phase I SPIT tests (described in Appendix A) have shown the behavior of a molten stream ejected at high pressure to be uncharacteristic of that hypothesized in the ZPSS. The SPIT jet geometry appears to be highly dynamic, dependent on the degree of gas in solution, ranging from coherent and stable to expanded and finely fragmented. The tests have demonstrated an unexpected aerosol source term accompanying the jet propagation, assumed to be caused by three or more separate mechanisms.

The Phase II SPIT test program is designed to perform the following experiments:

1) Perform jet and aerosol characterization tests.

2) Study the interaction of the jet stream with a water pool.

3) Conduct 1/20th-scale concrete cavity tests.

These test results will provide the majority of data concerning the dynamics of high-pressure melt ejection. The Phase II SPIT test matrix is outlined in the following section (V.2). Section VI discusses the experiments in more detail including the identification of the independent system variables and the development of the characterization test matrix using a factorial design approach.

The HIPS experiments are intended to provide experimental verification of the ZPSS' debris relocation mechanisms in a realistic, scaled geometry. The dimensions of the HIPS apparatus and test article represent a 1/10th linear scaling of the Zion plant geometry. The test matrix presented in Section V.3 is designed to provide data over the range of possible accident conditions. A limited number of characterization experiments are also included, to allow correlation to the more extensive results obtained from the Phase II SPIT tests.

The HIPS apparatus and equipment are discussed in Section VII along with the strategy used to develop the test matrix. The complexity and resources required for the HIPS experiments prevent using a large factorially designed test program.

V.2 SPIT Test Matrix

The SPIT characterization test matrix (Table 7) is based on a factorial design approach considering four independent input variables identified during the Phase I SPIT tests. The results of the matrix should demonstrate the influence of these variables

and their interactions on the behavior of the ejected melt stream and aerosol generation. The data will allow models to be developed and verified.

TABLE 7
SPIT Phase II Jet and Aerosol Characterization Matrix

Test	Pressure (MPa)	Gas	Approx. Temp. (^{o}C)	Jet Height (m)
1	6.3	N_2/CO_2	2250	0.9
2	17.0	N_2	3000	1.6
3	1.4	N_2	3000	0.2
4	17.0	CO_2	3000	0.2
5	1.4	CO_2	3000	1.6
6	17.0	N_2	1500	0.2
7	17.0	N_2	1500	1.6
8	17.0	CO_2	1500	1.6
9	1.4	CO_2	1500	0.2
10	6.3	N_2/CO_2	2250	0.9

The Phase II jet-water experiments are shown in Table 8. The tests are designed to identify the type of interactions and quantify their extent. The results are intended to be used for the selection of instrumentation devices for subsequent SPIT and HIPS scaled cavity experiments. The specific design and number of additional tests involving water is not known due to the uncertainty in the response of the system.

TABLE 8

SPIT Jet/Water Interaction
and 1/20th Scale Cavity
Test Matrix

Test	Pressure (MPa)	Configuration	Purpose
1	6.3	Deep water pool, directly contacting exit aperature	Determine steam bubble growth in "solid" water cavity
2	6.3	Aluminum 1/20th scale cavity, pool contacting exit aperature	Study dispersal of water pool and hydraulic forces in a "rigid" cavity
3	6.3	Concrete 1/20th scale cavity	Debris dispersal (dry cavity)
4	6.3	Concrete cavity with water pool contacting exit aperature	Debris dispersal (water present) jet/water interaction
5	6.3	Concrete 1/20th scale cavity shallow water pool	Interaction in partially filled cavity

The scaled concrete cavity test (Test 3) will provide information at 1/20th scale for use in subsequent modeling efforts. The experiment will also allow the verification of instrumentation techniques to be used on the HIPS tests. The damage incurred by the test article will determine if other tests on the same unit can be accomplished.

Additional test conditions for the matrix in Table 8 have not been defined, pending analysis of the results of the jet and aerosol characterization test matrix. The type of gas and the desired melt temperature will be chosen to obtain the maximum system response i.e. the most energetic jet/water interaction or the highest probability of debris dispersal. The results of either test matrix may dictate that additional experiments be performed in order to reduce uncertainties or study unexpected behavior.

V.3 HIPS Test Matrix

Scaling analyses of the mechanisms proposed in the ZPSS (Section IV) indicate that material dispersal is most influenced by the initial vessel pressure and temperature. The ZPSS dispersal mechanisms discount the presence of water in the cavity and do not allow for the influence of gas dissolved in the melt. Analysis of these latter two effects suggests that they may have a significant influence on the debris relocation phenomena. Table 9 identifies the critical variables influencing debris dispersal and their expected range.

TABLE 9
Critical Debris Dispersal Characteristics

Characteristics	Range (Extremes)
Pressure:	1.4 - 17.0 MPa
Melt Temperature:	1500°C - 2800°C
Water in Cavity:	dry - water filled
Gas Solubility:	low - high

A simple two-factorial test matrix of the input characteristics given in Table 9 would require 16 tests total, more than could be handled in a convenient manner. A fractional factorial scheme to find just main effects and not interactions of effects, and with no replication of data would require at least 8 tests. This number is also impractical under the scope of the Phase I HIPS testing.

The HIPS test strategy is therefore based on establishing the existence of the dispersal mechanisms by isolating main effects. The technique for accomplishing this is illustrated by a logic decision circuit given in Section VII (Figure 28). The intent of the circuit is to provide a method of finding the range of test conditions where the ZPSS material dispersal mechanisms exist (or do not exist). The test matrix based on the logic circuit is given in Table 10.

TABLE 10
HIPS Test Matrix

Test	Melt Mass (kg)	Expected Temperature (^{o}C)	Pressure (MPa)	Gas	Cavity	Remarks
1	80	2400	17.0	N_2	No cavity	Jet and aerosol characterization
2	80	1800	1.4	CO_2	No cavity	Jet and aerosol characterization
3	80	2400	17.0	N_2	MgO	Most probable debris dispersal conditions, MgO cavity
4	80	2400	17.0	N_2	Concrete	Most probable dispersal conditions, concrete cavity
5	80	1800	1.4	N_2	Concrete	Least probable dispersal conditions
6	80	1800	17.0	N_2	Concrete	Determine effect of temperature
7	80	2400	1.4	N_2	Concrete	Determine effect of pressure
8W	80	2400	17.0	N_2	Concrete	Water-filled cavity
9W*	80	2400	17.0	N_2	Concrete	Partially-filled cavity

* Possible inclusion in matrix depending on Phase II SPIT test results.

The matrix is initiated by performing two characterization tests that bound the expected temperature, pressure, and gas solubility ranges. They are followed by a test using initial conditions assumed to be most favorable for the existance of the relocation mechanisms. For the purpose of illustration, these conditions are the highest temperature, pressure, and gas solubility values within the prescribed range. Presumably, the SPIT jet characterization tests will provide a basis for establishing the degree of gas solubility associated with a set of test conditions, and the influence of dissolved gas on the dispersal

mechanisms. The cavity will be constructed of magnesium oxide to eliminate energetic concrete decomposition phenomena to minimize disruption of the dynamic debris configuration. The presence of water in the cavity is considered in another portion of the logic network.

The results from the HIPS tests numbers 3 through 7 will establish the principal main effect on debris dispersal mechanisms. The Phase II SPIT data will be used in conjunction with these results to quantify the secondary effects that are also involved.

The "dry-cavity" tests described above represent a lower bound on the possibilities regarding the presence of water. The opposite extreme is when the cavity is completely filled with water, to the lower extremity of the pressure vessel. Test HIPS-8W is designed to study this condition where melt is ejected under high pressure into a "water-locked" cavity. The objective of the test is to determine the influence water has on debris dispersal. All previous paths in the logic circuit are subsequently directed along this branch, regardless of previous outcomes.

The HIPS-8W test is applicable only to a completely filled cavity, a partially-filled cavity may behave quite differently from either this or the dry cavity case. The behavior of a shallow water pool will be addressed in the jet/water test matrix of the Phase II SPIT experiments. The results of the SPIT tests may suggest that a partially-filled cavity must be considered as a distinct, third class of experiments. In that event, HIPS Test 9W will be conducted to study the effect of a limited-water pool.

Included in the HIPS test matrix are jet and aerosol characterization experiments to provide correlation with similar SPIT experiments. Characterization tests are necessary to confirm the existence of the SPIT mechanisms at a larger scale and to provide data for scaling analyses. If significant differences are noted in the larger 1/10th scale HIPS jet and aerosol tests, additional characterization tests may be required.

The test matrix is not intended to provide definitive information about all possible combinations of accident conditions, only those factors that appear to be most critical to the debris dispersal mechanisms. By studying the extremes of the spectrum of possibilities for these factors, statements concerning the bounds of potential test outcomes can be made.

VI. System Pressure Ejection Tests (SPIT)

The results from the Phase I SPIT tests (described in Appendix A) have shown that the ejected melt jet is not a coherent, stable stream as hypothisized in the ZPSS. The behavior of the jet appears to be highly dynamic and dependent in part on the initial conditions within the melt generator. The results also suggest a number of aerosol generation mechanisms are active during the ejection process. These aerosols may cause a significant source term separate, and distinct from the in-vessel or melt/concrete mechanisms.

The second phase of the SPIT testing is designed to provide a cost effective study of the behavior of high pressure melt ejection. It is also a method for obtaining quantative results, in scale, concerning jet/water and jet/concrete cavity interaction. The following subsections describe the SPIT apparatus and instrumentation and the salient features of the test matrices.

VI.1 SPIT Apparatus Description

This section describes the SPIT melt generator and the associated facility components. It also includes a discussion of the melt composition and temperature.

VI.1.1 Melt Generator Assembly and Testing

The SPIT melt generator is designed to create a high-temperature melt within a pressurized, confined volume. The requirement for the high strength associated with pressure vessels is generally not compatible with devices capable of withstanding high temperature. To accomplish the design objective, it is necessary to separate the melt from the pressure-bearing component.

The SPIT generator design is shown in Figure 9. The pressure vessel is fabricated from a 12.7-cm-OD by 11.4-cm-ID mild steel pipe section capped on each end by welded flanges and bolted covers. The rated maximum working pressure of the vessel is 17.0 MPa. The melt crucible consists of a mild steel pipe section (10.2-cm OD x 8.9-cm ID) capped by graphite plates on each end, placed inside the pressure vessel. The annular volume between the melt crucible and pressure vessel wall is filled with a refractory, alumina-based, dry-ram powder. The lower vessel flange cover is threaded to accept a fusible brass plug normally 3/4" NPT. The lower graphite plate (6-12-mm thick) is designed to surround the melt plug and expose only the top surface to the melt. The top graphite plate is drilled to allow gas to enter into the melt crucible.

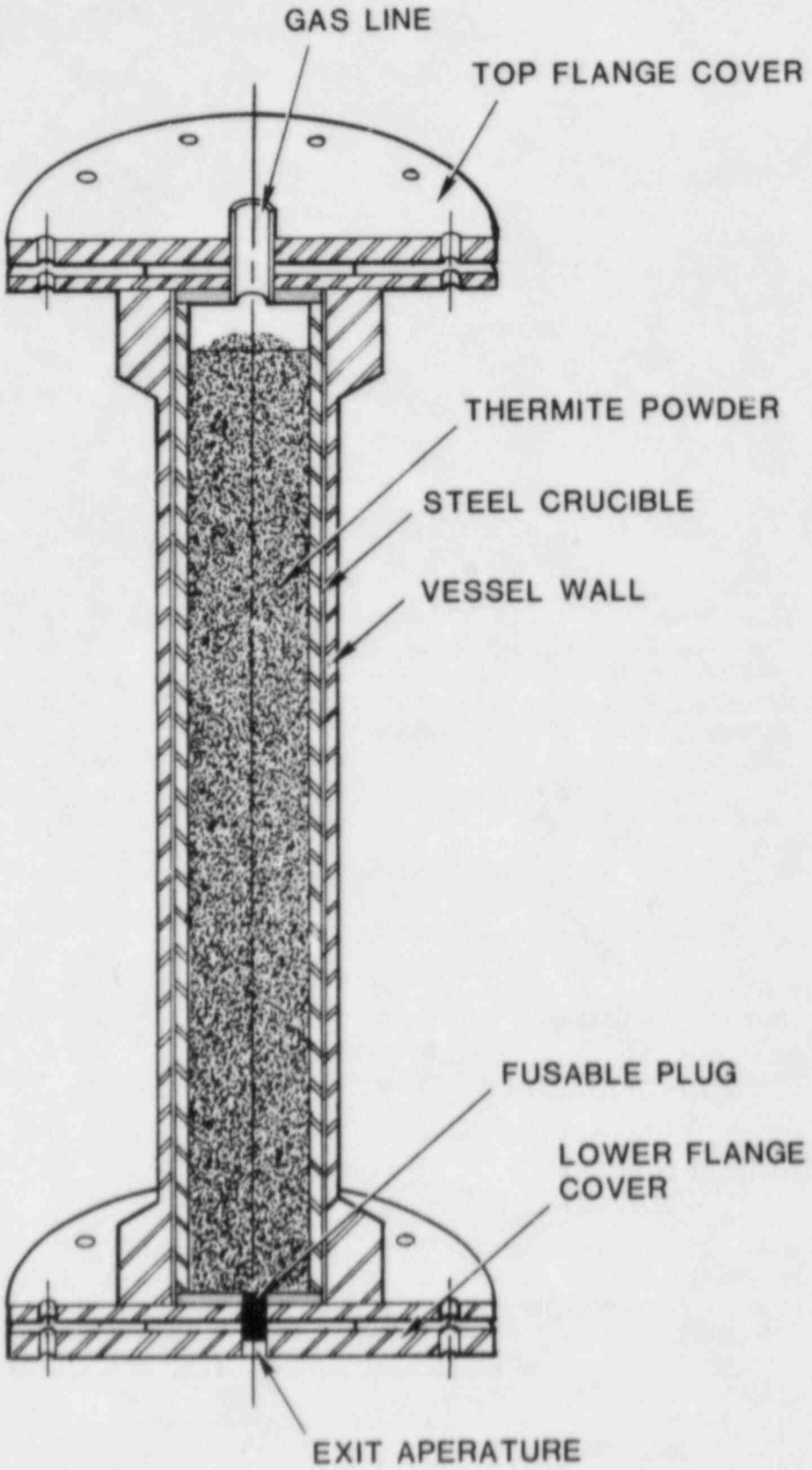

Figure 9. SPIT Melt Generator

Assembly of the melt generator is performed with the top flange cover removed. After the brass plug is installed and the lower graphite plate dropped into place, the steel inner liner is lowered atop the lower graphite disk. The dry-ram powder is poured into the gap between the two vessels. The thermite powder is then gradually poured into the inner liner and lightly tamped to improve settling. The capacity of the melt generator is approximately 10.5 kilograms using an Fe_3O_4/Al thermite mixture (nominal density 2.2 g/cc). When the thermite is in place, an igniter wire is embedded into the top surface of the powder to a depth of 1-2 cm. The igniter leads are kept sufficiently long (~20 cm) to allow attachment to electrical feed throughs placed in the top flange cover. After the top graphite cover is placed in position, the top flange cover is bolted onto the pressure vessel.

The test sequence is initiated by charging the accumulator and melt generator to the desired pressure. A transducer located in the upper flange cover monitors the pressure in the vessel with the output of the device recorded on a transient digitizing recorder, a high-speed FM recorder, and active readout panels. When the preset pressure level is achieved, the pressure source is terminated and the thermite reaction is initiated. A 28-VDC battery is used to cause an intermetallic reaction of the igniter, creating localized temperatures (in excess of 2700°C) in the vicinity of the igniter. The thermite requires temperatures greater than 800°C for the reaction to proceed.

The burn front propagates downward with a typical velocity of nominally 2.5 cm/sec, although this value can vary depending partly on the extent of tamping performed during the loading operation. A high degree of tamping apparently improves the heat transfer within the powder bed, causing the reaction front to propagate at a higher velocity. When the reaction front reaches the bottom of the crucible, the melt plug quickly fails and the molten material is forceably ejected from the vessel.

Post-test inspection of the melt generator shows the interior to be virtually devoid of any melt remains. Visual estimates indicate less than 5% of the melt left in the generator. Some additional residue is found in the expansion volume between the top graphite cover and the upper flange. This material appears to be ash-like and is assumed to be made up of contaminants from the melt or nonstoichiometric compounds and comprises less than 0.5% of the total melt mass. The inner steel liner is usually penetrated in several locations, but the dry ram is an effective protection for the vessel wall. In general, the aperture in the bottom flange corresponds to the outer diameter of the plug, approximately 2.5 cm. Slight erosion of the steel insert normally occurs, sufficient to obliterate the internal threads in the aperature. Small amounts of residual melt are deposited in this location, possibly by material dripping down into this area after the ejection process is completed.

VI.1.2 Interaction Chamber

For the Phase II testing, the melt generator will be placed in a large steel chamber similiar to that shown in Figure 10. The chamber allows containing and measuring the products, particularly aerosols, of the experiment. The melt generator is mounted on three load cells that are supported by the "roof" of the chamber. Thus, the top flange of the device is outside the chamber for ease of assembly while the lower flange and exit aperature are within the structure. The height of the generator also permits longer jet propagation distances, a desirable feature in the study of aerosol generation (see discussion in Section VI.2.)

The chamber is constructed of 1/4" thick steel plate with 6" I-beams on 26" centers for reinforcement. The large round opening in the side of the structure is used to house a junction box for instrumentation and control wiring. The cables terminate in the control center building located approximately 20 meters from the apparatus. The large covers on either end of the chamber are bolted into place with gaskets between the mating surfaces to insure sealing. The floor of the structure is comprised of a reinforced concrete pad, nominally 6" thick. A relief valve is used to prevent internal pressures from exceeding 0.2 MPa. The maximum working pressure of the chamber is estimated to be 0.3 MPa.

For the 1/20th scale cavity tests, the melt generator will be removed from the roof of the chamber and bolted to the test article. The test article will then be placed near one end of the interaction chamber. The exit of the cavity will be directly away from the near end so that the ejected debris will be free to expand away from the test device.

VI.1.3 Pressurization System

The SPIT apparatus uses either nitrogen or carbon dioxide to pressurize the melt generator. The gases are supplied by commerical storage bottles feeding separate manifolds. The output of each manifold passes through a manual shutoff valve to a common pressure regulator (see Figure 11). The regulator in turn feeds into an accumulator volume and then to the melt generator through a remote control shutoff valve. The accumulator is included in the system to mitigate potential pressure increases caused by liberated gas during the thermite reaction.

Experiments requiring pressures higher than can be conviently provided by the gas bottles will use a gas intensifier incorporated into the system. The pressure rating of the intensifier is much greater than the maximum required for the testing. The device will charge the accumulator and melt generator directly when test pressures above 10 MPa are needed.

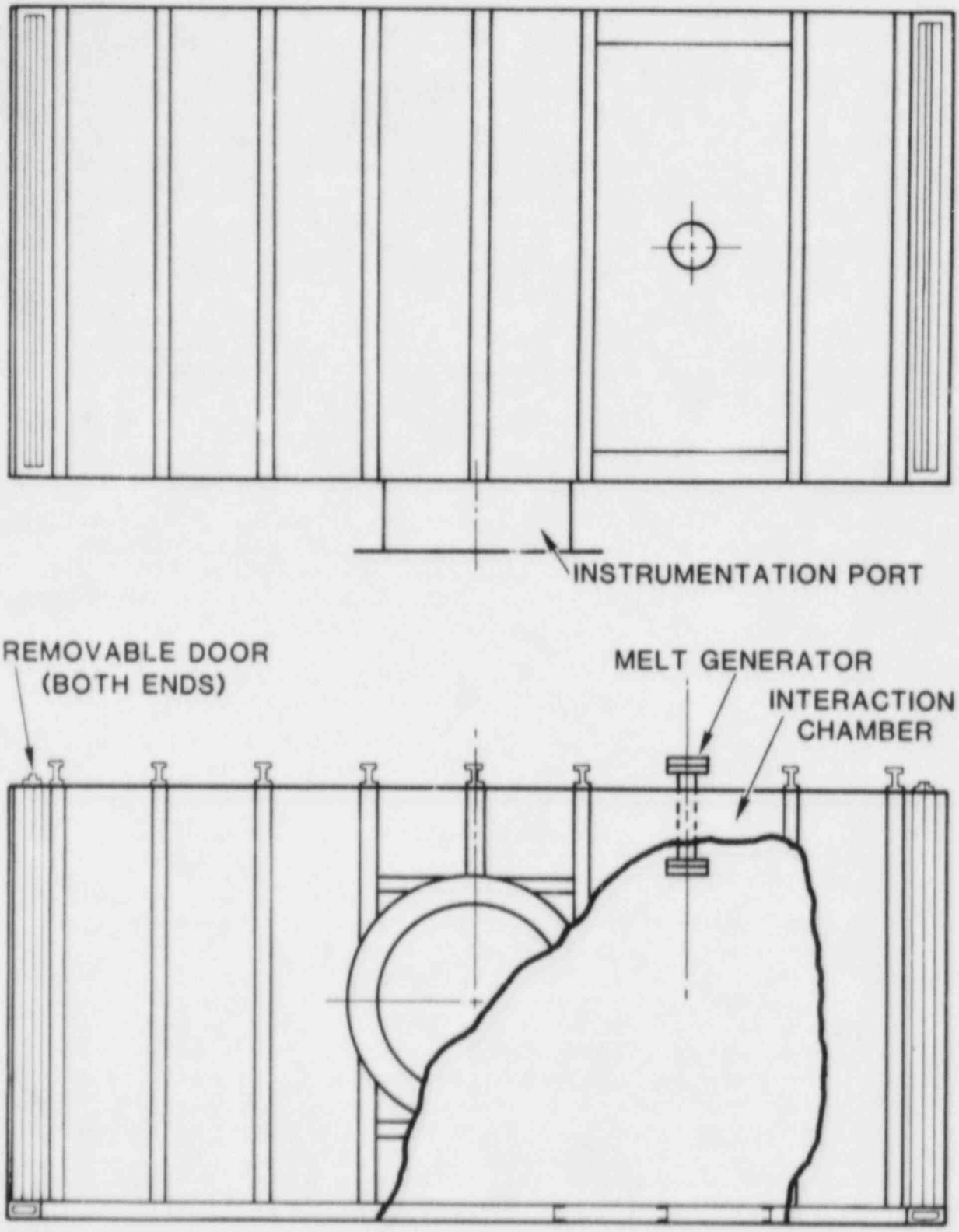

Figure 10. Schematic Showing Relationship of Melt Generator and Interaction Chamber

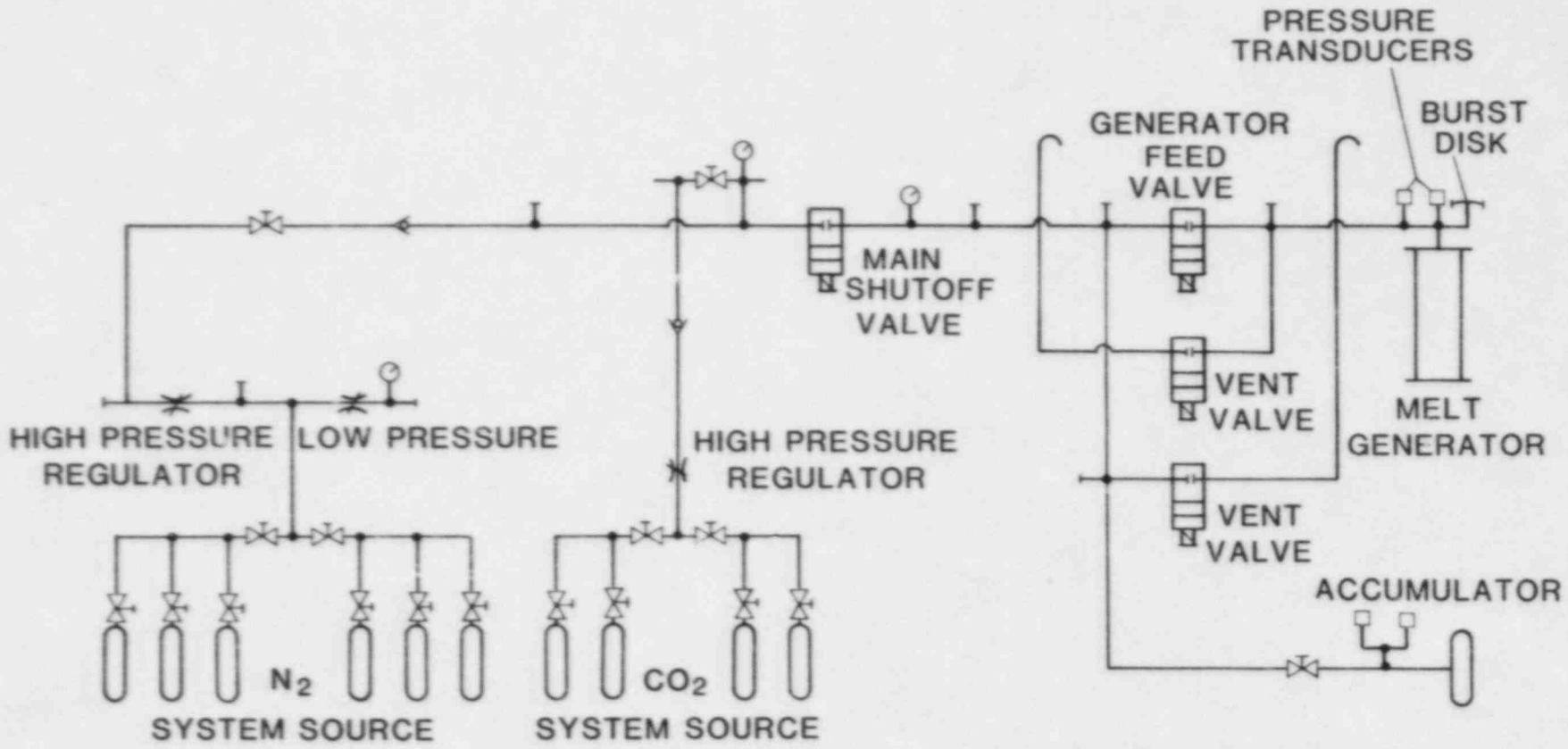

Figure 11. Pressure System Schematic

The pressurizing system is operated from the control center via remotely controlled valves. Remote transmitters for monitoring pressure levels are used at the gas manifolds and at the melt generator.

VI.1.4 Melt Composition and Temperature

The melt used in the SPIT tests is produced by the metallothermitic reaction of iron oxide and aluminum:

$$3Fe_3O_4 + 8Al \rightarrow 9Fe + 4Al_2O_3 + \text{heat} \qquad \text{(VI-1)}$$

the energy equivalence of a stoichiometric reaction is approximately 876 cal/g. The reactants are in the form of powders that are mixed just prior to the test. The temperature achieved by the mixture is assumed to be limited by the vaporization of one of the reaction products (Ref. 16). The completeness of the reaction depends on the details of mass, geometry, containment and pressure imposed on the reactants. For reactions that proceed to less than 85% completion, the behavior of the excess aluminum controls the maximum temperature. Reactions beyond this point liberate sufficient energy to vaporize the excess aluminum. The reaction must proceed to 94% for the boiling of the iron to control the temperature. At pressure, the boiling of iron is suppressed and temperatures as high as 3300 K may be achieved.

Considering the above reaction, the amount of heat liberated can be used to determine the maximum temperatures of the reactants,

$$3Fe_3O_4 + 8Al \rightarrow 9Fe + 4Al_2O_3 + H_{Rxn(298)} \qquad \text{(VI-2)}$$

where $H_{Rxn(298)}$ is the enthalpy of reaction at 298 K.

The maximum temperature can be found by:

$$- H_{Rxn(298)} = H_{Ref} + M_{Fe} \int_{T_{ref}}^{T} c_p \, dt + M_{Al_2O_3} \int_{T_{Ref}}^{T} c_p dt \qquad \text{(VI-3)}$$

where

$$H_{Ref} = M_{Fe}\left(H_{(T_{ref})} - H_{298} \right)_{Fe} + M_{Al_2O_3} \left(H_{(T_{ref})} - H_{298} \right)_{Al_2O_3} \qquad \text{(VI-4)}$$

where:

M_{Fe} = moles of iron

$M_{Al_2O_3}$ = moles of alumina

Handbook values (Ref. 17) are used to give:

$$H_{Rxn(298)} = -797900 \text{ cal}$$

$$c_p(Fe) = 10.74 + 4 \times 10^{-4} (T - T_{Ref})$$

$$c_p(Al_2O_3) = 34.63 \text{ cal/mole K.}$$

Assuming the reaction goes to completion,

$$797900 = 9 \left(H_{(T\ Ref)} - H_{298}\right)_{Fe} + 4 \left(H_{(T\ Ref)} - H_{298}\right)_{Al_2O_3}$$

$$+ 9 \int_{T_{Ref}}^{T} \left(10.74 + 4 \times 10^{-4} (T - T_{Ref})\right) dt + 4 \int_{T_{Ref}}^{T} 34.63\ dt \qquad \text{(VI-5)}$$

If T_{Ref} is selected to be 2400 K

$$\left(H_{2400} - H_{298}\right)_{Fe} = 23917 \text{ cal/mole Fe}$$

$$\left(H_{2400} - H_{298}\right)_{Al_2O_3} = 91929 \text{ cal/mole } Al_2O_4$$

and

$$797900 = 9 \left[23917 + 9.78\ (T - 2400) + 2 \times 10^{-4} (T^2 - 2400^2)\right]$$
$$+ 4 \left[91929 + 34.63\ (T - 2400)\right] \qquad \text{(VI-6)}$$

If the process is assumed to be adiabatic, then the maximum energy released is 876 cal/g. This value could cause up to 5% of the iron to be boiled, if the pressure does not suppress the process.

Maximum melt temperature above the iron boiling point is a concern if the iron "flashes" as the melt is discharged into the ambient environment. Iron flashing could then serve as potential source of non-prototypic aerosol-like material during the melt discharge. Non-reactive materials can be added to the thermite mix to insure that the maximum melt temperature is below the iron boiling point. Ten percent, by weight, of iron powder will lower the temperature by an additional 150 K, a reduction in heat output sufficient to insure that flashing does not occur.

VI.2 Jet and Aerosol Characterization Tests

The jet and aerosol characterization test matrix given in Table 7 is developed to obtain the response of the system over the range of conditions considered possible in reactor accident scenarios. The results will be used to develop and verify an analytical model of the jet behavior that can be used to predict behavior at larger scales.

VI.2.1 Information Sought

The purpose of the characterization test matrix is to provide a correlation of the jet behavior to the initial conditions of pressure, temperature, and melt and gas composition. The results will be used to develop an analytical model to predict the jet behavior over the input range under consideration. The tests are also designed to determine the extent of aerosol generation during melt ejection and the ability of these aerosols to transport fission products out of the melt. The characterization test matrix will determine the extent of aerosol in the experiments and the type and quantity of fission products in the aerosol, over the projected range of accident conditions.

Table 11 presents the types of information sought from the jet and aerosol characterization test matrix. The list is compiled by reviewing the variables involved in the analytical models describing melt removal mechanisms, aerosol transport in containment, and the effect of aerosols on engineered safety features.

TABLE 11
Information Sought from the SPIT Jet
and Aerosol Characterization Test Matrix

Variable	Phenomena Affected
Gas Pressure in Melt Generator	Gas solubility Jet velocity Gas velocity
Gas Temperature in Melt Generator	Gas solubility Gas velocity
Melt Temperature	Gas solubility Melt density Incident heat flux
Gas Solubility	Aerosol source term, Dynamic jet configuration

TABLE 11 (Cont.)
Information Sought from the SPIT Jet
and Aerosol Characterization Test Matrix

Variable	Phenomena Affected
Jet Velocity	Dynamic pressure Mass flow rate Debris configuration Incident heat flux Aerosol source term *Penetration velocity
Jet Configuration	Incident heat flux Dynamic debris configuration *Water interaction *Fragmentation
Incident Heat Flux	Jet/concrete interaction Concrete decomposition/gas generation *Jet/Water interaction
Reaction Forces	Mass discharge rate Jet density
Gas Velocity	Debris removal Aerosol transport *Water purge
Aerosol Composition, Size, Mass, Concentration	Fission product transport Aerosol source term *Water pool scrubbing

* Applicable to situations involving a water pool.

VI.2.2 Instrumentation

Melt-ejection experiments involve a combination of events with time durations ranging from tens of seconds (thermite reaction) to submillisecond (flash x-ray exposure). This characteristic, combined with the high temperature and pressure of the jet stream, requires the use of a number of unique devices to perform the required measurements. Table 12 summarizes the devices that will be used and the paragraphs below describe them in detail.

TABLE 12

INSTRUMENTATION FOR SPIT CHARACTERIZATION TESTS

Measurement	Device	Range	Number-Location	Remark
Gas Pressure	Pressure transducer	2000 psi or 10,000 psi	1 - gas line 1 - vessel flange cover	Placed near accumulator Thermally Shielded
Gas Temperature	Thermocouple	1400°C	1 - Generator expansion volume 1 - Gas Line	Shielded
Melt Temperature	Thermocouple	1400°C	6 - Crucible sidewall	Used to infer temperature via inverse heat-conduction analysis
Jet Temperature	Pyrometer	3300°C	2 - Exit aperature	Focused on melt jet at aperature
Jet Velocity	Framing Camera	-	3 - Outside chamber	
Jet Configuration	Flash x-ray	-	4 - Film cassettes near (1 m) apparatus	70-nsec exposure time
	Framing Camera	-	3 - Outside chamber	View obstructed by vapor and aerosol clouds
Reaction Forces	Load cells	8896 Nt	3 - Supporting generator	
Incident heat flux	Calorimeter	-	1 - Target plane - directly under jet stream	Multiple elements, Temperature data used to infer heat flux
Aerosol *				

* See Table 13

VI.2.2.1 Gas Pressure and Temperature

A transducer placed in the top flange cover of the melt generator (Figure 9) measures the pressure of the gas in the expansion volume above the melt. The record obtained from this device gives a precise indication of the gas pressure forcing the melt out of the vessel. A second, duplicate transducer is placed in the gas line near the accumulator (Figure 11). This location is chosen for two reasons; one, the device is physically isolated from the high temperature source so that thermal effects on the gauge are minimized and two, the recorded pressure history provides an indication of the flow restriction caused by the small diameter gas line.

Appendix B contains an analysis that shows the gas line acts as a low-pass acoustic filter during blowdown of the melt generator. The results indicate that the accumulator volume does not contribute significantly to the gas flow out of the melt generator for the period immediately following melt ejection.

Gas temperature is obtained by placing thermocouples in locations adjacent to the pressure transducers described above. The thermocouple in the gas line is a standard type K with a 1.6 mm diameter stainless steel sheath. The hostile environment existing in the expansion chamber during the thermite reaction requires that the second thermocouple be shielded by placing it within a 6 mm diameter stainless steel tube. The end of the tube is sealed and numerous 1-1/2 mm diameter holes are drilled in the side of the tube to permit gas flow to the sensor. The design is effective in mitigating damage to the thermocouple caused by molten thermite particles. The mass of the shield combined with the small diameter of the gas holes causes the response of the device to be slower than the comparable, unshielded device.

VI.2.2.2 Melt Temperature

Melt temperature cannot be measured directly in the generator because of the rapid evolution of very high temperatures and the corrosive nature of the melt composition. Common thermocouple materials such as stainless steel cannot survive the high temperatures. Sheath materials capable of resisting the chemical attack are typically thermally shock-sensitive and will fail mechanically during the thermite reaction. Limitations in access to the melt crucible and the presence of opaque gases precludes the use of optical pyrometry. The alternative to direct measurement is the use of some other technique to infer the temperature of the melt.

Thermite reactions have been observed to be highly agitated, probably because of the rapid expansion of trapped gas through the melt pool. Thus, it is assumed that the thermite reaction time is short relative to the time required for the melt to calm

and develop large thermal gradients. The temperature of the mixture is then nearly isothermal. Because the thermal conductivity of the steel shell is on the same order as the molten thermite, monitoring the crucible wall temperature may allow inferring the melt temperature. Thermocouples are inserted into the crucible wall at several depths and at various elevations, to obtain the temperature gradient as a function of time. The thickness of the steel between the melt and the thermocouple is adequate to protect the sensor during the thermite reaction. The mass of the steel also causes the initial temperature transient imposed on the steel to be delayed in time at the locations of the thermocouples. The delay limits the maximum temperature at the sensor location and reduces the slope of the temperature-time curve.

The steel crucible tube can be modeled as an infinite cylinder with a time-varying heat flux imposed on the inner radius and an adiabatic outer surface. It is also assumed that the melt is highly turbulent during the reaction, so that the heat transfer at the inner surface is dominated by conduction across the interface. Applying an energy balance to the control volume defined by the cylinder wall gives:

$$\dot{E}_{in} - \dot{E}_{out} = \dot{E}_{stored} \qquad \text{(IV-7)}$$

For an adiabatic outer surface, $\dot{E}_{out} = 0$ and the equation can be written:

$$-k2\pi rL \frac{\partial T}{\partial r} = \left(r_o^2 - r_i^2\right) L \rho c_p \frac{\partial T}{\partial t} \qquad \text{(VI-8)}$$

Converting the differentials to a finite difference notation gives:

$$\frac{2k(T)}{\ln (r_o/r_i)} \left[T_i^t - T_o^t\right] = \left[r_o^2 - r_i^2\right] \rho c_p \left[T_o^{t+1} - T_o^t\right] \qquad \text{(VI-9)}$$

where:

$k(T)$ = thermal conductivity of steel as a function of temperature

T = temperature of the shell

r = cylinder radius

subscript o,i = outside, inside cylinder surfaces

superscript t+1,t = time interval

ρ, c_p = density and specific heat of steel

The analysis considers the temperature at the inner surface of the liner is to be approximately the same as that of the melt and that melting of the steel does not occur. Placing thermocouples in the steel shell allows obtaining the temperature history T(t) at various radial and axial locations. These data can then be fit numerically to obtain $T_i(t)$ to infer melt temperature.

A numerical technique (Ref. 18) is used to solve the equation (VI-9) by using a boundary condition of the form:

$$T(r_o, t) = Y_i(t) \qquad i = 1, 2, \ldots N$$

where:

N = the number of thermocouples.

The above equation is solved numerically using finite control sizes and a fully implicit technique. When multiple thermocouples and/or future temperatures are considered, the heat flux that minimizes the following least-squares error is determined:

$$E = \sum_{j=n}^{n+4} \sum_{i=1}^{n} \left[T(r_i, t_j) - Y_i(t_j) \right]^2 \qquad \text{(VI-10)}$$

where:

n = the number of future times considered

The output from the code is either the heat flux or temperature at the inner surface of the crucible wall.

VI.2.2.3 Jet Stream Temperature

The temperature of the jet stream and/or vapor cloud outside the vessel is difficult to measure because of the high temperatures involved and the rapidly changing nature of the stream. Most direct contact thermometry techniques will not function at the anticipated temperatures (>2500 K) and may be hampered by slow response times. The response time requirement for the SPIT jet stream measurements can be established by considering the gage behavior to a step-change in temperature. Assuming an exponential form for the governing equation:

$$T_{meas} = T_{act} \left[1 - \exp \frac{-t}{\tau} \right] \qquad \text{(VI-11)}$$

where:

T_{meas}, T_{act} = measured and actual stream temperatures

t = point in time when T_{meas} is obtained

τ = time constant of the device

The time constant is defined as the period corresponding to: $0.1\ T_{act} \leq T_{meas} \leq 0.9\ T_{act}$. Substituting these values into equation (VI-II) gives:

$$0.1\ T_{act}: \quad t_1 = 0.1$$

$$0.9\ T_{act}: \quad t_2 = 2.3$$

$$\tau = 0.45\ (t_2 - t_1)$$

The above analysis shows that in order to measure a step change in T_{act}, the time constant of the pyrometer must be less than half the risetime of the pulse to insure proper frequency response.

If all the melt passing the sensor location is at the same temperature, then the device need only respond in the period of time required to eject all the material. Temperatures varying with time within the stream will require that the time constant be proportionally smaller.

At the highest ejection velocity, the total melt ejection period is on the order of 50 ms. For illustration, assume that the pyrometer should have response to changes in time intervals corresponding to 1% of the total ejection time:

$$t = 0.01\ (50\ ms) = 0.05\ ms$$

The time constant and natural frequency (f_n) (Ref. 19) required for this example is then:

$$\tau = 0.45\ (t-0) = 0.45\ (5 \times 10^{-4}) = 0.2\ ms$$

$$f_n = \frac{1}{2\pi\tau} = \frac{1}{2\pi(0.2 \times 10^{-3})} = 144\ hz$$

A commercial pyrometer* selected for the SPIT experiments has a 1 microsecond response time with a temperature range up to

---

* Model 8000-1, Thermogage, Inc., Frostburg, MD.

3300°C. The device is limited, however, in that it assumes the source is radiating as a blackbody. The spectral emissivity of the melt stream must be known to correct the measured result. The relationship between the measured and actual temperature measurement is given by:

$$E_b(T)_{actual} = \varepsilon_\lambda(\lambda, T)\, E_b(T)_{measured} = \varepsilon_\lambda(\lambda, T)_\sigma\, T^4_{meas}$$

or

$$T^4_{meas} = \frac{1}{\varepsilon_\lambda(\lambda, T)}\, T^4_{act}$$

where:

$E_b(T)$ = total emissive power

σ = Stephan-Boltzman constant

T = absolute temperature

$\varepsilon_\lambda(\lambda, T)$ = spectral emissivity

The spectral dependence of $\varepsilon_\lambda(\lambda, T)$ for a molten thermite jet must be known to evaluate the error associated with assuming a constant emissivity. If the pyrometer is sensitive to all wavelengths, then measured temperature is related to the true temperature by the expression:

$$T_{meas} = T_{act}\, (\varepsilon_\lambda)^{-1/4} \qquad \text{(VI-12)}$$

The uncertainty in the data is a function of the difference between the assumed and actual emissivity value. This is given by the expression:

$$T_{act} = C\, (\varepsilon)^{-1/4} \qquad \text{(VI-13)}$$

where:

$$C = \text{constant} = \left(\frac{E_b}{\sigma}\right)$$

The error in temperature is then:

$$\frac{ET_{act}}{T_{act}} = \frac{1}{4}\left(\frac{E\varepsilon}{\varepsilon}\right) = \frac{1}{4}\left[\frac{(\varepsilon_{act} - \varepsilon_T)}{\varepsilon_T}\right] \qquad \text{(VI-14)}$$

where:

$E\varepsilon$ = uncertainty in the emissivity value

T_{act} = actual temperature

ε_T = assumed emissivity

ε_{act} = actual emissivity

Over the range of temperature 1500-3000° K, and assuming that $0.3 < \varepsilon < 0.8$, the maximum temperature error (ET/T) can be as high as 42%. Thus a good estimate of the emissivity is needed to insure accurate temperature measurement.

Pyrometric measurements in the SPIT tests are also complicated by the presence of the vapor cloud surrounding the melt stream. If the device is placed at a distance from the apparatus, the view may be obscured by the vapor cloud accompanying the melt stream. Placing the device on the lower flange cover allows an unhindered observation of the jet as it emerges from the vessel.

Measuring the temperature of the jet as it emerges from the vessel should provide data to correlate with the in-vessel measurements. As the jet propagates downward, the loss of energy by radiation and convection to the environment may cause the temperature to be significantantly reduced prior to impacting the target or cavity floor. An estimation of the jet temperature as a function of various experimental conditions is given in Appendix C. The results of the analysis indicate that the energy loss via radiation and convection from the melt jet to the environment is insignificant for all but the limiting case of a purely gravity-driven melt. Measuring the stream temperature at the exit aperature should then provide a good overall indication.

VI.2.2.4 Jet Velocity

The velocity of the jet stream is important because it determines the dynamic configuration of the debris on the cavity floor. It also determines the time for aerosol evolution to occur. It is assumed in the ZPSS that the velocity can be estimated by applying Bernoulli's equation across the vessel aperture. The equation is of the form:

$$\left(P + 1/2\ \rho V^2 + \rho gY\right)_1 = \left(P + 1/2\ \rho V^2 + \rho gY\right)_2 \qquad \text{(VI-15)}$$

where:

P = pressure
ρ = density
V = velocity
Y = elevation
g = acceleration of gravity

Subscripts 1 and 2 refer to the inside and outside of the vessel, respectively

If the change in elevation is neglected, and the density is assumed unchanged, the above equation reduces to:

$$V_2 = V_{jet} = \left[\frac{2(P_1 - P_2)}{\rho}\right]^{1/2} = \left[\frac{2P_1'}{\rho}\right]^{1/2} \qquad \text{(VI-16)}$$

where the velocity in the vessel is assumed to be negligible, and P_1' is defined in gage pressure.

Using the two extremes of pressure (1.4 and 17.0 MPa) gives the following:

For 1.4 MPa:

$$V_{jet} = \left[\frac{2(1.4 \times 10^6)}{5900}\right]^{1/2} = 21.6 \text{ m/sec}$$

For 17.0 MPa:

$$V_{jet} = \left[\frac{2(1.70 \times 10^7)}{5900}\right]^{1/2} = 75.9 \text{ m/sec}$$

These results represent the upper and lower bound for the prescribed set of accident conditions. The ZPSS predicts that the calculated velocity at the breach remains unchanged until impact with the floor or water pool.

VI.2.2.4.1 Turbulent Jet Theory

The analysis in the preceeding section does not consider the possibility of turbulent mixing of the jet and free-stream gas. Relative movement between a liquid and a gas will induce tangential separation surfaces at the interface. Resulting instabilities in the surface cause exchange of matter, momentum, and thermal energy. As a result, a region of finite thickness with continuous distribution of velocity, temperature, and species concentration is formed along the boundary of the two materials. The region is termed the turbulent jet boundary layer (Ref. 20).

A turbulent jet discharging into a stationary fluid is called a submerged jet. If the velocity field at the initial cross-section is uniform, the boundaries of the mixing layers

form diverging surfaces which intersect at the edge of the nozzle. The outside surface of the boundary is defined where, at all points, the velocity with respect to the direction of propagation is zero. The inner boundary is given by a constant velocity core that eventually disappears at some distance from the nozzle. Beyond this point, the velocity everywhere in the flow is a function of propagation distance. Figure 12 illustrates the appearance of an idealized submerged jet.

For a submerged, axially-symmetric jet of a single constituent, the length of the polar (core) region (Xp) and the thickness of the boundary layer (Y) are given by:

$$X_p = \pm \frac{r_o}{c(.214)^{1/2}} \qquad \text{(VI-17)}$$

$$Y = cx \left(0.416 + 0.021 \frac{(cx)^2}{r_o} \right)$$

where:

X_p = length of polar region

r_o = radius of nozzle

c = empirical proportionality factor

x = axial distance from nozzle

The value of c is typically 0.2-0.3 with 0.22 commonly used for submerged liquid jets (Ref. 20).

Considering, as an example, the calculation for 17.0 MPa, and r_o = 12.7 mm, the length of the transition region is:

$$X_p = \frac{12.7}{(0.22)\ 0.463} = 124.7 \text{ mm}$$

The length of the core region is therefore roughly 10 diameters. At this limiting value, the boundary thickness is:

$$Y_p = 0.22\ (124.7) \left[0.416 + \frac{0.021\ (0.22 \cdot 124.7)^2}{12.7} \right] = 45.6 \text{ mm}$$

This result suggests that the turbulent jet expands several times its initial size within the transition region. Beyond this

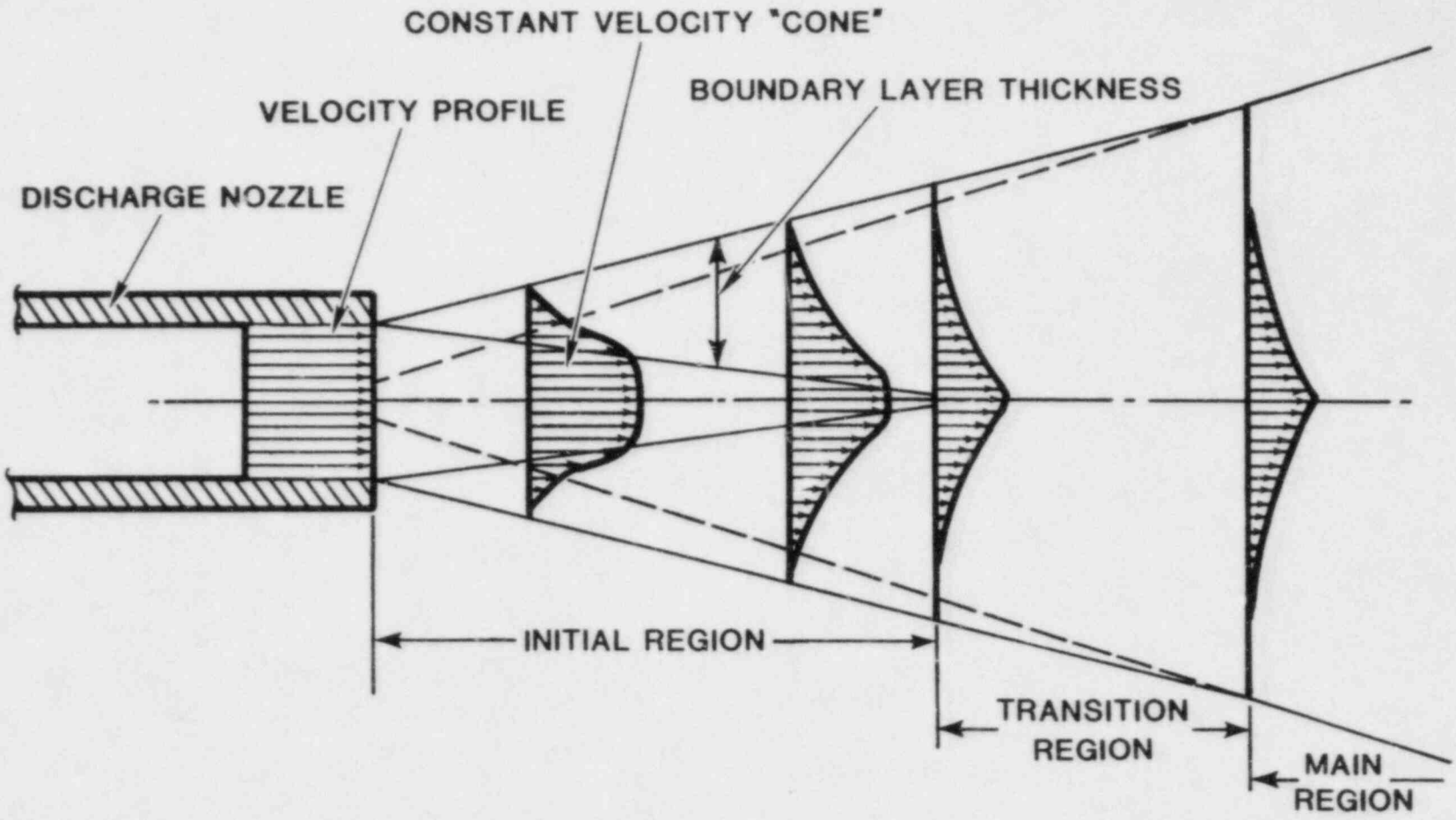

Figure 12. Diagram of a Submerged Jet

point, the centerline velocity (U_m) is given by the expression:

$$U_m = \frac{0.96\ U_o}{\frac{ax}{r_o}} \qquad \text{(VI-18)}$$

where:

U_o - initial velocity of jet

a - constant such that $ax_p/r_o = 0.96$

For the example above,

$$a = \frac{0.96\ (12.7)}{124.7} = 0.098$$

Equation (VI-18) reduces to:

$$U_m = \frac{124.4\ U_o}{x} \quad \text{for} \quad x > 124.7 \text{ mm}$$

The axial velocity is then inversely related to the propagation distance, for positions beyond the initial region of the flow. These results indicate that the melt stream may rapidly diverge from its initial diameter upon entering the atmosphere. The central, constant velocity core will diminish within a short distance beyond the exit aperature. The velocity field then becomes a function of both axial and radial position.

VI.2.2.4.2 Measurement Techniques

If the melt stream behaves as a turbulent jet, then velocity measurements must be referenced to the location of the aperature. Such measurements are complicated by the rapidly-expanding vapor cloud and a large radiant-heat energy accompaning the discharge.

Fast-framing motion picture techniques are commonly used to resolve the motion of high-velocity objects. In the case of the jet emanating from the melt generator, the expanding vapor cloud quickly obscures visual access to all but the leading edge of the melt stream. It is not certain that the behavior of the remaining portions of the melt stream correlates with the leading surface.

A flash x-ray technique is used primarily to obtain the configuration of the melt stream. The flash x-ray technique typically uses four separate heads in conjunction with corresponding film cassettes. The firing of each unit is accomplished

by individual trigger delay units referenced to a common signal such as a probe under the generator. The pulse width of the exposure is on the order of 70 ns, adequate to "freeze" the motion of even the highest-velocity jet. Velocity can be found by obtaining the propagation distance on two consecutive x-ray image photographs and dividing the resultant by the difference in the delay times for the two units.

The flash x-ray method is most applicable to observing a discrete portion of the melt, such as the leading edge of the jet. Distinct geometric features, later in time, rapidly evolve so that the resolution becomes increasingly more difficult to obtain. The technique also suffers in that only average velocity over the interval is obtained. If the jet is de-accelerating rapidly as turbulant jet theory predicts, then time-resolved velocity would be much more appropriate than average velocity.

VI.2.2.5 Jet Configuration

The dynamic jet configuration is obtained by penetrating the melt vapor and aerosol cloud that accompanies the ejection process. As described above, flash x-ray generators and film cassettes can be used for this purpose.

The resolution of an x-ray film image is based upon the geometric and film unsharpness. The former is caused by slight dislocation of the x-ray field near the edge of an object, such as the melt boundary. The latter effect is caused by movement of the object during the exposure period and the "graniness" of the film.

The geometric unsharpness, X_{12}, is given in Reference 21 as:

$$X_{12} = F\left(\frac{D_1}{D_o}\right) \qquad \text{(VI-19)}$$

where:

F = X-ray source spot-size

D_1 = object to film distance

D_o = source to object distance

For typical experiments:

$$X_{12} = 1 \times 10^{-3} \frac{(0.559)}{(1.83)} = 3.1 \times 10^{-4} \text{ m}$$

The film employed in the tests is very fine-grained so that the film unsharpness factor is dominated by the expression for movement of the melt. The jet movement is greatest for the highest predicted velocity:

$$X_{13} = Vt_x \qquad \text{(VI-20)}$$

where:

V = jet velocity
t_x = exposure time (x-ray pulse width)

$$X_{13} = 75.9\ (70 \times 10^{-9}) = 5.3 \times 10^{-6}\ \text{m}$$

The combined resolution of the x-ray image is then given by:

$$X_{11} = \left[\left(X_{12}\right)^2 + \left(X_{13}\right)^2 \right]^{1/2} = 3.1 \times 10^{-4}\ \text{m}$$

The analysis suggests that geometric features of the melt jet less than 0.3 mm will not be detectable on the x-ray images Thus, the small particles within the vapor cloud will not be detectable. The calculation also shows that the short pulse width of the x-ray exposure is very effective in "freezing" the jet stream.

VI.2.2.6 Reaction Forces

Expulsion of the melt from the vessel will cause a reaction force in the direction opposite the jet stream propagation. This force is monitored by three compression/tension load cells located between the chamber structure and the melt generator mounting plate. A simple free-body analysis shows that each cell is measuring one-third the difference between the weight of the vessel and the thrust produced by the expulsion of mass from the vessel.

The thrust on the vessel can be derived from conservation of momentum to be:

$$F_T = V_2 \frac{dm}{dt} = \rho A_2 V_2^2 \qquad \text{(VI-21)}$$

where:

F_T = thrust

V_2 = exit velocity

A_2 = Area of aperture

Knowing the quantities F_T, A_2, and V_2 permits the above relationship to be used to infer that the density of the molten jet stream as it exits the vessel. Because the equation is applied at the aperture, before significant expansion of the jet occurs, the thrust on the vessel should accurately determine the density of the melt in the stream.

The duration of the thrust forces is roughly equivalent to the period of time required to discharge the melt mass. Some force will be developed during gas discharge following the melt, but the gas density (and the force) is approximately 150 times less than the melt. The time required to expel 10 kg of melt can be estimated by assuming a constant mass flow (this is not strictly correct, because only the volumetric flow rate is constant for choked flow) through the aperture.

$$m_{total} = \int_{\emptyset}^{t_{final}} \dot{m}dt = A \int_{\emptyset}^{t_{final}} V(t)dt \qquad \text{(VI-22)}$$

where:

m_{total} = ejected mass during the interval $\emptyset$ to t

$\dot{m}$ = mass flow rate

t = time

For the highest pressure case, assuming constant velocity and the bulk melt density:

$$t_{final} = \int_{\emptyset}^{t_{final}} dt = \frac{m_{total}}{\rho AV} \qquad \text{(VI-23)}$$

$$= \frac{10 \text{ kg}}{5900 \text{ kg/m}^3 \ (5.12 \times 10^{-4}) \ (75.9)}$$

$$= 4.36 \times 10^{-2} \text{ sec}$$

The thrust can be calculated for the same conditions using Eq. (VI-22).

$$F_T = V\frac{dm}{dt} = V\dot{m} = 75.9 \text{ (m/sec)} \ 2.19 \times 10^2 \left(\frac{\text{kg}}{\text{sec}}\right)$$

$$F_T = 1.66 \times 10^4 \text{ Nt} = 3737 \text{ lb}$$

Each cell will measure approximately one-third of the above quantity minus the weight of the pressure vessel (2.2×10^3 Nt) or about 4.8×10^3 Nt.

VI.2.2.7 Heat Flux Calorimeter

In the high-pressure accident sequence proposed in the ZPSS, the melt ejected from the vessel impinges directly upon the concrete basemat. The heat flux transferred from the jet to the concrete is related to the extent of erosion and, hence, the amount of gas released. The resulting decomposition of the basemat and the quantity of gas released will affect the subsequent behavior of melt in the cavity. Extensive erosion may prevent debris configurations susceptable to removal by the proposed mechanisms. Likewise, gas emerging from a molten pool may be highly disruptive causing a very agitated, unstable configuration. The response of the concrete to the jet stream can then be an important parameter in determining the ultimate configuration of the core debris.

The incident heat flux will be measured during the SPIT tests using a slug-type heat flux calorimeter of the type shown in Figure 13. The device consists of up to four elements placed in a graphite body so that the front surface of each element is exposed. A close fit is maintained between the elements and the body to accurately simulate a semi-infinite body. A graphite face plate is attached to the body so that the front surface of each element is flush with the face plate. The sacrificial face plate and elements undergo extensive damage and are replaced for each test.

Each element is instrumented with three Type-K thermocouples constructed of AWG-32 gauge wire (0.18-mm dia) inserted into radially-drilled holes. The thermocouples are bonded into the element with a high-temperature graphite coating,* designed to insure good thermal contact between the thermocouple and the body of the element. All of the graphite parts are fabricated from fine-grain ATJ** graphite with the grain oriented perpendicular to the heat flow. The body and face plate serve to one-dimensionalize the heat transfer patterns through the elements to simplify the analysis.

Placing the thermocouples at three depths relative to the exposed surface gives the temperature distribution in the element as a function of depth and time. Multiple elements provide redundancy in the data, and allow determination of spatial variations in the incident heat flux across the face of the

---

*Graphi-Bond 551 (TM), Aremco Products, Inc., Ossining, NY.

**(TM)Graphite Products Division, Union Carbide Corporation, Cleveland, OH.

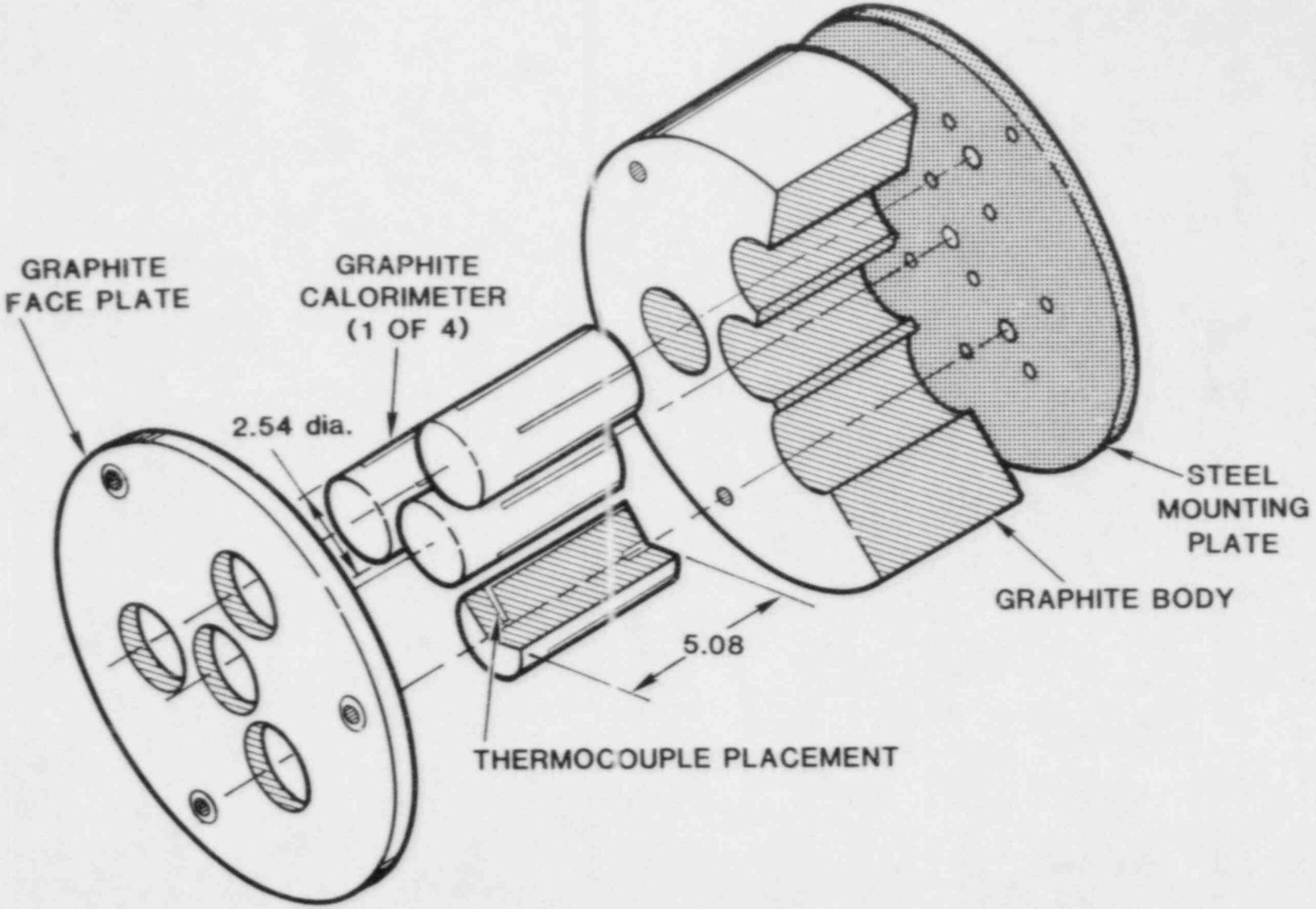

Figure 13. Slug-Type Heat Flux Calorimeter (Dimensions in cm)

calorimeter. Thermocouple response is recorded on a FM tape recorder with a frequency response of 40 khz. The data are subsequently stored on a floppy disk for analysis.

Analysis of the frequency response of the embeded sensor and an estimate of the error in the recorded temperature values is given in Appendix D.

The method of determining incident heat flux from temperature distribution within a body involves the solution of an inverse heat conduction problem to derive the boundary condition at the front surface of the element. Assuming the calorimeter body has a one-dimensional temperature distribution in the individual elements, the heat transfer can be represented as heat-flow in a semi-infinite slab. If the front surface is exposed to constant heat flux, then the temperature within the body at any location and time is given by:

(VI-24)

$$T(x,t) - T_o = \frac{\left(2Q\,\alpha(T)t/\pi\right)^{1/2}}{k(T)} \exp\left(\frac{-x^2}{4\alpha(T)t}\right) - \frac{Qx}{k(T)}\,\mathrm{erfc}\left(\frac{x}{2[\alpha(T)t]^{1/2}}\right)$$

where:

erf = Gaussian error function

erfc (z) = 1 - erf(z)

Q = incident heat flux

T_o = initial temperature of element

$\alpha(T)$ = thermal diffusivity = $k(T)/\rho c_p$

$k(T)$ = thermal conductivity

ρ = density

c_p = specific heat

x = location from exposed face

This equation can be solved if the heat flux is constant for the duration of the event and the functional relationship of the material properties with temperature is known. A solution is obtained numerically at discrete intervals in time because the incident heat flux from the impinging jet is not expected to be constant. The analysis uses an approach similar to that proposed by Beck (Ref. 22) by applying a least-squares method to damp the inherent instability of the numerical solution of the problem.

The quantity:

$$S^2 = \sum_{i=1}^{R} \sum_{j=1}^{N} \left(T_{i,j}^{obs} - T_{i,j}^{calc} \right)^2 \qquad \text{(VI-25)}$$

represents the error between the observed $\left(T_{i,j}^{obs}\right)$ and calculated $\left(T_{i,j}^{calc}\right)$ temperatures where N denotes the number of embedded thermocouples and R is the number of future temperatures employed to obtain a useful heat flux. The technique attempts to reduce the S^2 term in Equation (VI-25) with respect to the calculated heat flux.

The calculated temperatures are found using a modified Crank-Nicholson numerical routine that accounts for temperature-dependent thermophysical properties (Ref. 23). The procedure is applied piecewise over the data assuming the heat flux values to be constant over each specified time interval.

For the temperature range of interest (<1500°C), the data of Ref. 24 were fit to obtain an analytical expression for k(T) of the form:

$$k(T) = 0.07918 + 670.85/(T + 126.718) - 0.5199(T/100)^{-0.7877} \text{ (cal/sec-cm-K)} \qquad \text{(VI-26)}$$

Over the same range, the density and specific heat are given by:

$$\rho = 1.73 \text{ (g/cc)}$$

$$c_p = 0.3058 + 0.1589 \times 10^{-3}T - 0.03107 \times 10^{-6}T^2 - 0.1684 \times 10^{5}/T^2 \text{ (cal/g)} \qquad \text{(VI-27)}$$

Figure 14 gives the comparison between the calculated k(T) values versus those recommended in Ref. 24. The greatest scatter occurs in the temperature interval above 2000K (0.1 to 0.06 cal/cm-sec-K) where the observed values have been estimated or extrapolated from lower temperature data.

The number of future temperatures (R) to be used in Equation (VI-25) is determined by comparing the time associated with the maximum temperature in the element to the time when the maximum change in temperature occurs.

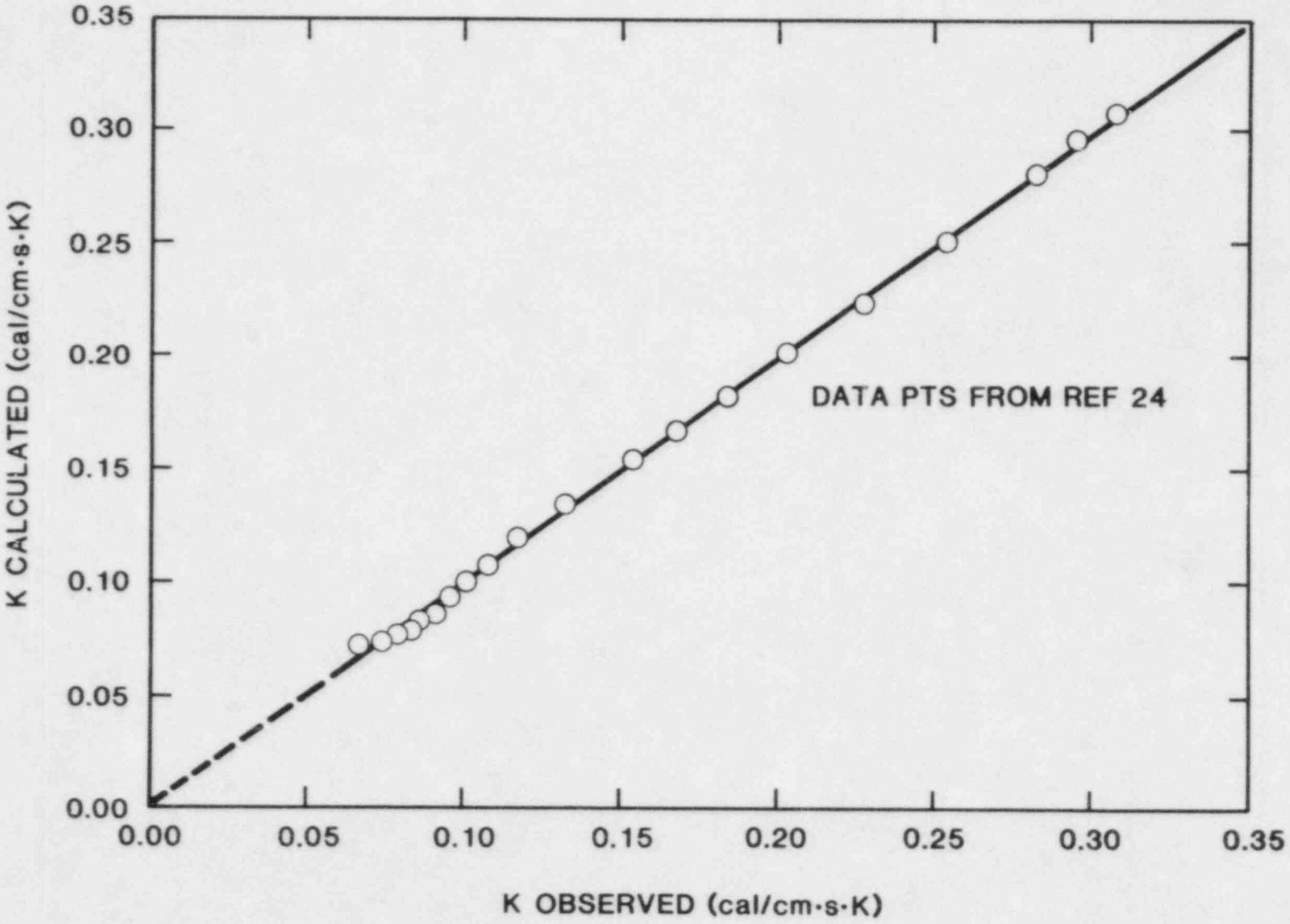

Figure 14. Thermal Conductivity of ATJ Graphite

Maximum Temperature:

$$t_1 = \frac{x^2}{2\alpha} \qquad \text{(VI-28)}$$

Maximum Change in Temperature:

$$t_2 = \frac{x^2}{2\alpha}(1 - 2/3) = \frac{t_1}{3} \qquad \text{(VI-29)}$$

Using an average value for α, the time intervals for the three thermocouple locations used in the calorimeter elements are listed below.

Depth	Maximum Temperature	Maximum Change
x_1 = 5 mm	t_1 = 14.6 ms	t_2 = 4.9 ms
x_2 = 10 mm	t_1 = 58.6	t_2 = 19.5
x_3 = 15 mm	t_1 = 131.8	t_2 = 4.4

Based on these results, the calorimeter elements respond to the imposed flux in times comparable to the discharge of the generator. Multidimensional effects such as the cooling from the sides of the block and the presence of a non-infinite dimension in the direction of propagation are therefore minimized. The results obtained from these data will be used to compare to those proposed in the ZPSS and to assess the attack on concrete by melt streams.

VI.2.2.8 Jet Aerosol Instrumentation

The SPIT free jet aerosol characterization tests provide an empirical basis for developing a model of aerosol generation by melt ejection in the accident scenario. The size distribution and mass concentration measurements of aerosols generated by a free jet or the debris exiting a scaled test article provide a basis to calculate the amount of aerosol material leaving the scale model's keyway (penetration). It may provide the means to back out the Stokes Number dependence of penetration to be applied to the accident case.

Doping the melt with appropriate fission product mocks and analyzing the sampled aerosol for those mocks provides a basis for assessing fission product aerosolization and transport to containment.

The SPIT aerosol characterization tests will be conducted in a closed chamber (approximately 43 m^3). The controlled volume permits the assumption of an instantaneous source of well-mixed aerosol. This assumption is facilitated by the less than 100-msec ejection time and the use of a mixing fan to evenly distribute the airborne material. Sample collection over various time intervals will provide distribution decay information. A summary of the devices to be used and the types of information obtained from each is given in Table 13.

Six Anderson Mark III cascade impactors will be used on each test. These cascade impactors give a particle mass distribution as a function of aerodynamic diameter. The pre-separator collects particles above approximately 10- micrometer aerodynamic diameter and will collect a relatively large mass of material to prevent overloading the subsequent impactor stages. Four impactors will be used in stationary positions sampling at 14 lit/min over sample times of 0-1, 1-3, 3-7 and 15-20 minutes.

Two additional impactors will be placed on a rotary device designed to sample isokinetically, by matching the impactor's airstream velocity to the velocity of the inlet as the impactor moves. The net effect is that large particles are obtained without having to significantly divert them from their natural paths (Ref. 25). These samples will be taken concurrently with the first two stationary impactor samples. Comparison of the stationary and rotary impactor samples, together with calculation of sampling efficiency for the stationary impactors from sampling theory, will provide information on sampling efficiency and the airborne size distribution. These instruments will directly provide size distributions, information on each of the modes, total concentration, and total mass aerosolized. The data will indirectly give the elemental distribution as a function of size when coupled with data from cascade cyclones.

Two Sierra cascade cyclones will be used on each test. These instruments consist of a series of cyclones to give an aerosol mass distribution as a function of aerodynamic diameter, as does the cascade impactor. The advantage of the cyclone is that larger amounts of material can be collected in each size class (each cyclone) for chemical analysis. One cascade cyclone will be operated from time 0-3 minutes. The other will be operated for a longer duration to assure that enough material is collected for the analysis. The first cyclone will provide the same information as the impactors. Size distribution information from the second cyclone will be distorted by the different decay times for concentration in each size class over the duration of the test. The elemental composition of each size class from the second cyclone coupled with the size distributions from the impactors and the other cyclone, will give the elemental composition distribution as a function of aerodynamic diameter.

TABLE 13
Aerosol Measurements and Instrumentation

Instrument	Measurement
Filter Samples	1,2,5
Photometer	1
Cascade Impactor	1,2,3,4,6
Cascade Cyclone	1,2,3,4,5,6
Deposition Samples	1,2,5

Measurements:

1. Total aerosol mass concentration
2. Total fraction of melt aerosolized
3. Size distribution of aerosol
4. Mass, mean size, and spread of each mode
5. Elemental composition of aerosol
6. Size-dependent elemental composition

Six Millipore 47-mm filter holders will be used on each test to collect total mass samples for elemental analysis. The sample times of 0-1/2, 1/2-1, 1-2, 2-3, 3-7, and 15-20 minutes give time resolution of mass concentration. They are taken concurrently with other samples to permit inter-instrument comparisons.

A photometer is a light penetration device that continuously monitors the intensity of a light beam across an aerosol sampling tube. It is strictly an empirical measurement device with *in-situ* calibration accomplished by filter collection of the measured aerosol. Six filters, operated concurrently with the six filter samples previously mentioned, are used for calibration. The device is placed in a large diameter (15 cm) duct utilizing a fan to draw in the airborne material. The duct serves to straighten the flow into the photometer so that the collected material is representative of the entire aerosol size distribution. The photometer is used principally to give a continuous aerosol concentration measurement as a function of time.

Deposition samplers placed on the chamber floor and walls are used to give total and time resolved deposition. The total deposition sample collection will be used to calculate total

aerosolized mass and elemental composition of aerosolized material. The results will be compared to the filter samples to assess sampling efficiency. The time-resolved deposition sampler exposes deposition surfaces at different times. Five surfaces are available with the sampling times: Ø-1/2, 1/2-1, 1-2, 2-3 minutes, and 3 minutes to test end. The time-resolved deposition samples enhance the concentration decay information and may be used for elemental analysis.

VI.2.2.9 Fission Product Mocks and Elemental Analysis

Doping the melt with fission product mocks (nonradioactive isotopes or chemically similar simulants) serves the following purposes:

1. Correlating the concentration of fission products in the aerosol will determine if fission product concentration is enhanced or retarded in the aerosol, and the particle sizes associated with the various fission products give an indication of the aerosol formation mechanisms.

2. The size and species distribution of the aerosol establishes a data base for empirical estimates and mechanistic modeling of fission product release from the melt ejection process. When used with keyway aerosol transport behavior, the distribution yields a radiological source term to the containment, as well as particle size information necessary to calculate residence time and transport.

The chemical analysis techniques used to measure fission product mocks can also be used to measure the size-dependent bulk composition of the aerosol. This is important in assessing the possible effects of unoxidized metal in the aerosol and the potential of the aerosol to act as a hydrogen ignition source.

Ideally, every fission product of interest would be represented in the melt and would be analyzed in the aerosol, however, the number of fission product mocks that can be included is limited. If the amount of non-reactive material in a thermite mix exceeds 1 w/o, it will tend to retard the reaction, slowing the reaction rate and limiting the maximum melt temperature. Detectability limits (see Table 16) dictate that minimum amounts of material are required as dopants. The small amount of aerosol material typically collected limits the available analytical techniques and, for some cases the number of elements that can be analyzed.

Selection of candidate fission products for simulation has been done by taking the total dose ranking at 1 and 1Ø hours from Ref. 26 and arbitrarily selecting the top 11 species from each

time frame. This procedure provides the field (see Table 14) from which to select the important fission products for this type of accident sequence.

TABLE 14

Importance Ranking of Fission Products
(Total Dose)

Rank	1 Hour	10 Hours
1	I	I
2	Np	Np
3	Te	Te
4	Tc	Mo
5	Mo	Tc
6	Sr	Ce
7	Ba	Nb
8	Cs	Ba
9	Y	Sr
10	La	Y or La
11	Ru	Ru

Table 15 gives the simulant selection for the fission products obtained from Table 14. Iodine and cesium are not included because they are volatilized early in the accident. Technetium (Tc) and Neptunium (Np) have no nonradioactive isotopes and are simulated by Manganese (Mn) and Cerium (Ce), respectively.

TABLE 15

Fission Product Simulants

Fission Product	Simulant
Np	Ce
Te	Te
Tc	Mn
Mo	Mo
Sr	Sr
Ba	Ba
Y	La or Y
La	La or Y
Ce	Ce
Nb	Nb
Ru	Ru

Identifying the fission products and their simulants allows determining the analytical techniques to be employed. The three techniques considered for the SPIT aerosol analysis are X-ray fluorescence (XRF), neutron activation (NA), and inductively-coupled atomic absorption (ICP). The first of these (XRF) is a nondestructive elemental analysis method which can be used for aerosols deposited on a filter or collected in bulk. Larger particles (>10 micrometer) in the distribution have potentially adverse affects on sensitivity and precision. For the filter sample, detection limits are on the order of 1 microgram per square centimeter of filter surface area. Lower mass concentration on the filter gives lower sensitivities.

Neutron activation is an additional nondestructive elemental analysis method. It is limited by low sensitivity to some elements of interest, such as Te and Al.

Inductively coupled plasma atomic absorption is a destructive elemental analysis method. Its primary limitation is that the sample material is consumed for each element analyzed. Typically, 100 mg of sample dissolved in 10 ml of solvent provides enough solution for analysis of 3 to 5 elements. There are also interference problems among elements such as Mn interfering with Zr. Table 16 lists the sensitivities and precision for each of the three analytical techniques, for the fission product simulatives being considered.

VI.2.3 Factorial Design Approach

The jet and aerosol characterization experiments are being performed to generate a data base for the development of analytical models. The models can then be used to predict jet and aerosol behavior for other system conditions and extrapolations to larger scale. The number of variables involved in the melt ejection and aerosol generation processes are large, complicating the correlation of input conditions to output results. The following paragraphs discuss the methods employed to develop a systematic approach to obtaining the required test outcomes.

The first step in developing a test matrix using a "statistical" approach is to identify the physical mechanisms that may affect the process. From these mechanisms, the experimental factors can be listed and their range of influence evaluated. Those variables that have a significant influence are carried forward in the test matrix, while the less important are held constant. The Phase I SPIT tests served to screen the physical mechanisms of the melt ejection process.

The SPIT test results determined that the dominant variables are pressure, gas solubility, melt temperature and the elapsed time from ejection to contact with a structure or water pool.

TABLE 16

Aerosol Analysis Techniques

Element	Method (Sample Size)					
	XRF[1] 100-mg Sample on 47-mm Filter		Neutron Activation 200-mg Sample		ICP 100-mg Sample Dissolved in 10-ml Solvent	
	Limit (ppm)	Precision (%)	Limit (ppm)	Precision[2] (%)	Limit (ppm)	Precision (%)
Ba		*	100	± 5	10	± 10
Sr	100	± 25	100	± 5	10	± 10
La		*	10	± 5	50	± 10
Y	100	± 25	†		10	± 10
Ce		*	1	± 5	50	± 10
Te		*	†		100	± 10
Mn		*	††		10	± 10
Ru	100	± 25	†		50	± 10
Mo	100	± 25	1	± 5	10[3]	± 10
Np		*	-		-	
Nb	100	± 25			10	± 10
Nd		*	6	± 5	100	
Zr	100	± 25	100	± 5	10	± 10
Fe		*	100	± 5	10[4]	± 10
Al		**	††		50	± 10
U	100	± 25			100	± 10

* Particle-size distribution may adversely affect sensitivity.

** Al not easily detected.

† Not sensitive to this element.

†† Involved procedure or Sanida Laboratories lacks facilities.

(1.) Particle size distribution affects sensitivity and precision. Precision of ± 25 relative percent is assumed.

(2.) Precision of ± 50% at detection limits.

(3.) May have problems with interference.

(4.) Interference from Mn, Ga, Rh, and Tm.

Melt mass can also be considered, but the limited capacity range of the SPIT apparatus cannot significantly alter the dependent variables (test outcomes). The 1/10th scale test matrix does provide an eight-fold increase in the mass. Table 17 identifies the range of each of these variables and the dependent variables that they influence.

TABLE 17
Independent and Dependent Test Variables

Independent Variable	Range	Influenced Dependent Variable (Responses)
Pressure	1.4 to 17.0 MPa	Jet velocity Incident heat flux
Gas Solubility	Low, High	Aerosol generation Jet disruption
Temperature	1500°C to 3000°C	Heat flux Aerosol generation
Jet height	0 to 4.1 m	Incident Heat Flux Jet configuration Aerosol generation

The pressure used for the experiments is easily controlled and measured. The principal difficulty is the possible increase in the initial value induced during the thermite burn. Gas solubility is related to the types of materials involved, the pressure, and to a lesser extent, temperature (see Section III.2). Establishing a value of gas solubility for each test is therefore complicated by the factors involved and by the uncertainty of their interrelationship. For the Phase II SPIT tests, two discrete values of gas solubility will be employed. Carbon dioxide represents a lower bound on the conditions expected for prototypic situations (i.e., steam and hydrogen over molten corium). Selecting nitrogen as the second gas provides an upper bound on the expected behavior.

The temperatures achieved during the thermite reactions appear to be a function of the constituents involved (particularly contaminants), pressure and the length of time the material resides in the vessel. The observations during the Phase I tests indicate that reducing the porosity by tamping the powder bed causes improved heat transfer and hence, a faster burn rate and less heat loss. Thus, the highest temperatures will be achieved for highly-tamped charges containing only the stoichiometric

material composition. Conversely, the melt temperature can be lowered by adding iron powder to the thermite charge to cause energy to be absorbed in heating the non-reacting materials.

The aerosol generation appears to be a function, in part, of the length of time the jet is exposed to ambient atmospheric conditions. The influence of this effect will be studied by experiments with widely varying distances from the exit aperature to the incident surface. This variation, combined with the range in jet velocity will provide a large spread in the total time of jet propagation.

The existence of four factors at two levels (low and high) allows a factorial strategy (Ref. 27) to be implemented. The range of each of the independent variables defines its response surface i.e. the geometric plane over which all other variables are held constant. The intersection of all the response surfaces represents the factor space, or all possible combinations of the factors variables. For three independent factors, the response volume is a cube, for four or more factors the shape is a "hyper-cube."

The intersections at the corners of the geometric volume represent design points or conditions where the factors are at their extremes. This design pattern is called a "two-level" factorial -- four factors at two levels each. The two-level factorial can determine the "main effect" of each factor, plus the "interactions" of the factors in combination. A full factorial test matrix would require 2^4 tests (16 total) to yield both main effects and interactions of the factors in combination.

Main effects are defined by considering the response of the system for two different values of factor X_1, while holding factors X_2, X_3, & X_4 constant. The estimate of the effect of X_1 at these two points can then be considered with other estimates obtained at other values of X_2, X_3, & X_4. The main effect of X_1 is then the average of all the estimates of the effects of X_1. In the same manner, the effect of X_2, X_3, and X_4 can be obtained.

The procedure above requires the use of all data to obtain an estimate of the main effect of a particular variable. This is called the "hidden replication" in a factorial experiment, because each factor effect and each interaction effect is based upon a difference between averages.

The improved precision of the factorial approach due to hidden replication can be estimated from the precision ratio (PR):

$$PR = \frac{\sigma_{FE}}{\sigma} = \frac{2}{(n)^{1/2}} \qquad \text{(VI-30)}$$

where:

σ_{FE} = standard deviation of a factor effect

σ = standard deviation of a single observation

n = total number of observations = $K2^P$

K - number of replicates

P - number of factors

This expression applies to all balanced two-level factorial experiments; both multiple replicates (K = 1,2,3..) and balanced fractional replicates (K = 1/2, 1/4, 1/8,...).

The PR depends only on the value of n, whether it is achieved through the number of factors (P) or the number of replicates. The PR required in a given experiment depends on three parameters that can be specified.

1. The parameter α specifies the confidence level $(1 - \alpha)$ that will be used for the t-statistic in testing the data for minimum significant factor effects.

2. The parameter Δ is the size of the factor effect it is desired to detect.

3. The parameter $(1 - \beta)$ is the desired probability of concluding that a factor has a significant effect when it has a true effect of size Δ.

The probability level $(1 - \alpha)$ establishes how close the average value is to the real value, within a certain confidence. The factor often used for this purpose is the "t-distribution" given in Table 18. The t-factor can be used to determine which factor effects are statistically significant.

For the experiment under consideration, K = 1 (no replication of data points) and P = 4 (pressure, gas solubility, temperature, jet height). Thus,

$$PR = \frac{2}{(16)^{1/2}} = \frac{2}{4} = 0.50$$

Performing one replication at any data point would improve the precision ratio markedly:

$$PR = \frac{2}{\left(2 \cdot 2^4\right)^{1/2}} = 0.35$$

TABLE 18

Probability Points if the t-Distribution

Double-Sided Test

df	P			
	.995	.99	.95	.90
1	127	63.7	12.7	6.31
2	14.1	9.92	4.30	2.92
3	7.45	5.84	3.18	2.35
4	5.60	4.60	2.78	2.13
5	4.77	4.03	2.57	2.01
6	4.32	3.71	2.45	1.94
7	4.03	3.50	2.36	1.89
8	3.83	3.36	2.36	1.89
9	3.69	3.25	2.26	1.83
10	3.58	3.17	2.23	1.81
11	3.50	3.11	2.20	1.80
12	3.43	3.05	2.18	1.78
13	3.37	3.01	2.16	1.77
14	3.33	2.98	2.14	1.76
15	3.29	2.95	2.13	1.75
16	3.25	2.92	2.12	1.75
17	3.22	2.90	2.11	1.74
18	3.20	2.88	2.10	1.73
19	3.17	2.86	2.09	1.73
20	3.15	2.85	2.09	1.72
21	3.14	2.83	2.08	1.72
22	3.12	2.82	2.07	1.72
23	3.10	2.81	2.07	1.71
24	3.09	2.80	2.06	1.71
25	3.08	2.79	2.06	1.71
26	3.07	2.78	2.06	1.71
27	3.06	2.77	2.05	1.70
28	3.05	2.76	2.05	1.70
29	3.04	2.76	2.05	1.70
30	3.03	2.75	2.04	1.70
40	2.97	2.70	2.02	1.68
60	2.91	2.66	2.00	1.67
120	2.86	2.62	1.98	1.66
∞	2.81	2.58	1.96	1.64

Defining the response of the system using only the extreme values of a particular variable does not indicate the behavior of the system between the two values. Obtaining the response for values intermediate to the two extremes allows estimating the deviation from linear (curvature) or obtaining a functional form for the response.

In order to estimate the curvature of each response indivi-didually would require an increase in the number of tests by 50 to 100 percent. An estimate of curvature can be made economically by performing tests at the middle points of all factors. The severity of curvature can then be estimated by the difference between the average of the design points (corner intersections) and the average of the center points. If the curvature is severe, linear model assumptions will only be accurate near the corners of the cube.

Factor effects can be calculated from response data and compared to the "minimum significant factor effect" to determine if the factor is important to the response. The curvature effect can be calculated and compared to the "minimum significant curvature effect" in a similar manner. The formulas for the minimum significant factor effect (MIN) and minimum significant curvature effect (MINC) are as follows:

$$MIN = T'(s)\ (2/mK)^{1/2} \qquad \text{(VI-31)}$$

$$MINC = T'(s)\ (1/mK + 1/C)^{1/2} \qquad \text{(VI-32)}$$

where:

T' = t-distribution statistic for the desired probability level and degree of freedom in the estimate

s = pooled standard deviation of a single response observation

m = 2^{p-1} where p is the number of degrees of freedom

K = number of replicates of each trial

C = number of center points

Comparing the individual factor effects to MIN establishes the relative importance of that factor. Typically, the probability $(1 - \beta) \geq 0.95$ is used. The largest factors (in absolute value) are the most important, relative to the response of the system. Similarly, if the computed curvature effect is larger than MINC, then at least one variable has a non-zero curvature associated with it.

More sophisticated analyses recognize the need to consider the linear, interaction and curvature effects with respect to all the independent variables. To estimate curvature, a full three-level factorial is required to provide orthogonal estimates. For four independent variables, a three-level factorial requires a minimum of 64 tests.

A fractional factorial test matrix can be used to reduce the total number of tests by performing eight tests with parameter vectors comprised of high and low values (corner points) and two replicants of a vector of intermediate values (center point). By reducing the number of tests by nearly a factor of two, the results will not be suitable to test for significant three-factor interactions. Some confusion among the interaction effects is characteristic of fractional factorial designs and is called "confounding." Confounded factor effect are termed "aliases" where the two interactions are defined identically. This method gives a main effects test program which permits the fitting of a response surface of the form:

$$R = \sum_{i=1}^{L} b_i x_i + b_o \qquad \text{(VI-33)}$$

where:

R = response such as jet velocity, aerosol size, etc.

x_i = i^{th} variable

b_i = the coefficient of the i^{th} variable

b_o = intercept

The choice of the fractional factorial matrix is dictated by a compromise between maximizing information and reducing the quantity of resources required for the matrix. Eighteen tests; all 16 corner points and two replicants of the center point, would be required to fit the interaction terms $x_i x_j$ where $i = j$. It should be noted that the additional 8 tests may be run, if deemed necessary.

Performing the tests and analyzing the results for the significant factor effects will aid in the development of a model to describe the jet and aerosol characteristics. The models can then be applied over the entire response volume to the accuracy identified in the error analysis of the data.

VI.3 Jet/Water Interaction Tests

A jet/water interaction is a creditable possibility during a reactor accident because of the presence of water in the reactor

cavity due to mitigation efforts or natural plant response. Only a limited amount of experimental data exist for this regime (Ref. 28), mostly for low temperature molten materials.

The SPIT jet/water interaction tests are directed towards providing the design and instrumentation requirements for experiments involving a high-pressure melt ejected into a scaled reactor cavity containing a water pool. The data will also be used to verify the ZPSS hypotheses concerning jet/water interactions.

The ZPSS analyses consider the range of water depth to be from a dry cavity to one that is fully filled with water. The extent of water in the cavity is dependent on the mitigation efforts and the natural plant response. To address all the possibilities in the SPIT matrix is beyond the scope of the program. The test strategy is simplified by assuming that the behavior of all jet/water interactions can be identified with one of two catagories: 1) fully-filled cavities or 2) cavities with a partial water pool. Quantitative differences are expected in the latter case depending on the depth of the pool, but the range should not affect the specifying of instrumentation.

VI.3.1 Water-Filled Cavity Analysis

The ZPSS analysis for a fully-water-filled cavity concludes that the water pool will have no effect on the debris dispersal process. This assumption is based on the theory that a large steam bubble will be created at the breach in the RPV that subsequently forces all of the water out of the cavity.

VI.3.1.1 ZPSS Analysis

The ZPSS estimates bubble growth by assuming that all the core material coming out of the pressure vessel is instantaneously quenched. The steam generated during the quenching process creates a bubble, with additional steam generation causing the pressure and hence the size of the bubble to increase. The rate of bubble growth as derived from the basic equations given in the ZPSS is:

$$\frac{dr_b}{dt} = \frac{3}{r_b}\left[\frac{RT}{2\pi r_b^2}\left(\dot{m}_q - \dot{m}_c\right) - P_b\left\{\frac{2}{3}\left(\frac{P_b - P_\infty}{P_\ell}\right)\right\}^{1/2}\right] \quad \text{(VI-34)}$$

where:

r_b = bubble radius

R = gas constant

T = absolute temperature

t = time

$\dot{m}_q$ = steam formation rate

$\dot{m}_c$ = condensation rate

P_b = pressure in the bubble (instantaneous)

P_∞ = atmospheric pressure

P_ℓ = pressure in the water away from the bubble

The steam formation and condensation rates are given by:

$$\dot{m}_q = A_f[2\rho_F(P_o - P_b)]^{1/2}\, c_F(T_F - T_{sat})/h_{fg} \qquad \text{(VI-35)}$$

$$\dot{m}_c = h_b(2\pi r_b^2)(T_{sat} - T_B)/h_{fg} \qquad \text{(VI-36)}$$

where:

A_F = area of breach in melt generator

ρ_F = density of melt

P_o = primary system pressure

c_F = melt specific heat

T_F = temperature of melt

T_{sat} = saturation temperature in the bubble

h_{fg} = heat of vaporization

h_b = heat transfer coefficient at the surface of the bubble

T_B = temperature of the water away from the bubble

The ZPSS derivation of the dr_b/dt expression from the same basic equations mistakenly omits the $(1/2\ r_b^2)$ factor in the first term in the equation.

The pressure in the water (P_ℓ) must be known to allow calculating the pressure in the bubble. For the geometry in the reactor, the expansion wave created by the steam bubble is transmitted to the walls of the cavity and reflected back at approximately twice the incident pressure. The velocity of the propagation is assumed to be given by the compressive wave velocity.

The interactions of the reflected wave patterns are complicated by the geometry of the cavity; waves returned by the side walls will be out-of-phase with those returned from the floor and instrumentation tunnel. Wave interactions are not considered in the ZPSS analysis, only the wave propagation in the instrument tunnel to the free surface at the containment floor. The calculated bubble and cavity pressure histories are given in Figure 15 (Ref. ZPSS Figure 3.2.9-6). The influence of the open instrument tunnel is predicted to cause the cavity pressure to decrease after the initial rise.

VI.3.1.2 SPIT Experiment Design

Two jet/water tests are proposed to satisfy the purposes stated above. The first test will use a large square box (Ø.6 m lateral dimension) of plexiglass to contain a water pool that is in contact with the melt generator. The transparent structure allows hi-speed framing cameras to be used to monitor the interaction of the jet and water and the growth of the steam bubble, if present. The important result will be to determine if the steam bubble growth occurs in the manner postulated by the ZPSS.

The walls of the box are not prototypic of the reactor in composition, dimensions or strength. Compressional waves emanating from the interaction zone will cause prompt failure of the box structure. The free water surface will allow expansion waves to be absorbed as movement of the water surface. These differences will cause the influence of water pressure on bubble growth to be less than in the reactor; the bubble growth rate should be greater in the experiment than in the accident.

To a first approximation, the response of the shock waves within a system can be evaluated by considering the mechanical impedances of the materials involved. The shock impedance of a material is given by (Ref. 29):

$$Z = \rho \mu_o$$

where:

Z = impedance
ρ = density
μ_o = longitudinal bulk sound speed

A compressional wave in water incident on an interface will cause a "partitioning" of the incident stress based upon the relative impedances of the materials. A simple approximation of the relative magnitudes can be found from the expressions:

$$P_T = P_o \frac{2Z_A}{Z_A + Z_B} \qquad \text{(VI-37)}$$

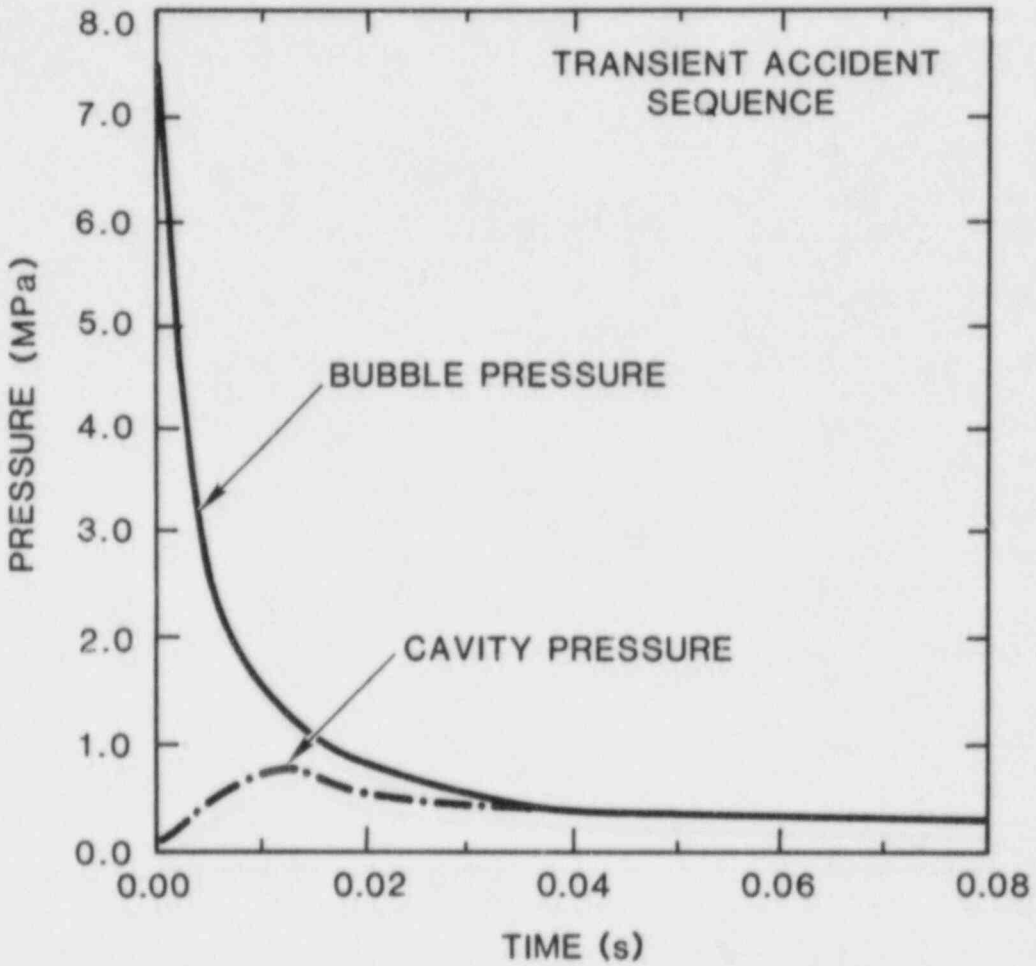

Figure 15. Bubble and Cavity Pressure Histories for a Water-Filled Cavity

$$P_r = P_o \frac{(Z_B - Z_A)}{(Z_B + Z_A)} \qquad \text{(VI-38)}$$

where:

P_o = incident stress level

P_T = transmitted stress into material B

P_r = reflected stress

Z_i = impedance of material i

In equation (VI-38) P_r represents the pressure that is reflected back into the incident material (water). If the source of P_o is continuous, then the reflected pressure P_r is superimposed on P_o from the interface to the point where P_r has propagated. Three limiting cases are considered to illustrate how these equations can be used to predict the wave interactions that will occur in the experiment and accident. The results of the calculations using equations (VI-37) and (VI-38) are given below:

	Interface Condition		
	Free Surface ($Z_B = \emptyset$)	Like Materials ($Z_A = Z_B$)	High Impedance ($Z_B >> Z_A$)
P_T	$2 P_o$	P_o	$\sim \emptyset$
P_r	$- P_o$	$\emptyset$	P_o

The free surface condition represents the situation where a gas exists above the water pool. The results show that an expansion (tensile) pulse will be reflected back into the water pool. A liquid can support a tensile wave only in absence of other disturbances that cause shear stresses to destroy the wavefront. Other wave interactions will undoubtably exist in both the experiment and accident, therefore causing the reflected pressure to rapidly return to zero. The transmitted stress ($2P_o$) will cause a portion of the water surface to expand away from the interface. The expansion will continue until P_o goes to zero, at which time the expanded portion of the pool will be "spalled off." This behavior supports the ZPSS assumption that the continually expanding steam bubble will cause all of the water pool to exit the cavity.

The second case involves similiar materials on both sides of the interface. This represents a hypothetical interface, reflection of the pressure is predicted to be zero and the transmitted pressure is unchanged.

The last example involves a second material that is of significantly higher impedance than the incident material. This situation is somewhat approximated by water in contact with the steel pressure vessel. For the limit $Z_B >> Z_A$, the transmitted pressure is essentially zero, but the reflected pressure is equal to and superimposed on the incident pressure. The direction of the reflected pulse is away from the interface and towards the source. This behavior will be maintained as long as the pressure source is constant. The pressure at the interface and in those regions encompassed by the propagation of P_r will be at roughly double the initial pressure.

Loads placed on the structure used to contain the water pools by the wave interactions are thus dependent upon basic material properties. Four materials are of interest in the experiments and accident: water, plexiglass, steel, and concrete. Standard material properties are obtained from References 30 and 31 and are given in Table 19.

TABLE 19

Material Properties for Impedance Calculations

Material	Density (kg/m^3)	Sound Speed (m/sec)	Impedance
Water	1000	1500	1.5×10^6
Plexiglass	1180	2680	3.2×10^6
Steel (Stainless)	7850	5960	46.8×10^6
Concrete	2340	4000	9.4×10^6

The ability of a plexiglass box to simulate the influence of a concrete cavity can be estimated by comparing the reflected pressure levels for both situations.

For Plexiglass:

$$P_r = P_o \frac{(3.2 - 1.5)}{(3.2 + 1.5)} = 0.36P_o$$

For Concrete:

$$P_r = P_o \frac{(9.4 - 1.5)}{(9.4 + 1.5)} = 0.72P_o$$

The calculation shows that the plexiglass will reflect approximately 50 percent less pressure from the interface than concrete. Because the pressure in the water is inversely related to the bubble growth rate (Eqn. VI-34), the plexiglass wall will cause the experiment to overpredict the bubble growth relative to the accident. Thus, if the bubble is not observed in the experiment, it will likely not exist in the accident.

Pressure pulses propagated to a free surface interface will not reflect pressure into the pool. This is contrasted to the reactor case, where the steel RPV will cause a pressure pulse to return to the pool. The reduction in the reflected pressure caused by the free surface in the experiment will also serve to overpredict the steam bubble growth. The presence or absence of trapped air pockets will affect the magnitude of the reflected wave.

Forces acting on the initial bubble generation suggest the geometry to be hemispheric. Compression waves emanating from the bubble will then be curvilinear as opposed to planar. Reflections from plane interfaces will be returned as curvilinear waves so that the return times of all portions of the wave front to the bubble are staggered. Likewise, waves incident at other than normal to a plane surface will reflect at a complementary angle and not back towards the source location. Plane or curved-wave fronts incident on curved surfaces such as the cavity wall will be reflected in a distorted manner. Thus, the interactions of the various pressure pulses within any geometry will become very complex.

The time interval in the experiment prior to wave interactions can be estimated by considering wave transit times. Considering the initial steam generation as a point source, the wave transit time is given by the dimensions of the box and the sonic water velocity:

$$t_1 = \frac{2\Delta x}{C} = \frac{2(30 \text{ cm})}{0.15 \text{ cm}/\mu\text{sec}} = 0.4 \text{ ms} \quad \text{(Horizontal)} \qquad \text{(VI-39)}$$

$$t_2 = \frac{2\Delta Y}{C} = \frac{2(110 \text{ cm})}{0.15 \text{ cm}/\mu\text{sec}} = 1.47 \text{ ms} \quad \text{(Vertical)}$$

The dimension in t_1 (30 cm) represents the horizontal distance from the center of the stream to the nearest edge of the box. The times, t_1 and t_2, represent the transit times of the initial compressional wave front. As the bubble expands, the distance will become less, depending on the relative growth of the bubble and the motion of the side walls. The calculated transit times are short compared to the discharge time of the generator, suggesting that the walls of the structure will very promptly distort and fail. The results can be compared to that expected during an accident where the transit time corresponds to the radius or depth of the reactor cavity.

$$t_1 = \frac{2(260 \text{ cm})}{0.15 \text{ cm}/\mu\text{sec}} = 3.5 \text{ ms} \qquad \text{(VI-40)}$$

$$t_2 = \frac{2(450 \text{ cm})}{0.15 \text{ cm}/\mu\text{sec}} = 6 \text{ ms}$$

Comparing the experimental and accident times indicates a scaling ratio in the range of 1 to 10 to 1 to 4.

The second purpose of the jet/water tests is to show the effect of the interaction in a scaled cavity. To do this, the wave interactions within the cavity must be properly scaled. In the reactor cavity, the compressional waves will propagate away from the boundary of the steam bubble until an interface is contacted, either the cavity walls, floor, RPV, or the free surface of the pool. The interactions of the waves are very complex due to the differences in the geometry of the bubble, cavity, floor, and vessel. Focusing of the reflected waves may cause instabilities in the bubble, inducing destructive fragmentation and dissipation of the bubble energy. The waves may also constructively interact at an interface boundary to concentrate pressure loadings on portions of the cavity.

The second jet/water interaction test is designed to cause wave interactions to occur in a prototypic manner. The test will determine the structural loads placed on the cavity by the hydraulic pressure in the water pool and the amount of expelled water. A 1:20 scaled-cavity geometry will be used to maintain the correct wave interaction transit times. Linear scaling can be used because the wave transit time is proportional to first power of the distance traveled. The cavity will be constructed of aluminum to simulate the impedence of concrete without being susceptable to rapid decomposition and gas generation. Using the relationship for reflected pressure (Eqn. VI-38) and material properties for aluminum from Ref. 30 gives:

$$P_r = P_o \frac{(17.3 - 1.5)}{(17.3 + 1.5)} = 0.84P_o$$

The strength of the reflected shock waves is approximately 10% higher than that predicted for concrete (0.72 P_o). The influence of the reflected wave on bubble growth may be slightly more detrimental compared to the reactor case.

The hydraulic loads on the cavity structure will be obtained by pressure transducers placed in the sidewall and floor of the cavity. The devices will measure the value of ($P_r + P_o$) at that location. Mapping the measured values for all locations should allow inferring the total load placed upon the structure.

VI.3.1.3 Predicted Loads

The magnitude of the hydraulic pressure-pulse can be estimated from a presumed thermal-to-mechanical conversion efficiency. Typical values of conversion efficiency for energetic interactions are estimated to be on the order of 1 percent or less (Ref. 32). Using 1 percent as a basis and assuming that all of the melt contributes to the mechanical energy in the form of pressure/volume work, yields the following:

Total adiabatic thermal energy = 10 kg x 3.6 MJ/kg = 36 MJ

Mechanical work = 0.01 x 36 MJ = .36 MJ

For an expansion process, the work is equal to the applied force (F) integrated over the distance of displacement (ds)

$$\text{Work} = \int F ds = \int (PdV + VdP) = \int VdP \qquad \text{(VI-41)}$$

where the PdV term is zero for a closed system in which the volume does not change. When the expanding pressure wave reaches the cavity wall or floor, the existence of the free surface at the end of the keyway is not yet a factor and the volume (V) can be approximated by the cylindrical cavity alone. Therefore:

$$\text{work} = V \int dP = V(P_2 - P_1) = V\Delta P$$

$$\Delta P = \frac{\text{Work}}{V} = \frac{0.36 \text{ mJ}}{2.13 \times 10^{-2} \text{ m}^3} = 1.69 \times 10^7 \frac{\text{Nt}}{\text{m}^2} = 16.9 \text{ MPa}$$

This value represents the incident pressure on the sidewall, P_o. The pressure the cavity must withstand is given by the sum of $P_r + P_o$.

$$P_{wall} = P_o + P_r = P_o(1 + 0.84) = 16.9(1.84) = 31.1 \text{ MPa}$$

This result establishes that the forces exerted through the water pool can be significant. The apparatus will be designed where possible to withstand loadings of this order to permit accurate pressure readings to be obtained.

VI.3.1.4 Instrumentation

For the two tests described above, the melt generator and aerosol instrumentation will be supplemented by high-speed motion picture cameras and multiple pressure transducers placed on the water container. For the plexiglass box, two pressure transducers will be used, one in the sidewall and the other in the base. Wall motion will cause these devices to register proportionally lower values than actually applied at the interface.

The aluminum scaled cavity will be monitored by a total of six pressure transducers. The devices will be placed in pairs in the cavity, tunnel and keyway regions. The individual pairs will be situated with one gauge mounted on a horizontal surface and the second on a vertical surface. Pairing the transducers provides redundancy in the data and an indicator of spatial resolution.

The motion picture cameras will be used to record the motion of the jet in the plexiglass water box and the resulting behavior of the water. Visual access to the aluminum cavity is not possible, but the cameras will follow the movement of water and melt from the exit of the keyway.

VI.3.2 Partially-Water-Filled Cavity Analysis

The interactions between the jet and water in partially filled reactor cavities differ from fully-filled in two significant ways:

1) Aerosol generation and hydrodynamic forces are active during the jet propagation through the ambient atmosphere

2) The free upper surface allows unconfined expansion of the pool

The first of these aspects is important in that the character of the jet may be altered depending on the distance between the RPV and pool surface. An unstable or divergent jet may be highly fragmented before reaching the surface causing it to be more susceptable to melt/water mixing. Better mixing may promote a vigorous vapor explosion.

The presence of a free pool surface allows only partial confinement of the pool expansion caused by steam generation.

Structural loading through the water is similiar to the filled cavity situation, but the loadings above the pool surface are significantly reduced. The lack of a coherent water structure throughout the cavity may prevent a complete purging of the water into the containment region.

The principal interest in the test results is the amount of water and melt displaced from the cavity region and the extent of aerosol generation. If the results are roughly equivalent to those observed for the fully-water filled cavity, it will be assumed that significant differences are not detectable. This outcome will then dictate that only one type of jet/water interaction test need be considered in the HIPS test matrix.

If detectable differences are observed between the two types of jet/water tests, then additional tests may be required to discern the source of the differences. It may be necessary to consider an additional experiment with a transparent water container to permit visualizing the type of interaction that occurs. The present state of knowledge of this interaction does not allow predicting what type of additional experiments may be required to understand the interactions in a partially-filled water cavity. The test matrix is developed to consider the possibility of one to three additional tests, although the specifics of the individual experiments are not yet developed.

VI.4 Scaled Cavity Tests

The SPIT scaled cavity test will be the first opportunity to study debris removal mechanisms in a realistic geometry, using prototypic materials. The test provides important information, together with the HIPS tests, to determine the scaling of the mechanisms to the reactor geometry. Quantative data on the aerosol source term and concrete decomposition processes will also be obtained.

VI.4.1 Apparatus Description

A schematic drawing of the concrete test article is given in Figure 16. The internal dimensions of the cavity represent a 1:20 linear scaling of the cavity, tunnel and keyway regions of the Zion plant. The concrete is the generic limestone-common sand composition given in Table 20 (from Ref. 6). Exact representation of the RPV and the instrumentation tube bundles are not included in the model. A flat steel plate holding a fusable plug is cast into the concrete at the scaled height of the RPV (22.5 cm) and is used as the bottom flange cover of the melt generator. The plate also prevents upward gas flow from the cavity, simulating the insulating shield around the Zion reactor.

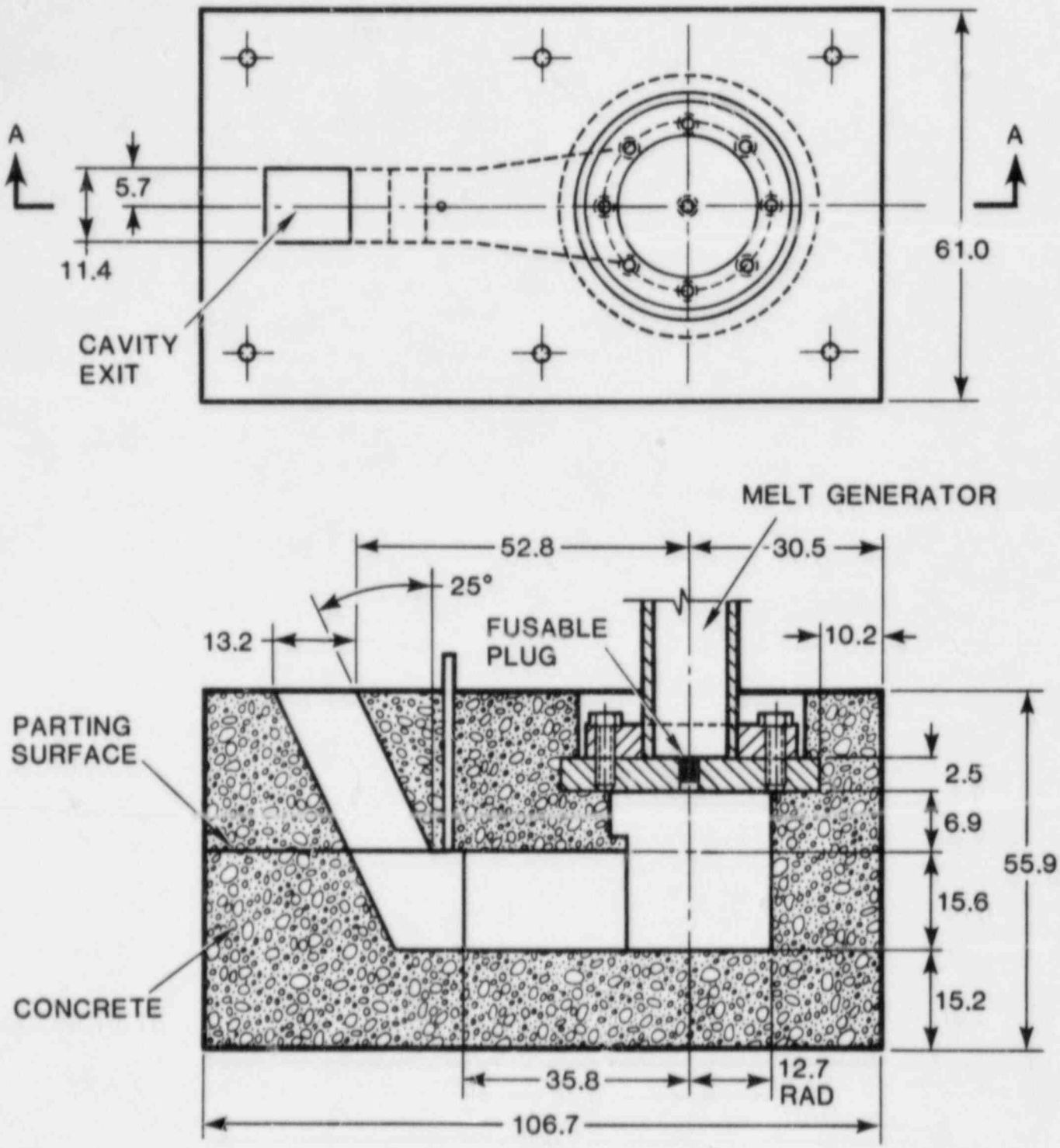

Figure 16. SPIT 1/20th Scale Cavity

TABLE 20

CHEMICAL COMPOSITIONS OF CONCRETE
(Weight Percent)

Oxide	Limestone/Common Sand Concrete	Basaltic Concrete
Fe_2O_3	1.44	6.25
Cr_2O_3	0.014	ND
Mn O	0.03	ND
TiO_2	0.18	1.05
K_2O	1.22	5.38
Na_2O	0.82	1.8
CaO	31.2	8.8
MgO	0.48	6.2
SiO_2	35.7	54.73
Al_2O_3	3.6	8.3
CO_2	22	1.5
H_2O	4.8	5.0
SO_2	<0.2	<0.2

ND = not determined

The parting surface located along the ceiling of the tunnel allows convenient access before and after the experiment. The two mating surfaces are gasketed so that a good pressure seal is obtained when the long through-bolts are secured. After the two halves are bolted together, the melt generator is lowered into place and secured to the embedded steel plate.

The experiment will be performed with the test fixture placed in a interaction chamber as depicted in Figure 17. The remaining assembly steps proceed in the same manner as described in Section VI.1.1.

VI.4.2 Information Sought from the Cavity Tests

In order to be useful in establishing scaling criteria, the results from the SPIT cavity tests must identify and measure the phenomena involved in the debris dispersal, aerosol generation, and concrete decomposition processes. Table 21 lists the informational requirements and the dependent phenomena of importance during the SPIT cavity tests. The term "debris" is used in the table to refer to the portion of the melt that is dispersed after the jet contacts the cavity or water pool.

TABLE 21

SPIT Cavity Tests Informational Requirements

Measurement	Phenomena
Pressure in Vessel	Gas solubility Jet velocity Gas velocity
Melt Temperature	Gas solubility Melt density Incident heat flux *Bubble growth
Gas Solubility	Aerosol source term Dynamic jet configuration
Jet Velocity	Dynamic pressure Mass flow rate Debris configuration Incident heat flux Aerosol source term *Penetration velocity

TABLE 21 (Cont.)

SPIT Cavity Tests Informational Requirements

Measurement	Phenomena
Jet Temperature	Incident heat flux Aerosol generation Debris configuration
Jet Configuration	Aerosol generation Incident heat flux Dynamic debris configuration *Water interaction *Fragmentation
Incident Heat Flux	Concrete erosion Gas generation *Water interaction
Concrete Erosion	Gas release/composition Aerosol generation Debris configuration
Dynamic Melt Configuration	Concrete decomposition Heat flux to surface, floors Removal mechanisms *Water interaction
Gas velocity	Debris dispersal Aerosol transport, generation *Water purge
Cavity Pressure	Debris dispersal *Hydrostatic pressure
Aerosol Composition, Size, Mass, Concentration	Fission product transport *Water pool scrubbing
Melt Disposition	Removal mechanisms Concrete erosion

* Applicable for experiments involving water pool.

Many of the informational needs arise from the discussion of debris dispersal and aerosol generation mechanisms given in Section IV.3 and IV.5. The following section discusses in more detail the instrumentation techniques that will be used.

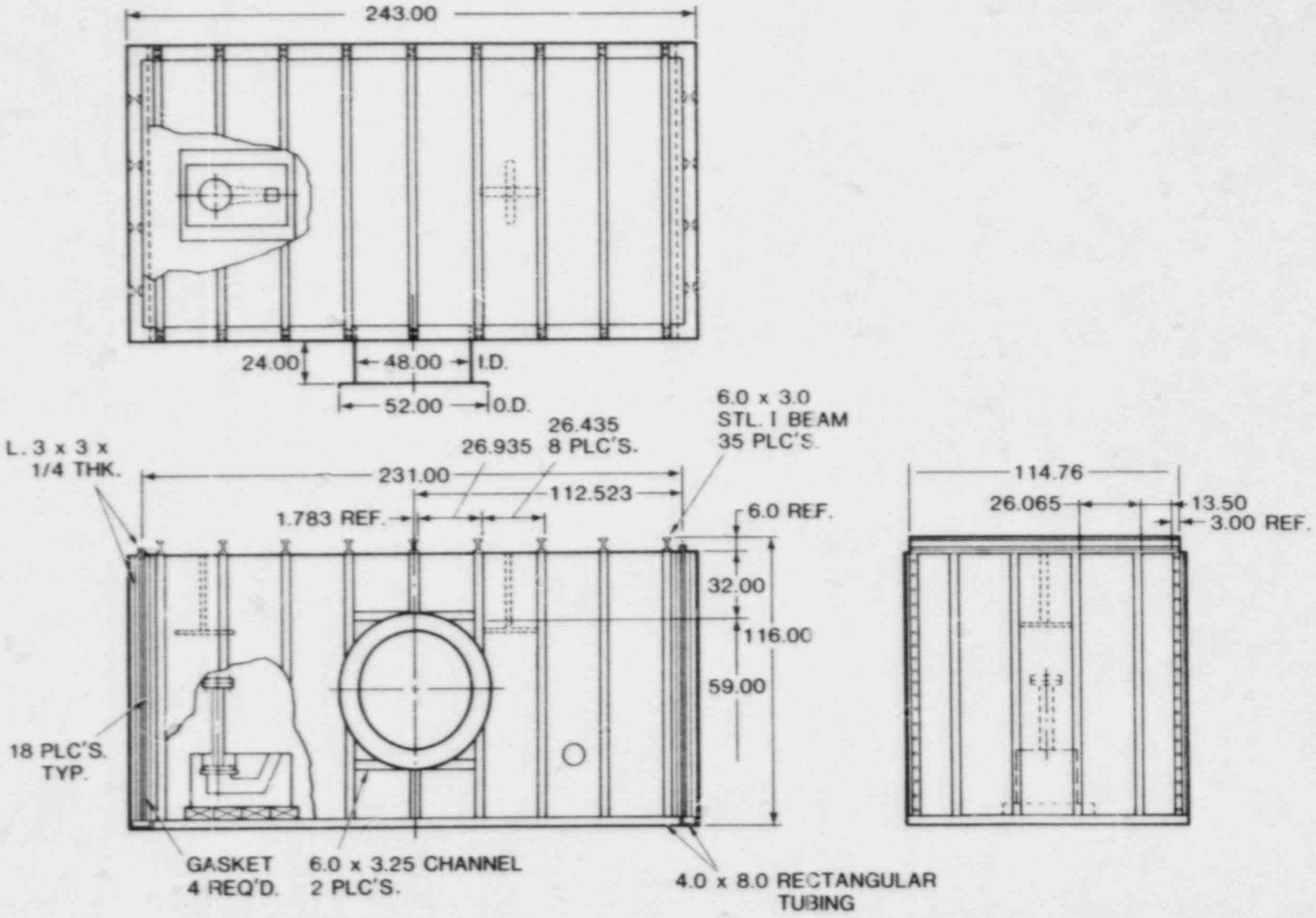

Figure 17. SPIT Apparatus Placed in the Interaction Chamber

VI.4.3 Cavity Instrumentation

Instrumentation for the SPIT cavity tests is more difficult to implement because of the lack of access within the test article and the need for unobtrusive devices. Consequently, most of the instrumentation used for the characterization testing is inappropriate for the cavity tests. The proposed instruments are given in Table 22 and are detailed in the paragraphs following.

TABLE 22

Instrumentation for the SPIT Cavity Tests

Measurement	Device	Comment
Melt Gen. Pressure	Pressure transducer	1- Expansion chamber 1- gas line
Melt Temperature	TC	Placed in crucible sidewall, inverse heat conduction analysis
Gas Solubility	none	Estimated
Jet Temperature	none	Estimated from characterization tests
Jet Velocity	none	" " " " "
Jet Configuration	none	Estimated from characterization results
Incident Heat Flux	none	" " " " "
Concrete Erosion	Embedded sensors	Also post-test observations
Debris position/ velocity	Embedded sensors	Optical detectors and electrical probes
Gas Pressure and Velocity	Pitot-static tube/Pressure gage	Placed in keyway and tunnel regions
Gas Temperature	Thermocouple	Shielded
Gas Composition	Sampling tube	Grab sample & post-test gas chromotography

TABLE 22 (Cont.)

Instrumentation for the
SPIT Cavity Tests

Measurement	Device	Comment
Cavity Aerosol	Sampling Tube	Filter sample
Debris Disposition	Catch pans	Located fixed distances from apparatus
	Framing Camera	Film record
	X-ray	At exit aperture
Chamber Aerosol	Impactor, filter, photometer, cyclone, deposition surfaces	Same as characterization test
Chamber Gas Composition	Time-phased grab samples	Post-test gas chromotography

The first seven measurements given in Table 22 (through Incident Heat Flux) are either done in the same manner or use the same data, as the jet characterization experiments.

VI.4.3.1 Concrete Erosion

Concrete erosion by the jet or debris pool is inferred from the output of thermocouples placed at various depths and locations in the concrete. Total erosion and erosion rate can be obtained using the time of failure and knowing the position of the thermocouple with respect to the initial melt interface.

Figure 18 illustrates a typical installation pattern for the embedded thermocouples placed in the SPIT scale model. The devices are commercial Type K sensors in ungrounded 1.6-mm-diameter stainless-steel sheaths. The size of the sheath has been selected for its relatively rugged construction. Sheaths of smaller diameter or bare thermocouples have been shown to be incapable of withstanding the pressures exerted during the concrete casting operations. The array is formed using 0.6 mm thick stainless steel shim stock between each unit and then spot welded. The arrays are positioned prior to the casting operation by thin (0.4 mm) steel wires stretched across the void formed by the concrete forms. This technique is estimated to give a positioning accuracy of $\pm$ 1 mm or better.

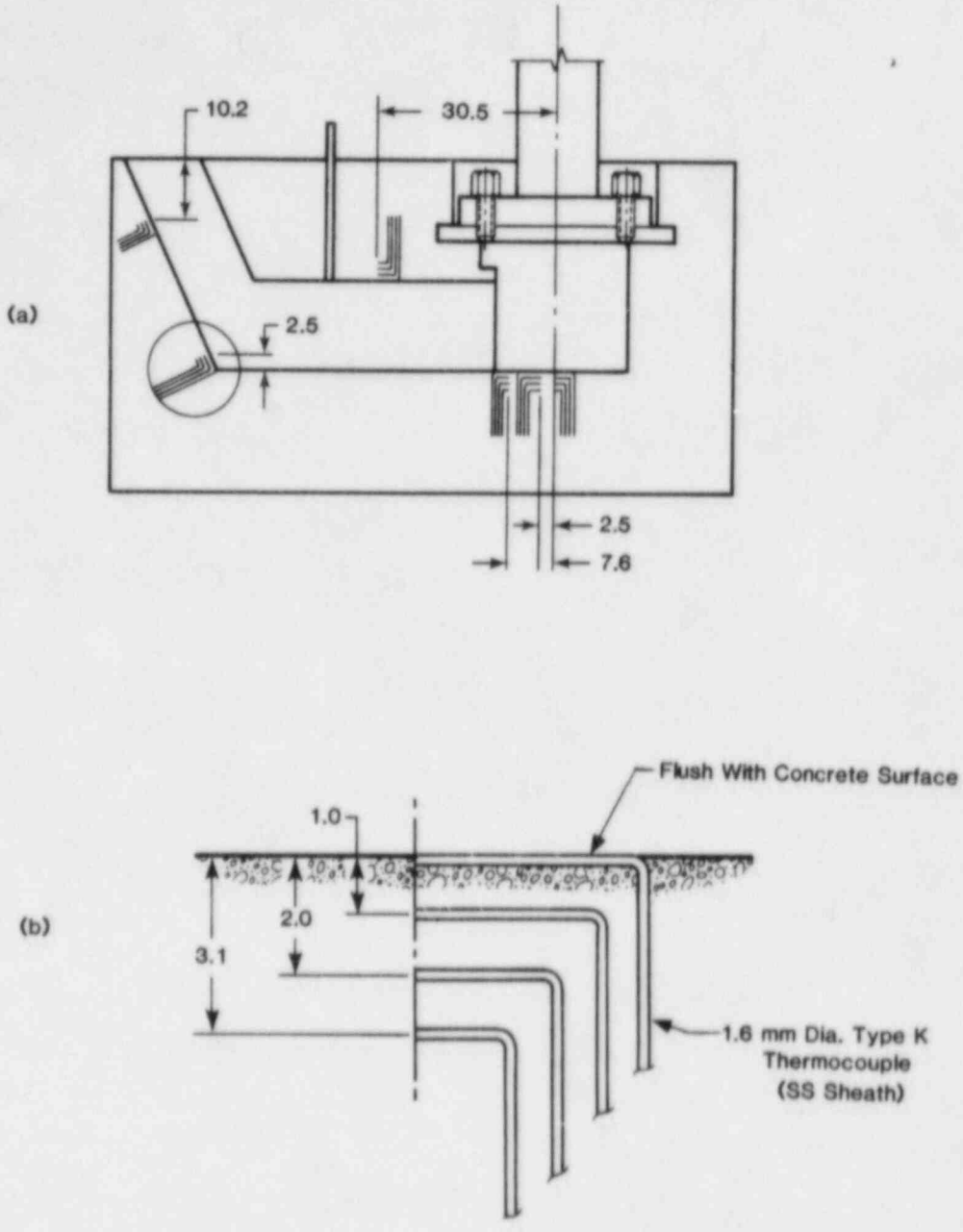

Figure 18. Embedded Thermocouple Details

(a) Thermocouple Arrays Placed in Concrete Cavity

(b) Details of the Array

(Dimensions in cm)

The arrays are placed in numerous locations on the floor and ceiling of the cavity. In all cases, the first sensor in the array is placed flush with the surface of the concrete so that an accurate reference for the other sensors is achieved. Each thermocouple is routed out of the concrete before terminating in a connector.

The ability of the thermocouple devices to measure erosion is dependent upon the accuracy of the device's placement, the response of the measuring system (including the sensor) and the ability of the experimenter to discriminate the onset of erratic behavior induced by the contact with the melt. The uncertainty in the position of the probes prior to casting is estimated to be ±1 mm, but the forces exerted by the concrete mixture combined with snifting of casting forms make the accuracy of the final position less certain. Experience with similar casting operations has shown that individual thermocouples can shift as much as 6 mm from their original position. The mean displacement appears to be on the order of 1 mm. The high-strength of the steel shim insures that the sensors in the array will not be separated, displacements are therefore restricted to bending of the sheath between the sensor tip and the steel strap. Inspection via X-rays is not practical because the resolution of the technique is inadequate to image specimens of small size.

Estimating the expected erosion rate allows quantifying the uncertainty associated with using thermocouples to monitor concrete attack. Reference 6 indicates that molten steel attacking limestone/common sand concrete has erosion rates varying from about 12 cm/hr to 20 cm/hr. These values probably represent a lower bound on the erosion caused by jet deposition, but are representative of that to be expected if the melt remains in the cavity in the form of a molten pool. For the purpose of this analysis, a mean value of 16 cm/hr is used.

Erosion rate determined by the failure of embedded thermocouples is given by:

Erosion rate ($\dot{D}$) = Distance between two sensors (D) ÷ the time interval between failures (TF)

The uncertainty in the erosion rate (ED) is then given by the expression:

$$E\dot{D} = \dot{D}\left[\frac{ED^2}{D^2} + \frac{ETF^2}{TF^2}\right]^{1/2} \qquad \text{(VI-42)}$$

The time interval between failures at 16 cm/hr corresponds to approximately 0.063 hour. For time periods on this order, the error in time measurement (accuracy of interval counter) is very small (0.01% of full scale) and is considered negligible compared

to the ability to discriminate the exact time the failure occurs. Typical values for the error in discriminating failure time are on the order of 10% if multiple sensors are employed. The error in the position of the sensor is estimated to average 1.5 mm. Using these values in equation (VI-42), the uncertainty in the erosion rate becomes:

$$\dot{E}\dot{D} = 16 \left[\left(\frac{0.15}{1} \right)^2 + (0.1)^2 \right]^{1/2} = 2.88 \ \frac{cm}{hr}$$

This value represents an error as given by:

$$\text{Error} = \frac{\dot{E}\dot{D}}{\dot{D}} = \frac{2.88}{16} = 18\%$$

The above analysis suggests that embedded thermocouples cannot give accurate erosion rate data unless significant improvement can be made in the detection of the failure time. The potentially high heat flux involved in the jet ejection could conceivably make the thermocouple failures more certain than the value used in the calculations. Conversely, the failures may occur so quickly that the response of the individual detector becomes the predominant source of error.

VI.4.3.2 Debris Position/Velocity

The ZPSS analysis proposes that the melt jet from the vessel stagnates at the cavity floor and forms a radially-expanding pool that travels down the instrument tunnel. If the velocity is sufficiently high, "splashout" of the melt will occur. Instrumentation capable of monitoring the initial movement of the melt would allow verifying the ZPSS hypothesis.

The sensor employed on the SPIT device relies on measuring the position of the melt with respect to time. The device, shown in Figure 19, consist of a thin strip of aluminum-oxide ceramic substrate imprinted with a network comprised of thick-film conductive and resistive paste. One side of the ceramic substrate has a continuous strip of conductor, while the other has a continuous resistor strip. At specified intervals, conductive "fingers" emanate from the resistive strip to locations opposite the continuous conductor. Bridging across the ceramic from the conductor strip to a "finger" will give a specified resistance when measured from the conductive tabs. An electrically insulating paint is used to cover the entire device except for small portions of the conductive tabs. The devices are placed into the concrete so that only the top portion of the continuous conductor and opposing fingers are exposed with the resistive strip buried in the concrete.

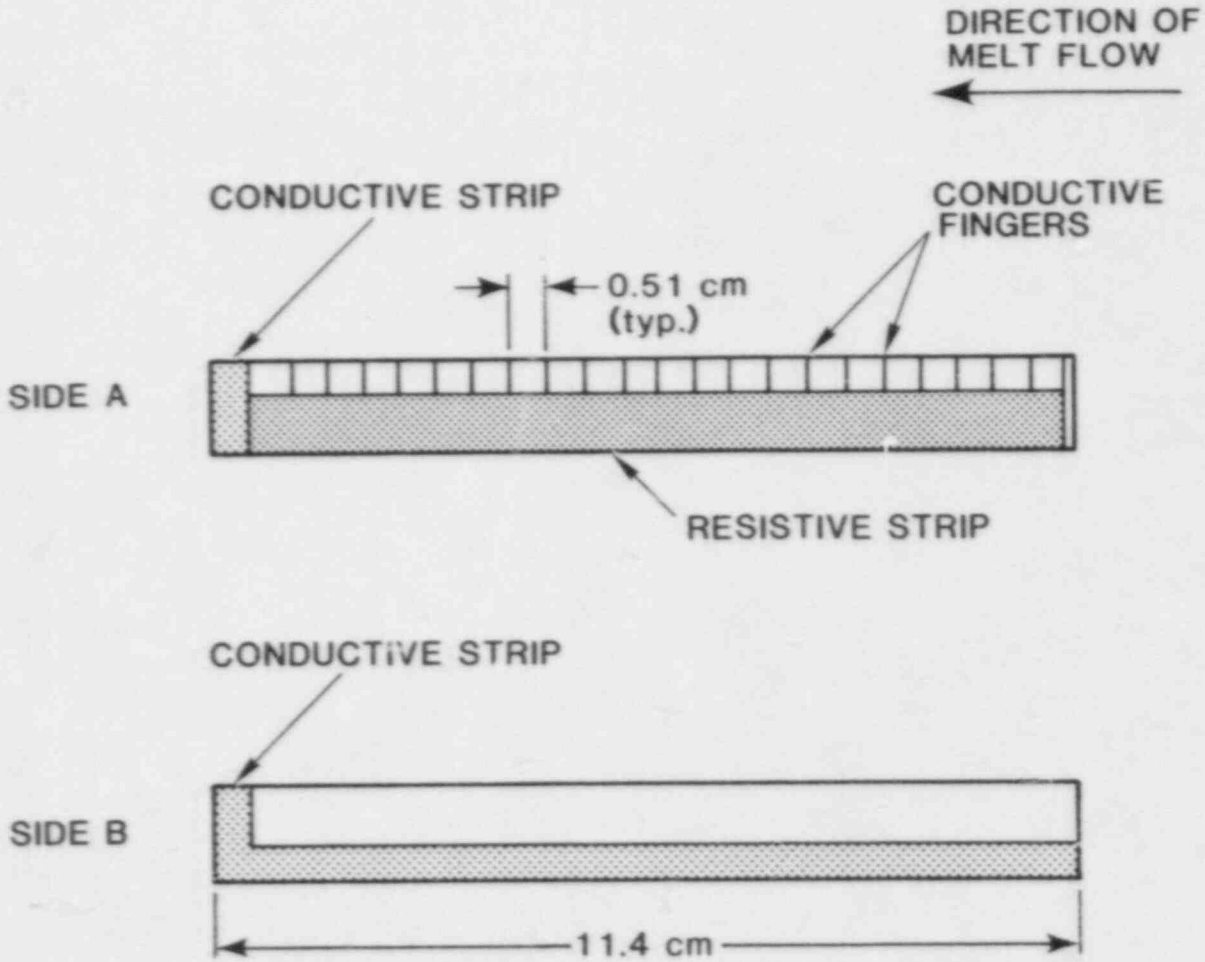

Figure 19. Melt Velocity Sensor

Each device is connected to a DC power supply so that a circuit of the type shown in Figure 20 is formed. The output of the circuit is given by the ratio of the resistance of the element to the shunt resistance:

$$E_{out} = E_{in} \left(\frac{R_s}{R_s + \sum_{i=j}^{n} R_i} \right) \qquad \text{(VI-43)}$$

where:

E_{out} = output voltage

E_{in} = power supply voltage

R_s = shunt resistance

R_i = resistance between element (i-1) and (i)

j = element number representing the position of melt front

n = total number of elements

When the melt front causes the last finger to be bridged, (i.e. j=n) then the output voltage is equal to the input. The quantity $\sum_{i=1}^{n} R_i$ is on the order of 2000 ohms so that choosing R_s = 100 ohms gives a system sensitivity of approximately 0.1 E_{in} per step. In this manner, multiple discrete voltage steps will be obtained as the melt passes over the device and shorts across each finger in turn. Plotting the data in terms of finger position as a function of closure time will yield velocity as the slope of the line fit to the individual points.

The error associated with measuring velocity in this manner is found by considering the accuracy of the position of each finger and the time measurement. This procedure is detailed in Appendix E. The analysis indicates that melt velocity determined by the ceramic sensors is reasonably accurate, on the order of 1.6%. This resultant is based on the assumption that the melt is well-behaved and that shorting of the elements will occur in a consistent manner. Observation of the free-jet experiments suggests that the melt will not behave as a fluid pool expanding along the cavity floor. Interaction between the hot melt jet and concrete is most likely to be highly energetic with liberation of significant quantities of aerosols and gases. These products are not conductive, so that deposition of the materials on the sensor ahead of the melt may insulate the elements. The expanding cloud of vapor observed with the melt stream may also move through the cavity to cause premature shorting of the elements

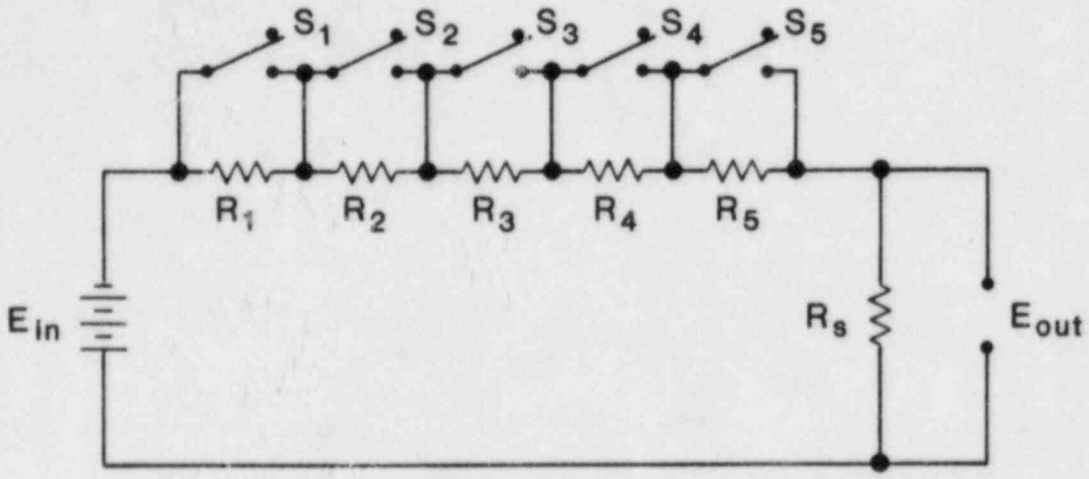

E_{in} - SOURCE VOLTAGE

E_{out} - OUTPUT VOLTAGE

S_i - SWITCH REPRESENTING MELT SHORTING ACROSS FINGER i TO CONDUCTIVE STRIP

R_i - RESISTANCE MEASURED FROM FINGER i TO CONDUCTIVE TAB

R_s - SHUNT RESISTOR

Figure 20. Electrical Circuit for Melt Velocity Sensor

prior to arrival of the melt. Likewise, melt sparged out of the pool may precede the melt front and cause erratic readings if deposited on the sensors.

The 1/20th scale cavity provides the opportunity to evaluate the melt velocity sensors under circumstances similar to that expected in the HIPS cavities. Failure of the devices or erratic results from the SPIT test may require other methods of making the measurement or modification to the existing technique.

VI.4.3.3 Gas Pressure and Velocity

The cavity shape determines the flow channel through which the blowdown gases from the melt generator must pass. The velocity and density of the gases give the dynamic pressure head term that is used in all of the hypothesized debris dispersal mechanisms. Thus, obtaining the gas velocity as a function of time is important in assessing the debris dispersal mechanisms.

The 1/20th scale cavity will be instrumented with a pitot static tube to determine the velocity of the gas stream. Applying conservation of energy to a section of the tunnel gives an equation for the velocity of the gas:

$$V_g = C_p \left(\frac{P_t - P_s}{\rho_g} \right)^{1/2} \qquad \text{(VI-44)}$$

where:

C_p = correction factor for the pitot tube to account for friction and turbulance

P_t = total or stagnation pressure

P_s = static pressure of gas

ρ_g = gas density

The quantity $(P_t - P_s)$ will be obtained directly by using a differential pressure gauge between the stagnation and static pressure ports. The differential pressure data is then used in Equation (VI-44) to give the local velocity at a particular location in the tunnel as a function of time. A highly turbulant flow is necessary to cause the velocity profile to be constant across the tunnel section. The velocity field is expected to be generated principally by the gases from the pressure vessel, plus gases released from the concrete. The resulting flow pattern is undoubtedly highly turbulent because of the high velocity of the ejected gas and the many obstructions provided by the cavity geometry.

The pilot-static device will be calibrated by performing a vessel blowdown with the melt generator in place. Using a calibrated flowmeter on the gas line to the generator will allow the mass or volumetric flowrate with time to be obtained. Knowing the density and the geometry of the apparatus will then give the velocity passing over the sensor location. The procedure will be done with nitrogen and carbon dioxide over a range of system pressures. The tests with carbon dioxide may illustrate the influence of gas condensation on the velocity measurements. These results will be useful in the modeling process concerned with the blowdown of steam from the reactor pressure vessel.

It is anticipated that the gas velocity will vary over a wide range as the system pressure drops from the initially high value to the final condition. The correspondingly wide range in the quantity $(P_t - P_s)$ will require a sensor with an equally broad response. Several pressure gauges in parallel may be employed to improve resolution of the data. The pilot-static tube also lends itself to measuring the static pressure alone. An absolute pressure gauge connected to the P_T port of the tube will yield the desired value. Thus, dynamic and static pressures can be obtained simultaneously using a single probe and properly selected pressure gauges.

VI.4.3.4 Gas Temperature in the Tunnel

Measuring the temperature of the gas flow in the tunnel is complicated by the radiative heat transfer from the molten pool and cavity surfaces. To minimize the effect, the thermocouple will be placed in a shield arrangement that allows the gas to flow freely over the element. The shields will be designed to prevent stagnation of the flow so that the proper convective heat transfer conditions are maintained. A multiple-shield, high-velocity thermocouple of a type similar to that shown in Figure 21 will be used.

The response of the probe to sudden changes in temperature can be approximated by the relationship (Ref. 33):

$$T_p = T_g = (T_g - T_o)\ e^{-t/\tau} \qquad \text{(VI-45)}$$

where:

T_p = temperature of the probe

T_g = gas temperature

T_o = initial temperature of the probe

t = time

τ = time constant of probe

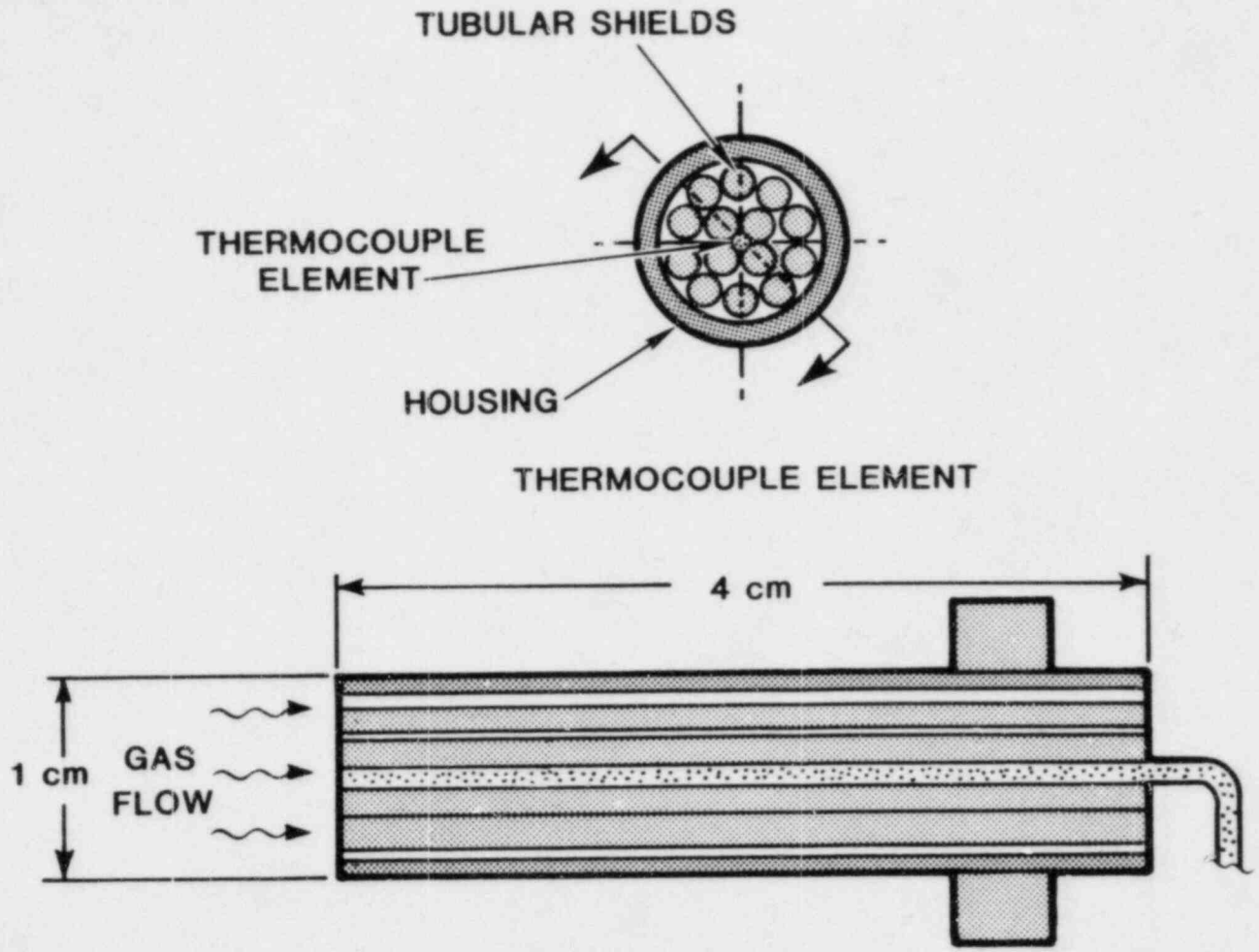

Figure 21. Multiple-Shield, High-Velocity Thermocouple Assembly

Reference 34 is used to estimate the time constant for this type of configuration. For velocities on the order of 2 m/sec and a thermocouple element approximately 1.6 mm in diameter, the time constant is on the order of 20 msec. The device should then be capable of resolving step changes in temperature with rise-time as fast as 50 msec. Therefore, the thermocouple configuration is expected to be only marginally adequate to respond to a step change in temperature occuring during the discharge interval. The device will not be capable of resolving rapid variations in the gas temperature that occur in times shorter than 50 msec.

VI.4.3.5 Gas Composition

The composition of the gas flowing through the tunnel is necessary for the equations governing the melt removal process. "Grab" samples are typically used to obtain composition via gas chromatography. The composition is expected to derive principally from the gas used to charge the melt generator, plus the gases released from the thermal decomposition of the concrete. Gasses released from the concrete are important because they will aid in the development of models to predict the type and amount of noncondensable gas that can be expected in a reactor accident.

The traditional method of gas sampling is to draw the composition into a pre-evacuated chamber that is subsequently sealed by remotely-operated values. The time required to equilibrate the pressure in the sample volume with the experimental apparatus is dependent upon the flow through the interconnecting piping. The flow can be estimated using the Colebrook equation to obtain the friction in the pipe (Ref. 35):

$$(f)^{1/2} = 2 \log_{10}\left(\frac{\frac{\varepsilon}{D}}{3.7} + \frac{2.51}{R_e\sqrt{f}}\right) \qquad \text{(VI-46)}$$

where:

f = friction factor

$\frac{\varepsilon}{D}$ = relative pipe roughness

D = pipe diameter

R_e = Reynolds number

Equation (VI-46) can be solved by evaluating the mass velocity term G between the reservoir (1) and sample volume (2) connected by a length of pipe (L):

$$G = \rho V = \left\{ \frac{\rho_1 P_1 \left[1 - \left(\frac{P_2}{P_1} \right)^2 \right]}{2 \log_e \left(\frac{P_1}{P_2} \right) + \frac{fL}{D}} \right\}^{1/2} \qquad \text{(VI-47)}$$

where V is the velocity of the gas in the tube. The mass velocity can also be given in the form of the Reynolds number:

$$G = \frac{R\mu}{D} \qquad \text{(VI-48)}$$

where μ is the dynamic viscosity of the gas.

If $P_1 >> P_2$, then the first term in the denominator of Equation (VI-47) can be neglected and equating Equations (VI-47) and (VI-48) gives:

$$R_e \sqrt{f} = \left\{ \frac{D^3 \rho_1 P_1}{\mu 2_L} \left[1 - \left(\frac{P_2}{P_1} \right)^2 \right] \right\}^{1/2} \qquad \text{(VI-49)}$$

The mass velocity can be used to determine the mass flow rate ($\dot{m}$) through the pipe.

$$\dot{m} = \frac{\pi G D^2}{4} \qquad \text{(VI-50)}$$

Solving Equations (VI-46) through (VI-50) simultaneously will give the mass flow into the sample chamber. The interval required for the sample is then obtained by determining the point in time at which the pressure in the sample container is equal to the pressure in the tunnel. For the nominal conditions of the test, the sampling time required is on the order of 10 seconds, or roughly the same time frame as the blowdown of the system. The response time of this technique will not be adequate to resolve details of gas release process. It may; however, be capable of resolving the melt/concrete interactions that occur over a longer period, depending on the extent of debris material removed from the cavity region.

A continuous sampling technique provides a alternative approach to filling gas bottles. This method also uses a sample tube but the pressure differential would be provided by a vacuum pump drawing on a manifold of parallel sample containers. Valves

placed on the inlet and outlet of each bottle are connected to a time sequencer to control valve activation. All of the containers are initially open to allow gas to pass through unrestricted. At preselected times during and after the ejection sequence, the valves on the individual containers are closed to trap the gas within. Sequential valve closures allow the variation in composition with time to be assessed. The time delay of the sampling tube is a factor but it should cause the same time shift to occur in each of the samples.

VI.4.3.6 Debris Deposition

Debris deposition or displacement refers to the amount of material that is removed from the scaled cavity during the experiment. The two questions that must be addressed are: 1) the quantity and size distribution of material ejected out of the cavity and 2) the time-frame of melt dispersal relative to jet ejection, water pool contact, or gas blowdown.

The first question can be answered by simply measuring the amount of material that is outside the model at the end of the experiment. This amount is then compared to the original mass of the thermite constituients and any residual material remaining in the melt generator. The collected material will include displaced melt, aerosols, and possibly concrete particles that have settled onto the chamber floor. Mechanical screens can be used to separate the smaller aerosolized material, giving a size distribution of the displaced melt. Chemical analyses will be done on the residue.

The ejected melt stream is typically accompanied by a luminous cloud of vaporized melt that darkens as it cools and condenses. This cloud will undoubtably also be ejected from the cavity, along with the molten debris. Conventional photographic techniques will not penetrate the cloud to show the debris dispersal process. X-ray detection is capable of resolving the position of the dense melt within the luminous cloud. The x-ray record should show good contrast between the dense (melt) and the other, less-dense materials. Time-resolved estimates of the amount of melt material ejected will be uncertain because the image is a two-dimensional view of a three-dimensional object.

Post-test inspection of the test article will also indicate the extent of material removed from the cavity. Melt material remaining in the cavity will probably be tightly adhered to the concrete surface. If the quantity remaining appears to be large, then obtaining the mass of the entire test article before and after the experiment will be used to estimate the mass of debris remaining in the cavity. This method does not account for the mass lost by concrete decomposition, which is expected to be small in comparison.

VII. HIPS Experimental Program

The main objective of the HIPS tests is to provide experimental confirmation of the debris removal mechanisms postulated in the ZPSS. The results will also be used to describe the aerosol generation mechanisms and fission product source term during melt ejection and vessel blowdown. The data will be used in developing scaling criteria to full-size reactor geometries and a model for predicting the ex-vessel portion of the accident process.

The HIPS test matrix has been developed with the assumption that the results from the SPIT aerosol and jet characterization tests can be scaled to larger geometries. Similiar tests in the larger, HIPS geometry will be limited to the number necessary to confirm the scaling hypothesis. The program also assumes that the SPIT 1/20th scale cavity experiment will demonstrate the type and location of the interactions, and the instrumentation needed to diagnose the resulting behavior.

The following sections cover the description of the experimental apparatus and instrumentation, the information sought from the tests and the test strategy employed.

VII.1 Experimental Apparatus

The HIPS apparatus consists of a melt generator, concrete test article, and the same interaction chamber as that used in the SPIT program. The test article represents a 1/10th linear scaling of the Zion reactor cavity.

VII.1.1 Melt Generator

The HIPS melt generator incorporates improvements based on the experience gained during the SPIT program. The dimensions of the HIPS generator are significantly larger, with available volume for gas expansion representing an 18-fold increase over the SPIT equipment. A second advantage of the relatively larger diameter is that the distance between the melt crucible and vessel wall is increased. The increased thickness of refractory powder provides greater protection to the vessel integrity.

A schematic drawing of the pressure vessel to be used as the melt generator is shown in Figure 22. The wall is made of 16 inch (41 cm) OD, Schedule 60, mild-steel pipe casing (1.6 cm wall thickness) with bolted flanges welded to each end. The flange covers are sealed with flat, reinforced gaskets. The internal length of the device (1.34 m) gives an approximate volume of 0.146 m^3. The assembled apparatus has a rated maximum allowable working pressure of 2500 psia (17 MPa), sufficient to cover the expected range for the HIPS test matrix.

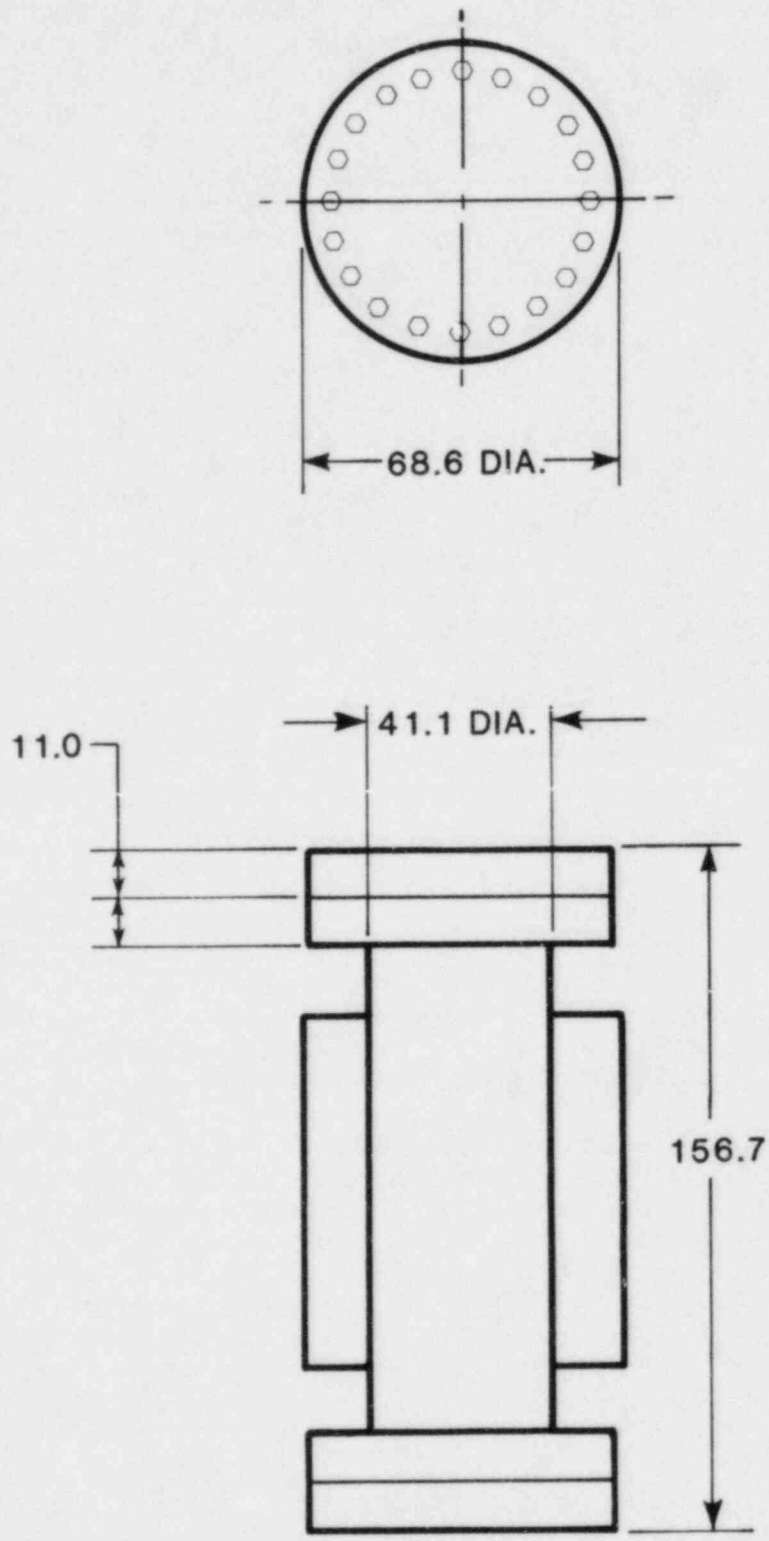

Figure 22. Schematic of HIPS Melt Generator
(Dimensions in cm)

Unlike the heavy pipe section used in the SPIT apparatus, the HIPS melt generator will use a thin-wall melt crucible. As shown in Figure 23, the crucible is constructed of inner and outer shells separated by a 2 cm thick layer of refractory wet ram material, designed to sinter when exposed to a high surface heat flux. The ramming material will form the prime barrier to the molten thermite, and it is anticipated that the heat flux from the melt will cause sintering to a depth of several centimeters. The sintered shell will then be used as the crucible on subsequent tests with the apparatus.

Graphite plate, 12 mm thick, is used to cap the upper and lower ends of the melt crucible. The upper plate has a central 50 cm diameter to allow gas passage between the crucible and expansion volume above. The lower plate is machined to expose the brass fusable melt plug in the bottom flange cover. The bottom flange cover has been modified to accept a small-diameter "insert" plate that is replaced for each test. The insert permits the size of the exit aperature to be selected and minimizes damage to the flange cover. The insert is sealed to the flange cover by an O-ring and retaining bolts.

Assembly of the melt generator process is similar to the pattern used for the SPIT device. First, the size of the exit aperature is determined and the insert machined to accept a melt plug of corresponding dimension. The insert is then placed in the lower flange cover and the flange and insert assembly placed into the recepticle located in the concrete test article. The melt generator is lowered onto the lower flange plate and securely bolted into position. The lower graphite plate is then placed in position so that the melt plug is exposed. The crucible is lowered onto the graphite plate and held in position. After extraneous material is removed from inside the shell, the thermite powder is placed into the crucible.

The thermite is lightly tamped during placement to reduce the porosity and overall volume. The ignitor is placed into the thermite to a depth of nominally 2 cm and extension wires are brought out through the upper graphite cover. The leads are then crimped to the electrical feedthroughs in the vessel side wall and the cover is bolted in place. Attaching the gas feed line and instrumentation leads completes the assembly process.

VII.1.2 Test Article

The internal dimensions of the HIPS test article are based on a 1:10 linear scaling of the Zion cavity, tunnel, and keyway regions. Figure 24 shows details and dimensions of the HIPS test article. The external dimensions have been selected to allow the structure to withstand the strains imposed during melt ejection and vessel blowdown.

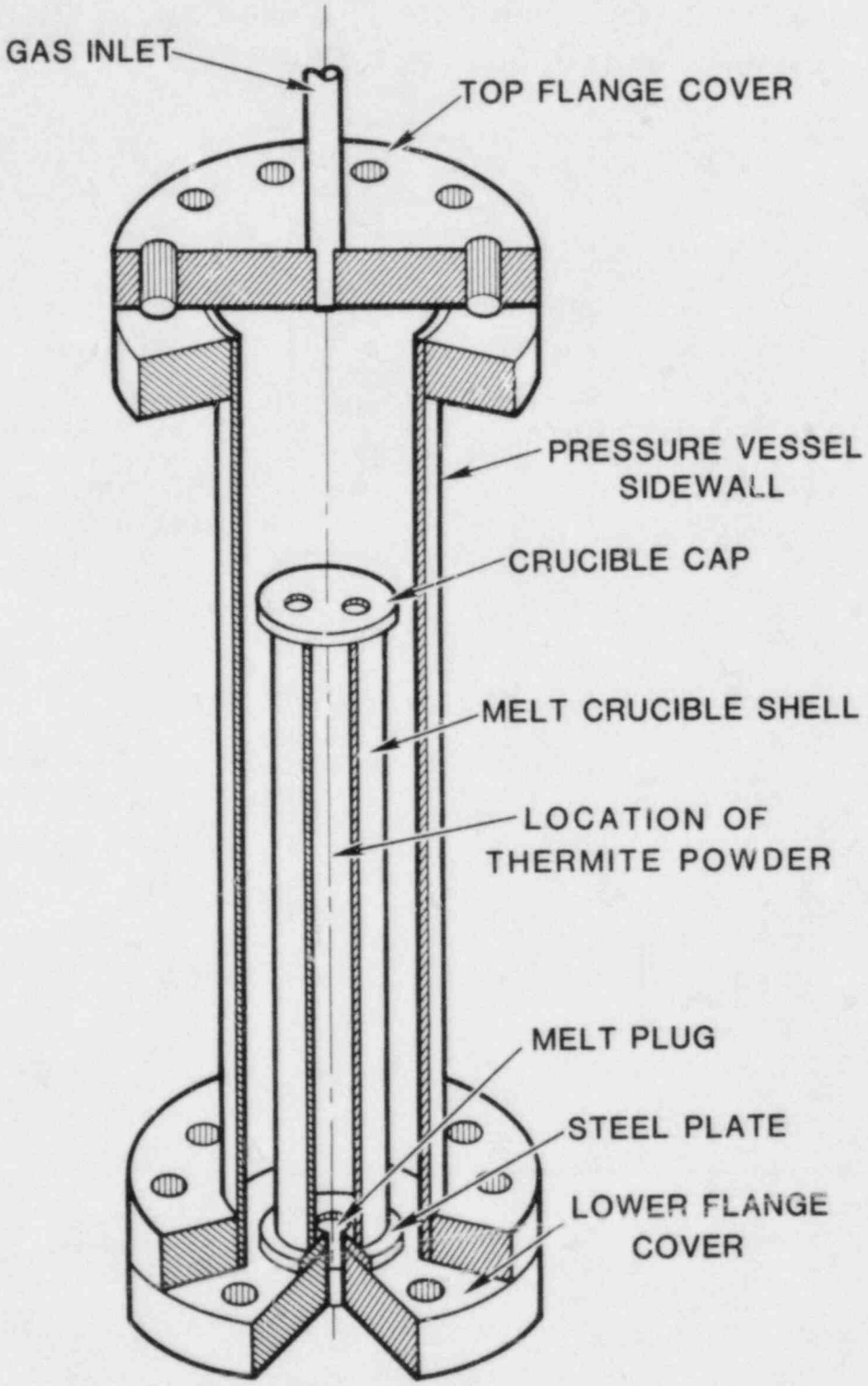

Figure 23. HIPS Melt Generator Assembly

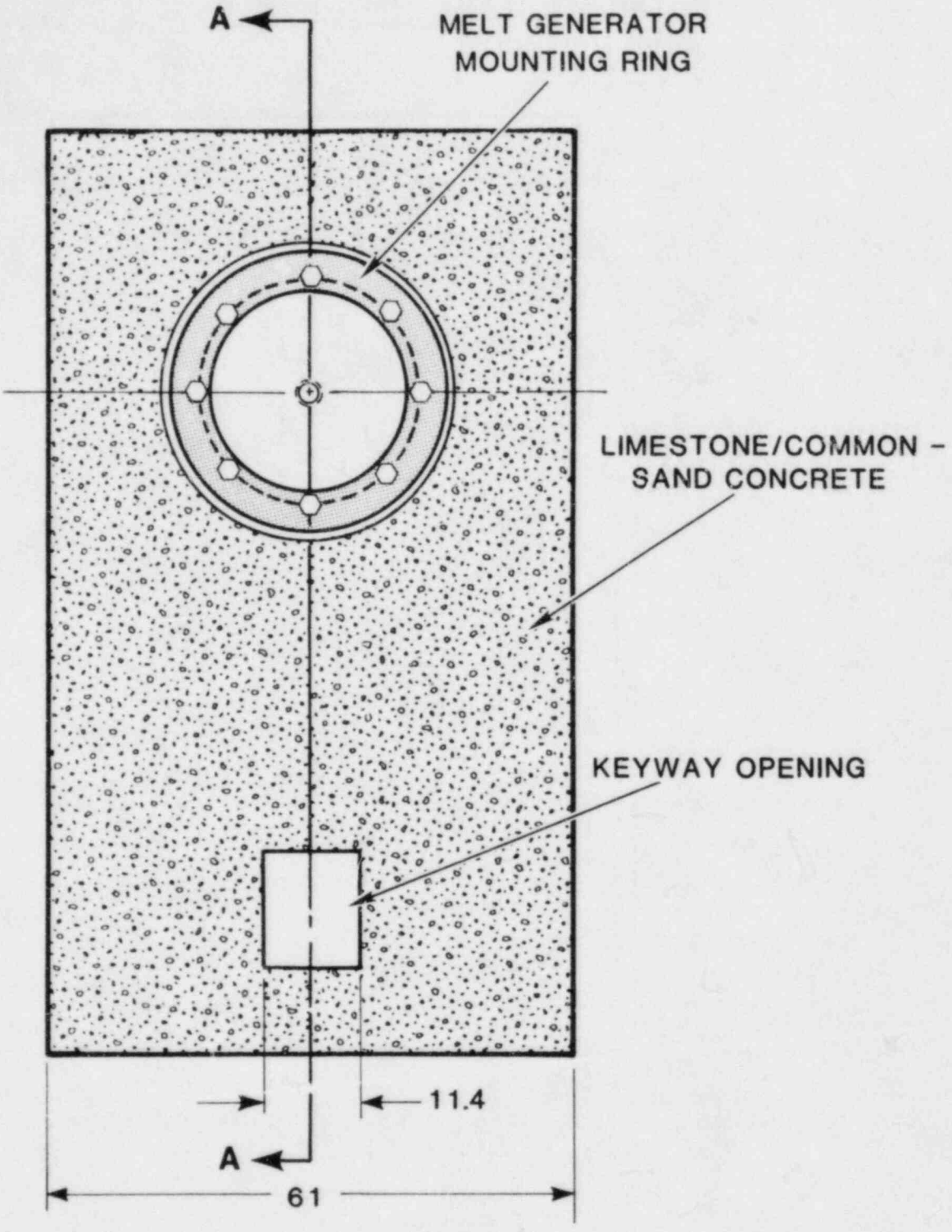

Figure 24a. Top View of HIPS Test Article (Dimensions in cm)

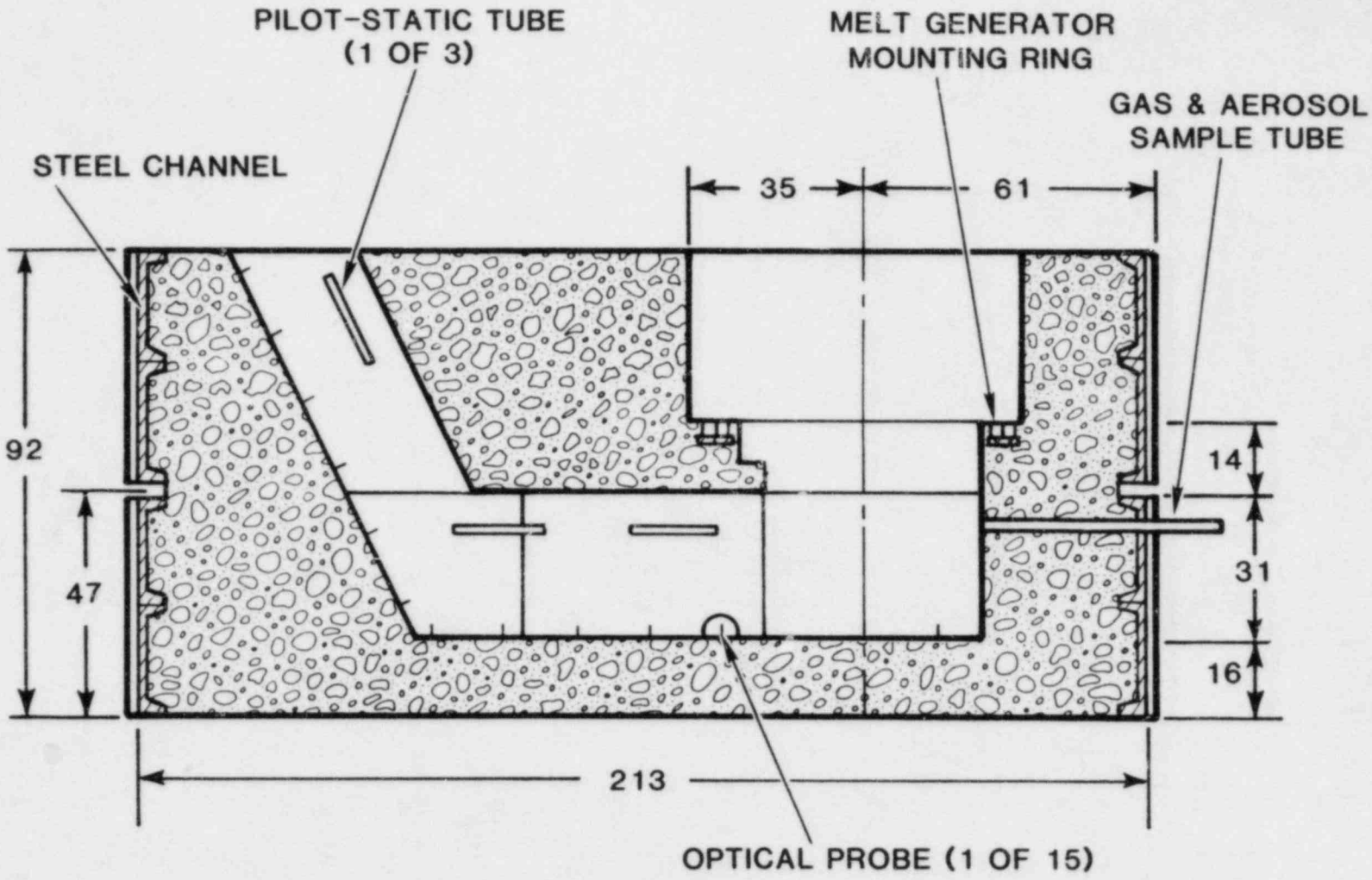

Figure 24b. Cross – Section of HIPS Cavity Region (Dimensions in cm)

The test article is formed in two sections with the parting line located along the upper tunnel surface. Each section is constructed using large steel channel members welded together to form the outer periphery. The steel provides added strength to the concrete structure and a convenient means for handling the apparatus. The concrete is generic limestone/common-sand (see Table 20) similiar to that used at the Zion plant. Some reinforcing steel is placed in the lower section (approximately 8 cm from tunnel floor) to strengthen the structure. The melt generator mounting ring in the upper section is placed to locate the exit aperature at a scaled height equivalent to the bottom of the RPV.

Instrumentation in the cavity is similiar to that of the 1:20th scale SPIT test fixture. The larger dimensions of the HIPS cavity permit the number of instruments to be increased, with three pitot-static tubes and temperature sensors and two additional gas and aerosol sample tubes. The cavity also incorporates additional diagnostics in the form of optical probes to monitor initial movement of the melt in the cavity. These devices consist of a 6 mm diameter fiber optic probe placed flush with the exposed concrete surface. The opposite end of the probe is monitored with a photodector to give an electrical output when the melt passes over the exposed surface. Time-correlating the position and signal from the various probes gives melt displacement and velocity within the cavity.

Figure 25 shows a conceptial drawing of the assembled HIPS apparatus consisting of the melt generator and test article. The melt generator mounting prevents gas escaping out of the cavity. The assembled apparatus placed in the interaction chamber is shown in Figure 26. The device is placed on the concrete floor of the chamber, near one end with the exit of the cavity directed towards the opposite end. Ejected debris, aerosols, and gases will be retained and measured while in the chamber. Two large fans driven by air motors are used to stir the airborne products of the reaction to obtain a homogenous mixture for sampling.

VII.2 Test versus Accident Characteristics

The ex-vessel behavior of the ejected core debris represents a complicated interaction of chemical, hydrodynamic, and thermal processes. Identifying these phenomena and their possible range of variation is necessary to insure that the experiment accurately models the accident. Table 23 presents the correlation of the experimental and accident characteristics, and the effect on the outcome of the test. The results indicate that the conditions present in the experiment will tend to overpredict the amount of debris dispersed from the cavity. The following paragraphs present the logic that was used to assess the effect of test conditions.

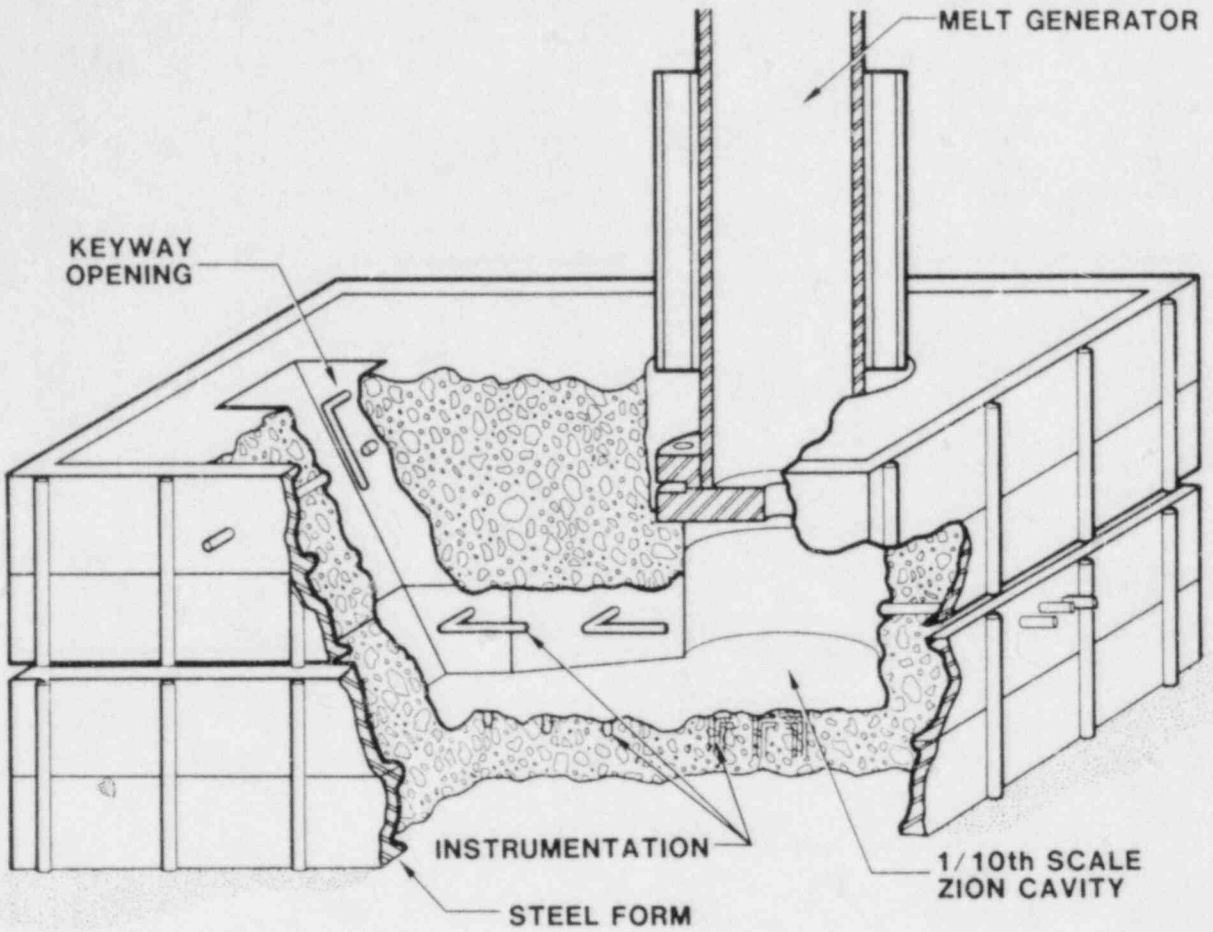

Figure 25. HIPS Test Apparatus

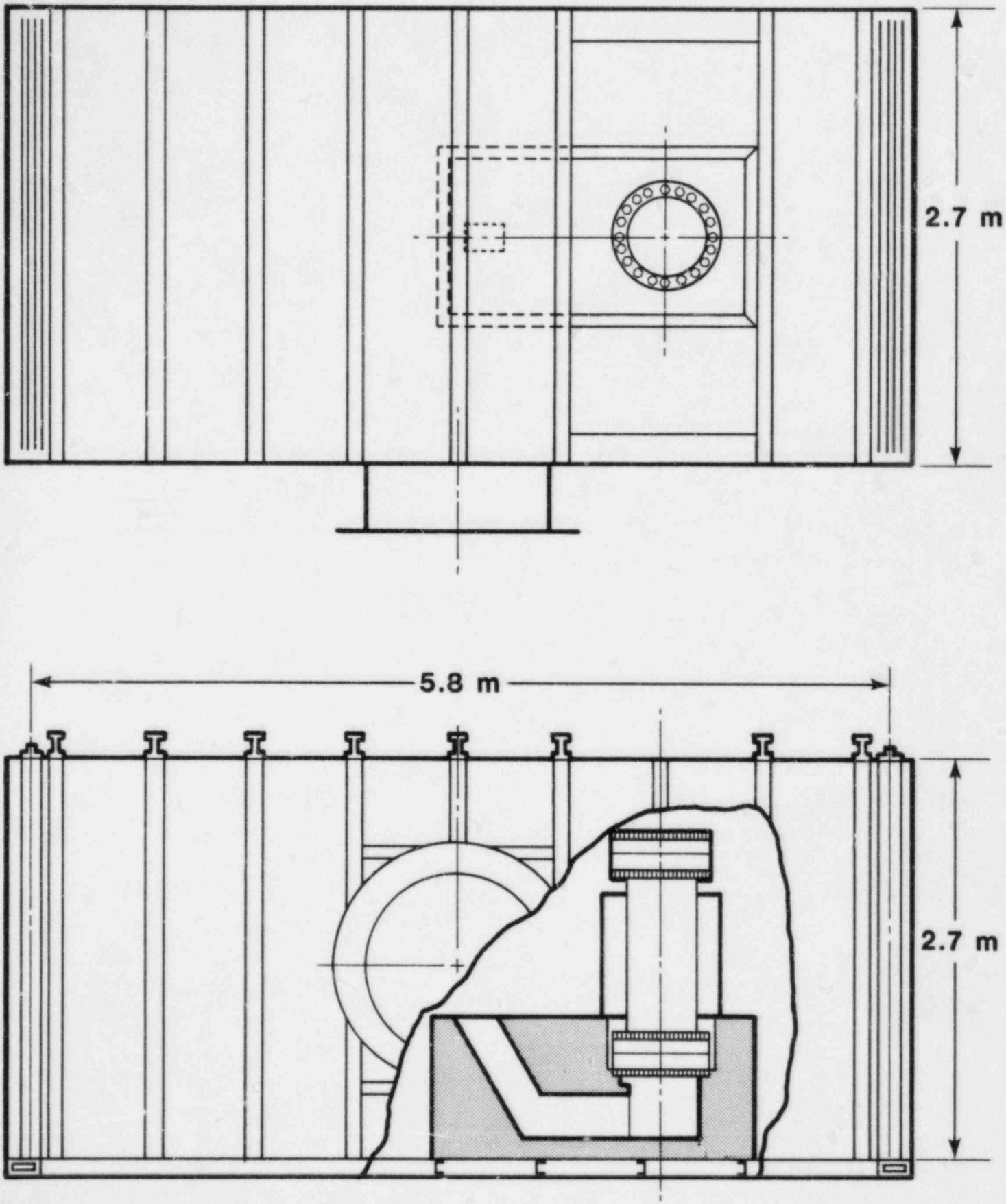

Figure 26. HIPS Test Apparatus Placed in the Experiment Interaction Chamber

TABLE 23

CORRELATION OF ACCIDENT AND TEST PHENOMENA AND THE EFFECT ON TEST OUTCOME

Phenomena	Accident	Experiment	Effect on Test Conditions on Outcome
Pressure	1.4 to 17.0 MPa	1.4 to 17.0 MPa	None.
Gas Volume	Primary System	Melt Generator	Linear scaling approximately 1:12; slightly less total energy in blowdown gas.
Gas Composition	Steam and Hydrogen	Nitrogen/Carbon Dioxide	Higher dynamic head due to N_2 density (factor of 10); will enhance material removal mechanisms. Gas solubility effects in accident unknown. N_2 and CO_2 probably provide upper and lower bounds on solubility, respectively. CO_2 may provide good simulation of steam condensation at blowdown.
Melt Composition	Corium = 7.0 gm/cm^3	Iron and Alumina = 5.9 $/cm^3$	Hydrodynamic mechanisms only slightly affected unless metal/oxide stratification occurs before ejection. Gas solubility, aerosol production, and debris configuration unknown. Freezing point of alumina only slightly lower than $Zr-ZrO_2-UO_2$ mixtures. Experiment temperature a function of non-reactive mass and time in crucible. Too high a temperature may overpredict decomposition and disruption of debris configurations.
Melt Temperature	1500-2800°C	1800-2500°C	May overpredict concrete decomposition compared to lower temperature range. Density and viscosity may be too low--will enhance material removal.
Melt Vessel	RPV	Melt Generator	Length-to-diameter different (2 to .35), causing higher static head; melt depth nominally the same - "punchthru" of gas will not be overpredicted. Flat bottom may enhance atomization and jet breakup.
Breach Dimensions	4-40 cm	2.5 cm (Variable)	Exceeds 1/10th scale; will cause initially higher mass flow of melt and gas enhancing material removal. Thickness to aperature radius approximately 8:1, radial growth of aperature may be slightly underpredicted.
Cavity Geometry	Zion Plant	-	1/10th linear scaling; geometric features not included (ladders, sump, instrument tubes, etc.). Should allow more efficient material removal.
Concrete	Limestone-Common Sand	Same	Aggregate size not scaled; relative amount of "surface" material greater. Initial gas generation and erosion may be enhanced.
Containment Structure	Containment Building	Interaction Chamber	Free-expansion out of keyway; no obstruction to material dispersal. Linear scaling approximately 1:13.
Containment Atmosphere	Possible Elevated Pressure (4 atm) Steam, Hydrogen	Ambient	Greater pressure differential will enhance melt transport out of cavity region.
Water Pool	Dry to 5-m Depth	Dry to 0.4-m Depth	Mixing length (time to initiate) and fragmentation not scaled. Rigid walls will simulate reactor cavity. Growth of steam bubble should be scaled if steam generation is rapid compared to transit times.

The geometry of the reactor pressure vessel is a cylinder with flanged and dished upper and lower heads; the melt generator is a cylindrical pipe section with flat flange covers on each end. Based on the present design, the experiment and accident have nominally equivalent melt depths. This causes the static head to be improperly scaled, but this is no consequence for pressures above 1.4 MPa. But relatively deep melt pool in the experiment could prevent the overlying gas from "punching" through the melt. This effect would contribute to aerosol generation by causing portions of the melt to be entrained by the gas passing through the melt pool. Mechanical breakup of the melt in this manner should cause large particles to be formed. If this process is observed in the experiment it is likely to also occur in a reactor accident.

A second effect of the experimental geometry is the possible atomization of the melt caused by stagnation of the melt flow induced by the flat-bottom geometry of the melt crucible. Atomization of the jet can result in a less coherent stream and enhanced aerosol generation via the production of fine droplets. The curvature of the dished head of the reactor pressure vessel is not significantly different from a flat-bottom vessel. The radius of the Zion RPV is approximately 2.2 meters. For breach diameters up to 10 times the initial hole size, the deviation from a flat plate is less than 2% of the head radius. Atomization of the melt induced by the flat-bottom geometry of the vessel appears to be nearly as likely in the accident as in the experiment.

The above illustrates a situation where the characteristics of both the accident and the experiment are well established. In contrast, some of the accident phenomena are not well known or a range of possibilities must be considered in the design of the experimental matrix. As an example, melt temperature in the accident is not well established, but is assumed to be in the range from 1500°C (steel solidification) to 2800°C (UO_2 melting). Approaching the lower bound, melts are more viscous and resistive to displacement. The reduced superheat causes the material to be more prone to forming a solid crust layer by energy loss from the pool surface. At least three of the melt displacement mechanisms are dependent on an exposed liquid surface. The experimental melt temperature has not been measured, but may be as high as 3000°C, depending on the extent of reaction and the heat losses involved. The uncertainty of the accident melt temperature and the possible consequence of a lower temperature requires that a range of temperatures be considered within the experimental test matrix. Comparing behavior at the high and low extremes of the temperature range permits studying the influence of the melt condition on the debris dispersal and other phenomena.

VII.3 HIPS Test Strategy

The results of the analyses in the previous section suggest that accident characteristics can vary and may change the outcome of the event. Corresponding changes in the test conditions can also be used to better simulate the accident phenomena. The essential step in the test procedure is to determine the accident characteristics that are most influential in the event outcome, while identifying those variables that do not contribute significantly. Addressing each accident characteristic and its range of variation in the experiment would require a large number of tests.

A basic two-factorial test matrix of the critical input characteristics given in Table 9 would require 16 tests total, more than could be handled in a convenient manner. Even a fractional factorial scheme would require at least 8 tests. The HIPS test strategy must therefore be based on performing the experiments that will best satisfy the objective of the program: to verify and quantify the debris dispersal mechanism.

The scaling analysis (Section IV) of the mechanisms hypothesized in the ZPSS indicates that they are most influenced by the initial vessel pressure and temperature. The ZPSS analyses do not account for gas dissolved in the melt or the influence of water in the cavity. Analyses of these latter two effects show that they may also have a significant influence on the debris relocation phenomena.

Lacking the resources to consider a systematic test matrix, the HIPS test strategy will concentrate on establishing the existence of the dispersal mechansims by isolating only the main effects. The technique is illustrated by the logic decision circuit given in Figure 27. The circuit is designed to determine the range of test (and accident) conditions where the ZPSS material dispersal mechanisms exist (or do not exist).

The matrix is initiated by performing the test using conditions considered to be most probable for causing relocation of the melt (HIPS-1). For the purpose of this illustration, the conditions are assumed to be: the highest temperature and pressure values within the prescribed range, and a cavity constructed of a non-reacting material. The test article will be identical to that described in Section VII.1.2 except the cavity region is formed using a layer of magnesium oxide (minimum 5 cm thick). The cavity is constructed by casting the MgO around a Styrofoam form of the cavity dimensions. The material is then baked at a temperature of 400^{o}C for ten hours. The remaining form is then filled with limestone/common sand concrete. The concrete provides rigid support to the ceramic and strength to the overall structure. Additional heating (>150^{o}C) is done just prior to the test to drive off the water absorbed in the MgO material.

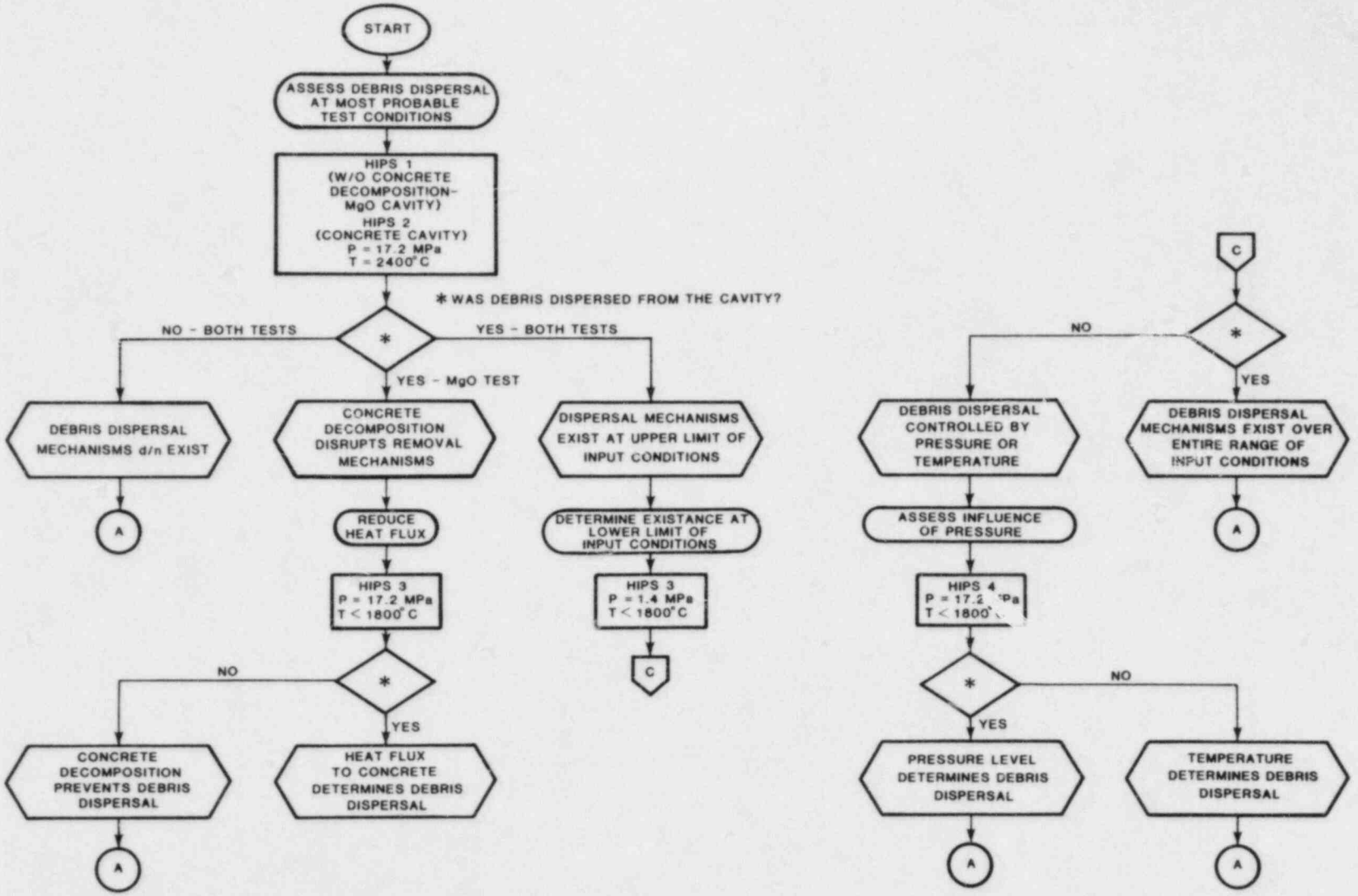

Figure 27a. Logic Decision Network for the HIPS Test Strategy

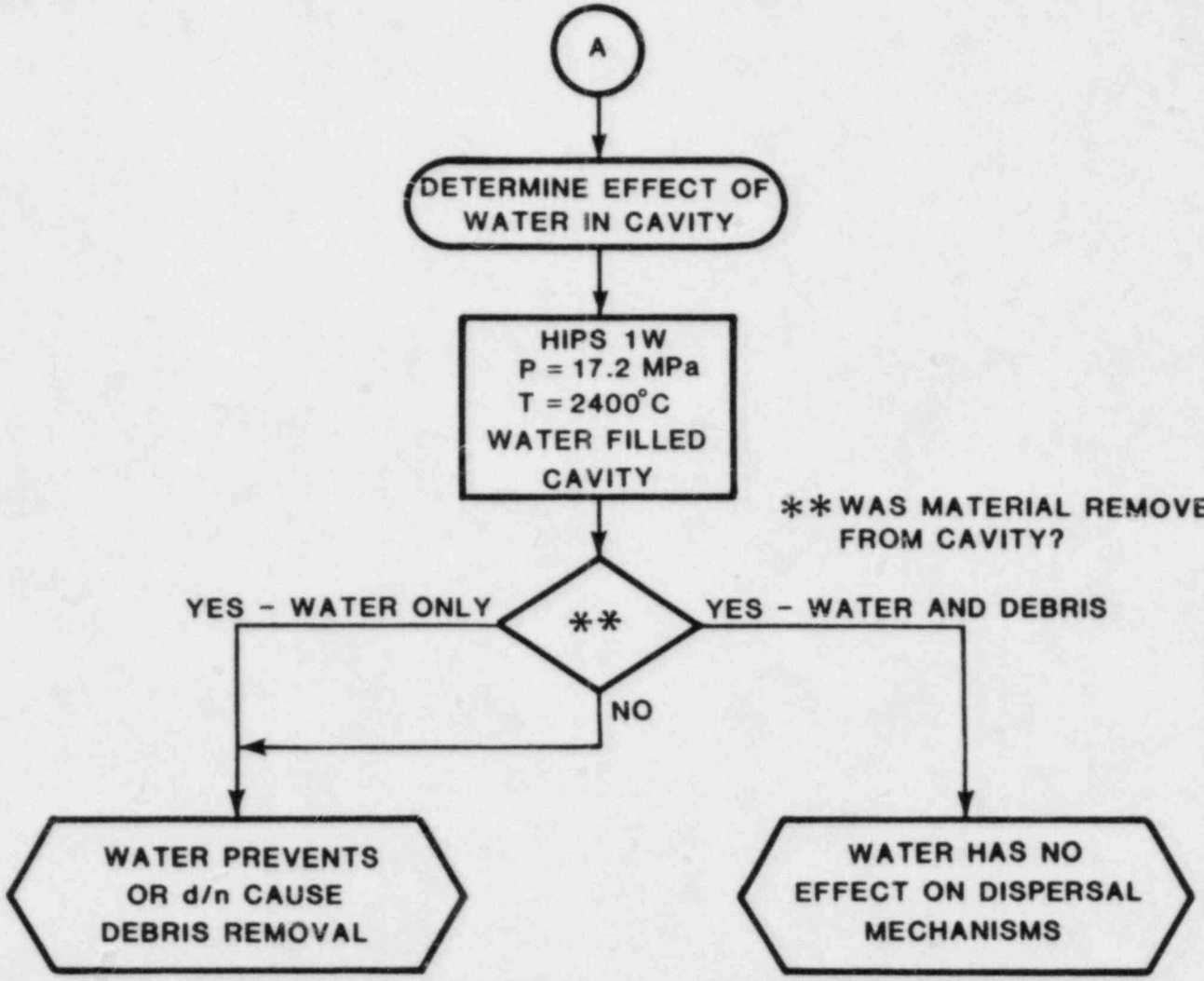

Figure 27b. Logic Decision Network for the HIPS Test Strategy

The second test is identical to the first except that the cavity is concrete. The two tests can then be compared directly to show the influence of concrete decomposition on debris dispersal. It is expected that reducing gas generation from the basemat should inhance material removal by minimizing the disruption of the dynamic debris configuration. The comparison will also show the extent of gas and aerosol generation produced by the concrete decomposition.

Following the second test, the logic path leads to a decision block to decide subsequent tests. If material was not removed from the cavity during both the HIPS-1 and HIPS-2 tests, then the removal mechanisms do not exist. If the melt was displaced in HIPS-1 and not in HIPS-2, then the influence of concrete decomposition on removal mechanisms requires study. Likewise, if material was displaced in both tests, then a lower bounding condition for removal must be established.

Test HIPS-3 is designed with minimum values for pressure and temperature to determine if material removal occurs for the lower bound of the accident conditions. If removal occurs at the these values of pressure and temperature, then the mechanisms are assumed to be active over the entire range of system conditions. If material is not displaced in this test, then one or two additional experiments are required to determine if pressure or temperature is the dominating influence.

The results from the HIPS tests numbered 1 through 5 (or 1 through 3) will establish the principal main influence on debris dispersal. The data from the tests will be used to model the processes of debris dispersal, aerosol generation and transport, concrete decomposition and gas production, and the fission product source term. The Phase II SPIT data will also be used in conjunction with these results to aid in developing appropriate scaling criteria.

The second portion of the decision circuit considers the effect of a cavity water pool on debris dispersal. The Phase II SPIT matrix is planned to investigate the influence of water using structures constructed of benign materials. The results of the SPIT experiments will determine the differences, if any, between fully and partially-filled cavities and the magnitude of the resulting interactions. If significant differences are noted between the two cases, then the HIPS test matrix will also consider the two situations. The logic circuit incorporates both classes of experiments, the decision to pursue both paths will be based on the analysis of the SPIT tests.

Test HIPS-1W is designed to study the condition where melt is ejected under high pressure into a "water-locked" cavity. The objective of the test is to confirm the ZPSS hypothesis that melt will initiate a steam bubble causing explusion of the water from the cavity. Because this test represents a new condition within the spectrum of possibilities, all previous paths in the logic

circuit are subsequently directed along this branch, regardless of previous outcomes. If necessary, HIPS-2W will also be conducted at identical conditions except for a shallow pool depth.

The HIPS test program described above will not provide definitive information about all possible combinations of accident conditions, but only those main factors that appear to be most critical to the debris dispersal mechanisms. Conducting tests at the extremes of the spectrum of possibilities for these factors will permit statements to be made concerning the bounds of potential test outcomes and modeling to be initiated.

VIII. Summary

The Zion Probabilistic Safety Study represents an extensive and innovative analysis of the risks involved in operating the Zion plant. Within the context of the ex-vessel interactions, the document proposes a number of unique mechanisms that may result in removal of the core debris from the cavity region. The resulting distribution is considered coolable by the existing plant mechanisms.

The High Pressure Melt Streaming program has been developed to experimentally and analytically study the phenomena associated with the ex-vessel accident sequences. Tests are planned at two different scales with initial conditions varied over the entire range expected in the accident. The results will form a data base for describing the ejected jet stream, jet-concrete interactions, debris removal processes, and aerosol generation.

The System Pressure Injection (SPIT) test matrix is designed to characterize the jet behavior and aerosol generation during melt ejection. Thermitic melts up to 10 kg will be generated under pressures of 1.4 to 17.0 MPa. Carbon dioxide and nitrogen will be used to determine the influence of gas solubility on jet and aerosol behavior. A statistical approach is used to develop the test matrix to insure that the influence of the significant variables is considered over the range of conditions.

The SPIT matrix will also include a limited number of tests investigating the interaction of the melt jet and water pools. The results of these tests will be used to design instrumentation and equipment for subsequent, larger scale tests. The data will also check the validity of the ZPSS hypotheses concerning the influence of water pools on the debris dispersal processes.

A 1/20th linear scale model of the Zion cavity will be tested using the SPIT apparatus. The prototypic concrete composition is used to construct the test article. The test will be performed at initial conditions most likely to cause dispersal of the debris out of the cavity region.

The results from the SPIT testing provide the basis for conducting the larger scale HIPS experiments. The HIPS test matrix concentrates on verifying the existance of the debris dispersal mechanisms over a range of conditions. The geometry of the HIPS apparatus represents a 1/10th linear scale of the Zion cavity. The melt generator contains up to 80 kg of a thermitically-generated iron-alumina mixture, at pressures up to 17.0 MPa. The concrete test article is instrumented to measure the varibles needed to support verification and modeling analyses. Placing the apparatus in a large interaction chamber allows retaining and sampling the products of the interaction process.

The HIPS test matrix is designed to isolate the main factors contributing to the debris dispersal mechanisms. A logic decision circuit is used to determine the progression of test conditions. The influence of water within the cavity is also included within the logic circuit.

The results of the SPIT and HIPS tests are expected to be used in developing analytical tools for describing the jet propagation, aerosol generation, and debris dispersal processes. The experiments will also provide data for scaling analyses to extrapolate the phenomena to reactor scales. Ultimately, the models will be used to predict behavior for other cavity geometries and differing system conditions.

APPENDIX A

Phase I SPIT Test Program

The Phase I SPIT test program was initiated to devlop a high pressure melt generation and delivery technique. During the course of the program, unexpected phenomena were observed that required the design of specialized instrumentation and caused the tests to become progressively more complex. This section provides a brief overview of the test results with the discussion principally concerning the nature of the jet stream and the aerosol samples. A listing of the pertinent test details is given in Table 24.

A.1 Jet Characteristics

The nature of the jet emanating from the reactor vessel will have a direct influence on the subsequent behavior of the melt within the cavity. The initial shape and velocity of the jet forms the dynamic debris configuration that is hypothesized to promote removal of the material from the cavity. The assumption in the ZPSS analysis is that a stable, single phase jet is formed so that no geometric expansion occurs during passage to the cavity floor. A solid jet maximizes the unit pressure loading that, in turn, causes the material to traverse rapidly across the cavity floor. An analysis given elsewhere in this report suggests that gas solubility and mechanical breakup may cause the material leaving the vessel to be an unstable, two-phase mixture.

The Phase I SPIT tests show that the appearance of the melt stream is radically different than that presumed in the ZPSS. Figure 28 is a series of representative photographs taken during the SPIT-3 test. The times stated are referenced to the first appearance of the jet and are accurate to $\pm$ 0.02 second. The melt jet at 0.05 second is characterized as a highly luminous, divergent cone (35-40^{o} half-angle) emanating from the vessel. The brightness of the cloud prevents resolution of any details other than the outer shape. The material within the cone appears to be vaporized melt. At 0.1 second, the cone is still apparent, but the lower portion is masked by material that has condensed and darkened. Some of the condensed material has deflected off the brick bed as indicated by its upward and outward direction. Approximately 1 second later (t = 1.15 sec), the aerosol cloud completely envelops the apparatus. The dark-brown appearance indicates that the material has cooled significantly. The behavior within the cloud interior is not discernable.

Figure 29 shows two flash X-ray photographs of the melt stream taken during two separate SPIT tests. The experiments were conducted at nominally the same conditions except for the

TABLE 24

Details of SPIT Tests

Test	Date	Melt Mass (kgs)	Pressure (MPa) Initial	Final	Gas	Comment
SPIT-1	25 May 82	2.15	Amb	0.69	Ar	No melt thru, relief valve set at 0.69 MPa.
SPIT-2	26 May 82	2.37	Amb	0.67	Ar	Relief valve opened prior to melt thru, gaseous melt.
SPIT-3	3 Jun 82	2.50	1.03	1.88	N_2	Gas did not vent, melt "sprayed" sequentially in 3 directions.
SPIT-4	23 Jun 82	10.35	1.03	8.10	N_2	No melt thru, relief opened at 7.24 MPa, 350 gm La_2O_3 mixed in thermite.
SPIT-5	24 Jun 82	10.35	0	?	N_2	350 gm La_2O_3, no pressure record, instrumented MgO brick bed.
SPIT-6	28 Jul 82	10.6	3.45	5.16	N_2	Pressure vessel failure
SPIT-7	20 Sep 82	10.4	2.99	4.77	N_2	10 cm deep Al_2O_3 gravel bed, melt penetrated and removed bed.
SPIT-8	29 Sep 82	10.4	7.24	7.62	N_2	30 cm deep Al_2O_3 gravel, melt penetrated 20 cm into bed, no displacement of particles. Steel calorimeter.
SPIT-9	3 Nov 82	5.0	3.45	?	N_2	Real time x-ray of thermite reaction
SPIT-10	10 Nov 82	5.0	2.52	3.16	N_2	Real time x-ray of thermite reaction
SPIT-11	7 Mar 83	10.0	6.32	8.40	CO_2	First CO_2 test, no trigger on x-ray units
SPIT-12	11 Mar 83	10.0	5.71	5.52	CO_2	Coherent stream with ligament instabilities, max heat flux 400 cal/cm^2-sec
SPIT-13	17 Mar 83	10.0	5.13	17.24	CO_2	Extreme pressure increase during reaction, highly fragmented melt.

TABLE 24 (CONT.)

Details of SPIT Tests

Test	Date	Melt Mass (kgs)	Pressure (MPa) Initial	Final	Gas	Comment
SPIT-14	6 Jun 83	10.0	1.59	1.68	CO_2	Lowest pressure value, large aerosol generation
SPIT-15	27 Jun 83	10.0	6.87	11.67	N_2	Solid water pool, jet penetrated water at approx. 16 m/sec, no vapor explosion, box destroyed
SPIT-16	22 Jul 83	10.0	9.08	10.54	N_2	1/20 scale aluminum cavity, water filled, melt failed to vent
SPIT-17	25 Jul 83	10.0	8.76	10.21	N_2	Repeat test 16, over 200 MPa pressure spike in water pool (approx. 13 msec after jet entry), cavity destroyed
SPIT-18	9 Nov 83	10.3	10.62	12.26	N_2	Alumina brick cavity, placed in 42 m^3 chamber, approx. 58% of debris dispersed from cavity, several psi overpressure of recorded in chamber
SPIT-19	16 Dec 83	10.3	10.76	12.77	N_2	Scaled (1/20) Zion reactor cavity, limestone/common sand concrete, placed in 42 m^3 chamber, significant overpressurization of chamber caused extensive damage. Approx. 95% of debris removed

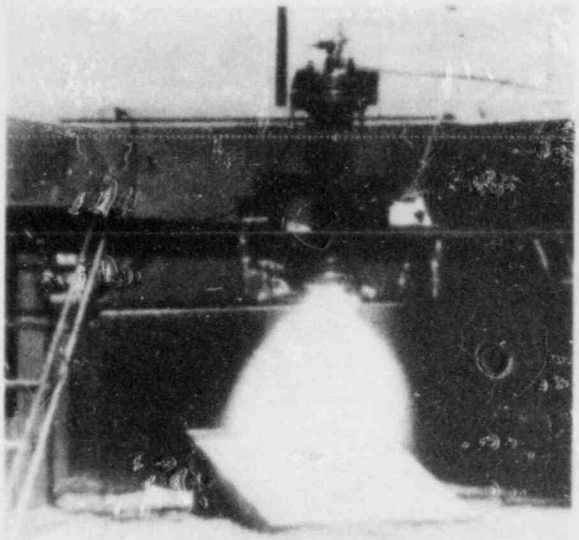

t = 0.05s

MELT EJECTION BEGINS

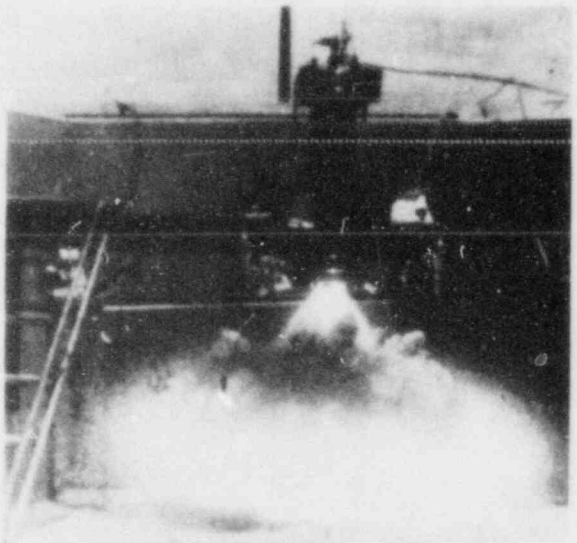

t = 0.1s

VAPOR CONDENSATION

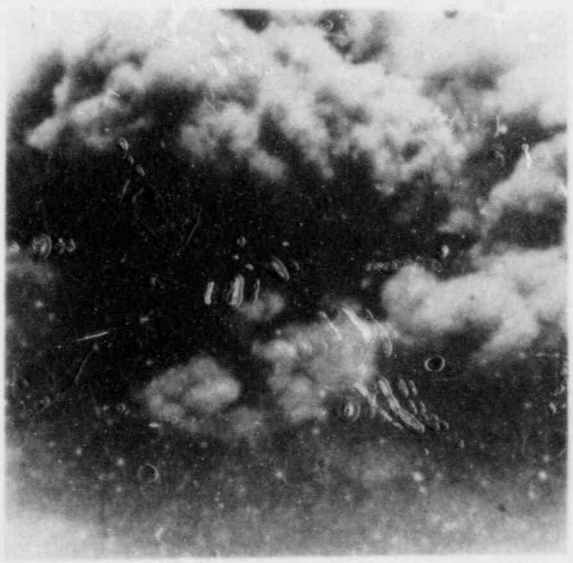

t = 1.15s

MAXIMUM AEROSOL CLOUD

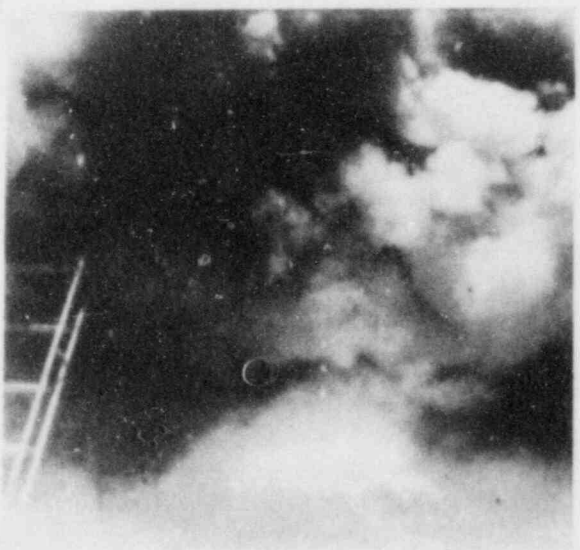

t = 1.95s

RESIDUE OF EJECTION

Figure 28. Melt Ejection Sequence

TEST 8 – 7.6 MPa N_2

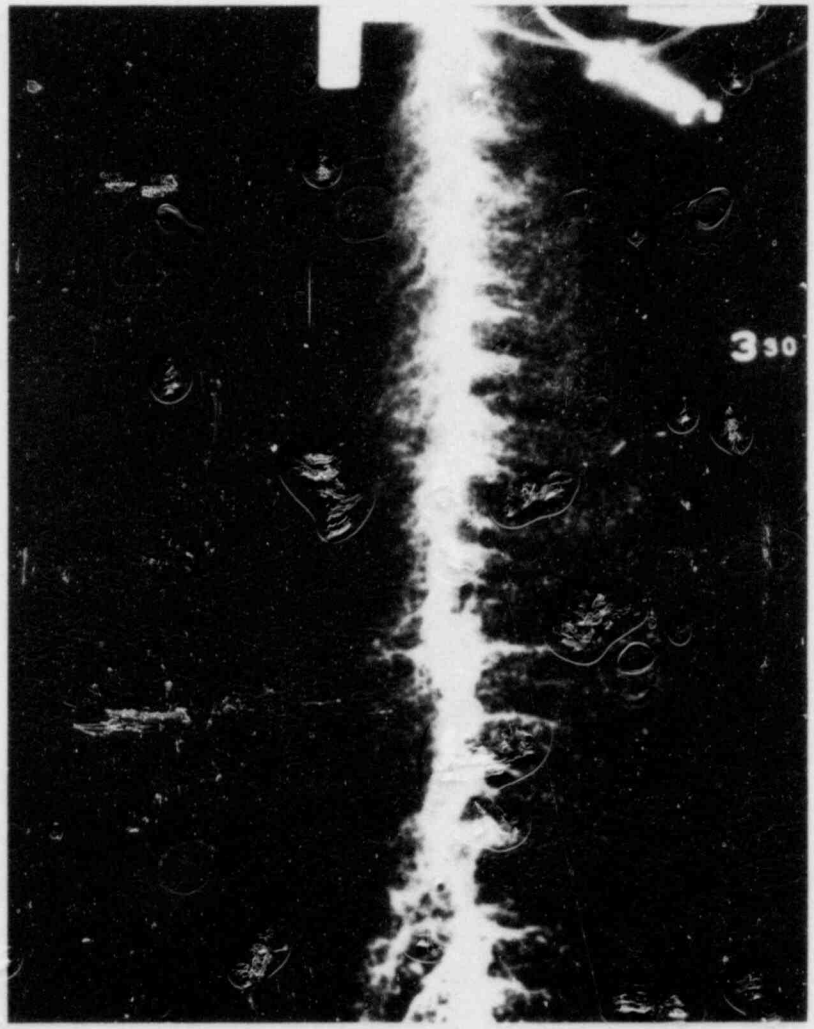

TEST 11 – 8.3 MPa CO_2

Figure 29. Flash X-ray Photographs of Jet Stream

type of gas. SPIT-8 was charged with nitrogen while SPIT-11 used carbon dioxide. The outward apparance of the jet was very similar to that seen in Figure 29. The time given in each photo is referenced to a signal generated by a break-wire trigger placed under the melt plug. The response of the trigger to the melt is estimated to be approximately 4.5 ms. Four x-ray units are typically used on each test, located at a radius of approximately 2 meters from the melt stream and positioned approximately 25° apart. Film cassettes are placed diametrically opposite the corresponding X-ray head, approximately 0.46 meter from the stream center.

Both photos show the melt jet at 45 milliseconds after the break-wire signal. The large nuts securing the lower melt generator flange are obvious in the upper portion of the figures. The photo from SPIT-8 shows slightly over half of the melt stream. The boundary of the stream is clearly defined, suggesting that the surrounding cloud seen in the photographs of Figure 29 is significantly less dense. The half-angle of the jet stream is on the order of $10\text{-}12^{\circ}$. Using the position of the stream front and the time of exposure gives an estimated velocity of 20 m/sec.

The estimated velocity can be compared to that obtained using Bernoulli's equation to determine if the jet behaves as isentropic fluid flowing through an orifice.

$$U = \left[\frac{2(P_o - P_a)}{\rho_F}\right]^{1/2} = \left[\frac{2P_{og}}{\rho_F}\right]^{1/2}$$

where:

$P_o - P_a = P_{og}$ = pressure in the melt generator (gage pressure)

ρ_F = density of melt (fluid)

$$U = \left[\frac{2(7.62 \times 10^5)\,N/m^2}{5900\ kg/m^3}\right]^{1/2} = 16.1\ m/sec$$

For this example, the discharge coefficient of the orifice is assumed to be unity. The comparison is resonable considering the large uncertainty in the experimental value.

As the jet expands and moves downward, the density of the stream appears to decrease, as evidenced by the appearance of voids within the structure. A pattern of density concentrations in the form of horizontal bands is apparent in the lower third of the stream. These bands may be caused by Helmholtz instabilities

that occur as the internal pressure of the stream equilibrates with the surrounding environment.

Helmholtz instabilities arise when two immiscible fluids flow relative to each other along a surface of separation. There exists a maximum relative velocity above which a small disturbance on the surface will grow and amplify. The SPIT geometry can be approximated using a correlation (Ref. 36) for a downward liquid jet and an upward vertical vapor blanket. The velocity of propagation of surface wave is given by:

$$C^2 = \frac{\sigma m g_c}{\rho_\ell + \rho_v} - \frac{\rho_\ell \rho_v}{(\rho_\ell + \rho_v)^2} (V_v - V_\ell)^2$$

where:

σ = surface tension of liquid

$m = 2/\lambda$ wave number

g_c = proportionality constant

λ = wavelength of disturbance

ρ_ℓ, ρ_v = density of liquid and vapor

V_ℓ, V_v = velocity of liquid and vapor

The condition for a stable jet requires that $C^2 \geq 0$, or

$$\frac{2\sigma g_c}{\lambda} - \frac{\rho_\ell \rho_v}{(\rho_\ell + \rho_v)} (V_v - V_\ell)^2 > 1$$

This criteria can be evaluated for SPIT-8 by assuming that $\sigma = 1000$ dyne/cm, $V_\ell = 20$ m/sec, $V_v = 0$, and that the wavelength of the observed disturbances is on the order of 2 cm.

$$\frac{3141}{4799} = 0.65 < 1$$

The result suggests that for the jet in the SPIT-8 test, the relative velocity of the stream is high enough to induce instability on the surface of the stream. Instability effects should become even more pronounced at higher driving pressures due to the dependence on the square of the relative velocity term.

The second radiograph in Figure 29 shows the appearance of a CO_2-driven melt. In this case, the jet appears as a nearly coherent stream with ligament-type instabilities emanating from the surface. No large voids or lower density areas are obvious

within the stream, as would be expected without gas in solution. The estimated velocity is nearly equivalent to that seen in SPIT-8 with the higher density apparently offsetting the increased system pressure.

A.2 Aerosol Generation

Cascade impactors and filter samples were employed on SPIT tests 3, 5, 6, and 8. The devices are placed near the apparatus so that they are enveloped by the aerosol cloud. Remotely controlled valving permits samples to be drawn into the devices at predetermined time intervals. Typically, the devices are activated at ignition and closed after the aerosol cloud dissipates. Cascade impactors allow the sample to be sized according to aerodynamic diameter based on seven size ranges incorporated into each device. Filters are used to obtain a mass of aerosol over a fixed time period. Using a known flow rate allows inferring a mean concentration. The captured material from both types of devices can be used in chemical analyses to determine speciation.

Cascade impactors of the type used on the SPIT tests are most efficient in sampling aerosols in the range of slightly less than one-half micrometer to about 15 micrometers (aerodynamic diameter). The low mass of smaller particles causes them to be carried through the device without impacting on a collection surface. Large particles behave in an opposite manner; their momentum may be too great to be deflected out of the aerosol cloud into the apparatus. Filters are similarly affected in the large size range but are more efficient in capturing the lower size range.

Cascade impactor data from the SPIT-3 test are presented in Figure 30 in the form of frequency of occurrence as a function of particle diameter. The curve fit to the data suggests two distinct modes, 0.5 and 5 micrometer aerodynamic diameter. The smaller mode is assumed to be formed by the condensation of the vaporized species in the highly luminous cloud surrounding the melt jet. The larger mode is attributed to mechanical breakup of the melt, possibly by fragmentation induced by atomization of the melt at the exit aperature of the vessel.

As the jet enters the atmosphere, the surface material is exposed to a high relative velocity gas stream that causes hydrodynamic fragmentation. The droplets can undergo a multistage breakup process until a stable fragment size is achieved. For this situation, the fragment diameter size is given by (Ref. 13):

$$d = We_c \frac{\sigma}{\rho_g V_g^2} \left[1 - \frac{V_d}{V_g}\right]^{-2}$$

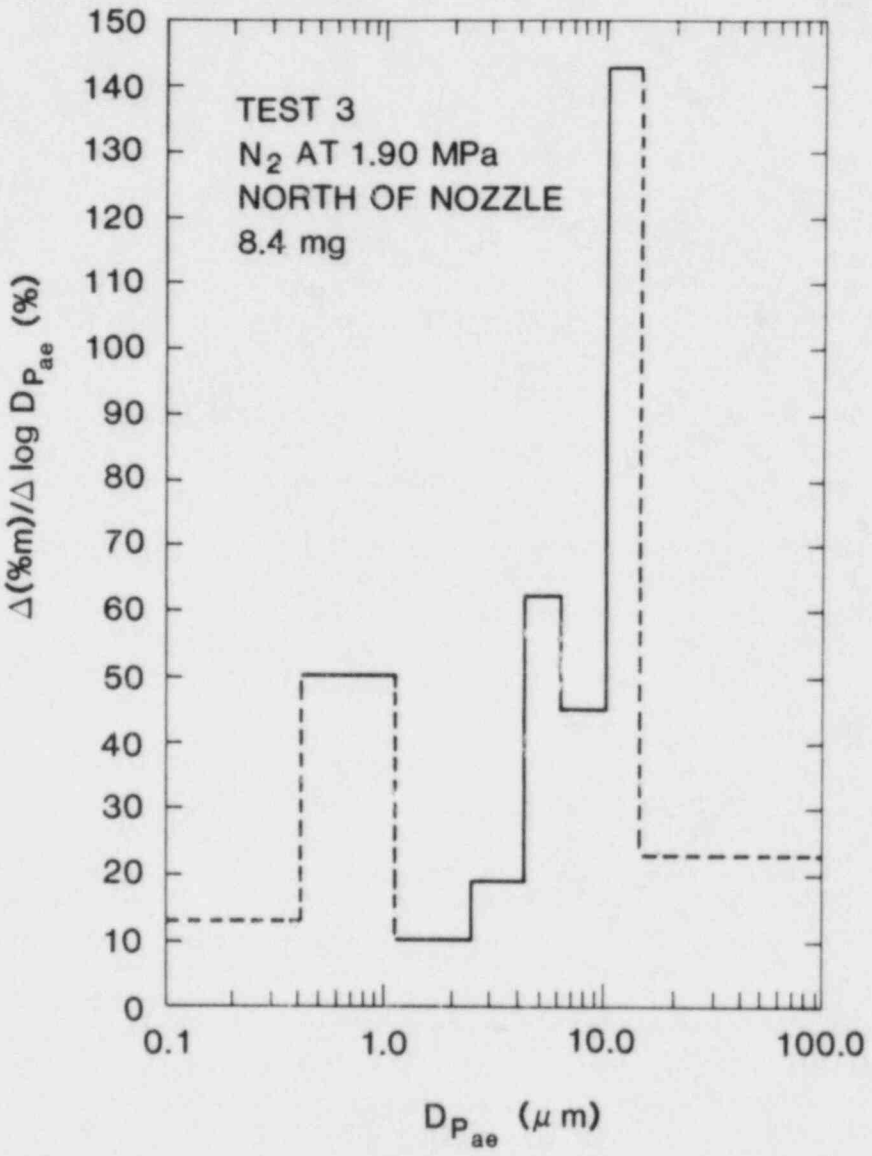

Figure 30. Size Distribution of Aerosol Produced During Pressurized Melt Ejection

where:

We_c = critical Weber number

d = maximum fragment size when the processes are complete

V_d = fragment cloud velocity after the fragmenting process

ρ_g; V_g = density and velocity of the gas stream

σ = droplet surface tension

This equation accounts for Weber number reduction by both particle size reduction and relative velocity reduction. Applying typical values from the SPIT-type tests indicates that the atomization process can yield stable particles in the 10- to 100-micrometer size range. Material recovered from the impactor pre-filter used during the SPIT-8 test are consistent with these results. Microscopic examination of the particles shows a mean size of nominally 65-micrometer aerodynamic diameter. This material was not found on the impaction stages of the sampler, probably because of the device's low collection efficiency for larger particles.

Electron microscopic examination is used to determine the geometry of the aerosol particles. Representative samples of the three sizes mentioned above are shown in Figure 31. The smallest particles (0.5-micrometer average diameter) appear to be composed of aggregates of small (<0.1-micrometer) primaries. The 0.1-micrometer particles probably represent the material formed during the condensation process with the aggregates created by collisions, while the individual particles settled out or were lost during the sampling. The 5-micrometer and 65-micrometer particles appear to be principally single, spherical shapes, consistent with the proposed generation mechanisms of aerodynamic fragmentation

Energy dispersive spectroscopy of the samples shows the two smaller size ranges to be selectively either iron- or aluminum-bearing. None of the samples that were analyzed showed aluminum and iron coexisting in the same particle. Quantitatively, more iron-bearing particles were observed than aluminum. The relative lack of aluminum composition particles in the smaller size range may be due to the higher vapor pressure of iron compared to aluminum (Figure 32). The 65-micrometer samples do show both iron and aluminum within the particle. Figure 33 illutrates the results of this type of analysis on the 65-micrometer sample. The silica and zirconium are assumed to be impurities existing in the melt. The lanthanum is derived from an oxide form placed in the thermite charge prior to the test.

Dp =65 MICRON

Dp = 5 MICRON

Dp = 0.5 MICRON

Figure 31. Electron Micrographs of SPIT Aerosol Samples

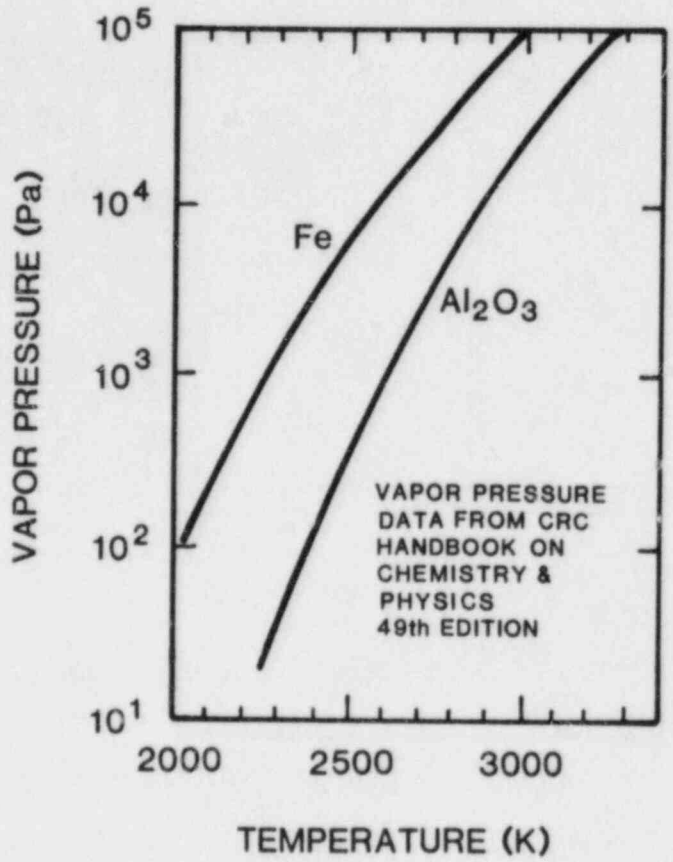

Figure 32. Vapor Pressure of Iron and Aluminum Oxide as Functions of Temperature

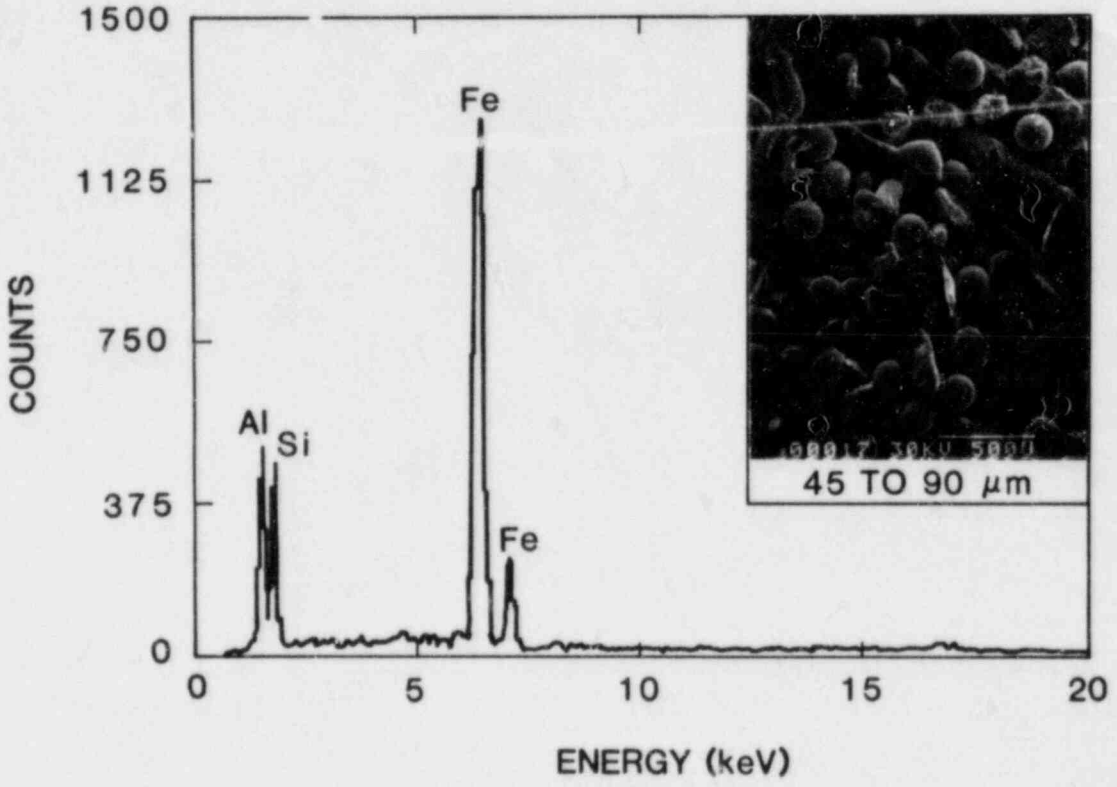

Figure 33. Elemental Analysis of 5-micrometer Particle

APPENDIX B

Gas Blowdown of SPIT Apparatus

The pressurized components of the SPIT apparatus are the melt generator, accumulator reservoir and interconnecting plumbing. The accumulator provides an expansion volume for the gases liberated and heated during the thermite burn. The gas volume of the melt generator is estimated to be 5.9×10^{-3} m^3 and the reservoir volume is approximately 2.8×10^{-2} m^3. The interconnecting piping represents a neglible contribution in volume. The two volumes should not be considered to be additive because the interconnecting tubing may be too restrictive to insure simultaneous blowdown. This point can be illustrated by a simple isentropic flow analysis of the discharge from the melt generator and the flow through the interconnecting piping.

For an ideal gas, the mass flow rate of a reversible adiabatic expansion through an orifice is given by (Ref. 35):

$$\dot{m} = \frac{CA_2 P_2 \left[\frac{2}{RT_1} \frac{k}{k-1} \left(\frac{P_1}{P_2}\right)^{k-1/k} \left(\left(\frac{P_1}{P_2}\right)^{k-1/k} - 1 \right) \right]^{1/2}}{\left[1 - \left(\frac{A_2}{A_1}\right)^2 \left(\frac{P_2}{P_1}\right)^{2/k} \right]^{1/2}}$$

where:

C = orifice discharge coefficient

A_2 = area of orifice

P_2 = ambient pressure

R = gas constant

T_1 = temperature of gas in the melt generator

k = ratio of specific heats

P_1 = pressure in melt generator

A_1 = cross-sectional area of melt generator

The discharge coefficient (C) can vary from 0 to 1.0, the final value depends on the ratio of A1/A2, type of gas, velocity through the orifice, and other factors.

Flow through a pipe is governed by the inertial, viscous, pressure, and elastic forces. Assuming isothermal flow the mass flow rate through the interconnective piping is given by (Ref. 35):

$$\dot{m}_2 = \frac{\left(P_0^2 - P_1^2 \right)^{1/2}}{\left[\frac{2RT}{gA^2} \ln\left(\frac{\rho_o}{\rho_1}\right) + \frac{4f'RTL}{gA^2D} \right]^{1/2}}$$

where:

P_o, P_1 = pressure in accumulator and melt generator, respectively

ρ_o, ρ_1 = density of gas in accumulator and generator

D, L, A = diameter, length, and area of pipe, respectively

g = acceleration due to gravity

f' = pipe friction factor

If the Reynold's number in the pipe exceeds 4,000, turbulent flow can be assumed and the friction factor is given by the Colebrook equation (Ref. 35):

$$f' = \frac{Y^2}{4}$$

$$\frac{1}{Y} = 2 \log_{10} \left(\frac{\varepsilon/D}{3.7} + \frac{2.51}{R_e Y} \right)$$

where:

ε = empirical value for surface roughness

R_e = Reynold's number = $\frac{VD}{\mu}$

V = velocity of flow

μ = viscosity of gas

In order to obtain the blowdown history of the SPIT apparatus, the above three equations must be solved simultaneously.

The initial conditions of the problem are given by the pressure, temperature, and type of gas in the pressure system. The pressure in the generator at any point in time is determined by the amount of mass that has flowed out of the vessel through the melt plug orifice minus the mass that has entered the generator via the interconnecting plumbing.

For the purpose of illustrating the behavior of the system, the following values are selected for the base case:

$$P_1 = 15.2 \text{ MPa} \qquad T_1 = 1670 \text{ K} \qquad T_2 = 330 \text{ K}$$

$$A_2 = 5 \times 10^{-4} \text{ m}^2 \qquad C = 0.8$$

The sensitivity of the calculation to changes in the values of the variables is illustrated by comparing the base case response to the variation in the system parameters. The range in values is assumed to be representative of the possible variation in the experiment. In Figure 34a, the discharge coefficient and the effective flow area are varied. As shown, the calculated blowdown times are inversely proportional to the change in the parameters. In all three cases, the accumulator pressure does not change significantly during the blowdown of the melt generator. The small flow area of the interconnecting plumbing is too resistive to allow significant gas flow from the accumulator to the melt generator. A pressure decrease on the order of only 10 kPa in the accumulator pressure is predicted for these cases.

Figure 34b provides a comparison to the base case for variations in the gas temperature, pressure, and species. Both temperature and species are significant contributors to the response of the system, basically due to the influence of the (RT) product in both flow equations. The major effect of the decrease in system pressure is to cause a longer discharge time by decreasing the mass in the system. The results for all cases show that the accumulator volume does not significantly contribute to the blowdown response of the system.

To further assess the effect of the piping on the response of the system, a calculation was made where the piping was considered to have the same volume, but of an infinitesimally small length. In this hypothetical situation, the system volume is maintained, but the entire contents are essentially available for discharge through the orifice in the melt genertor. Figure 35 illustrates the comparison between the hypothetical situation and the base case of Figure 34.

Figure 35 shows that the additional volume contributes significantly to the time required for the melt generator to equilibrate with the ambient conditions. Because the mass flow rate is the same for both cases, the comparison illustrates that the interconnecting piping is functioning as an acoustic low-pass

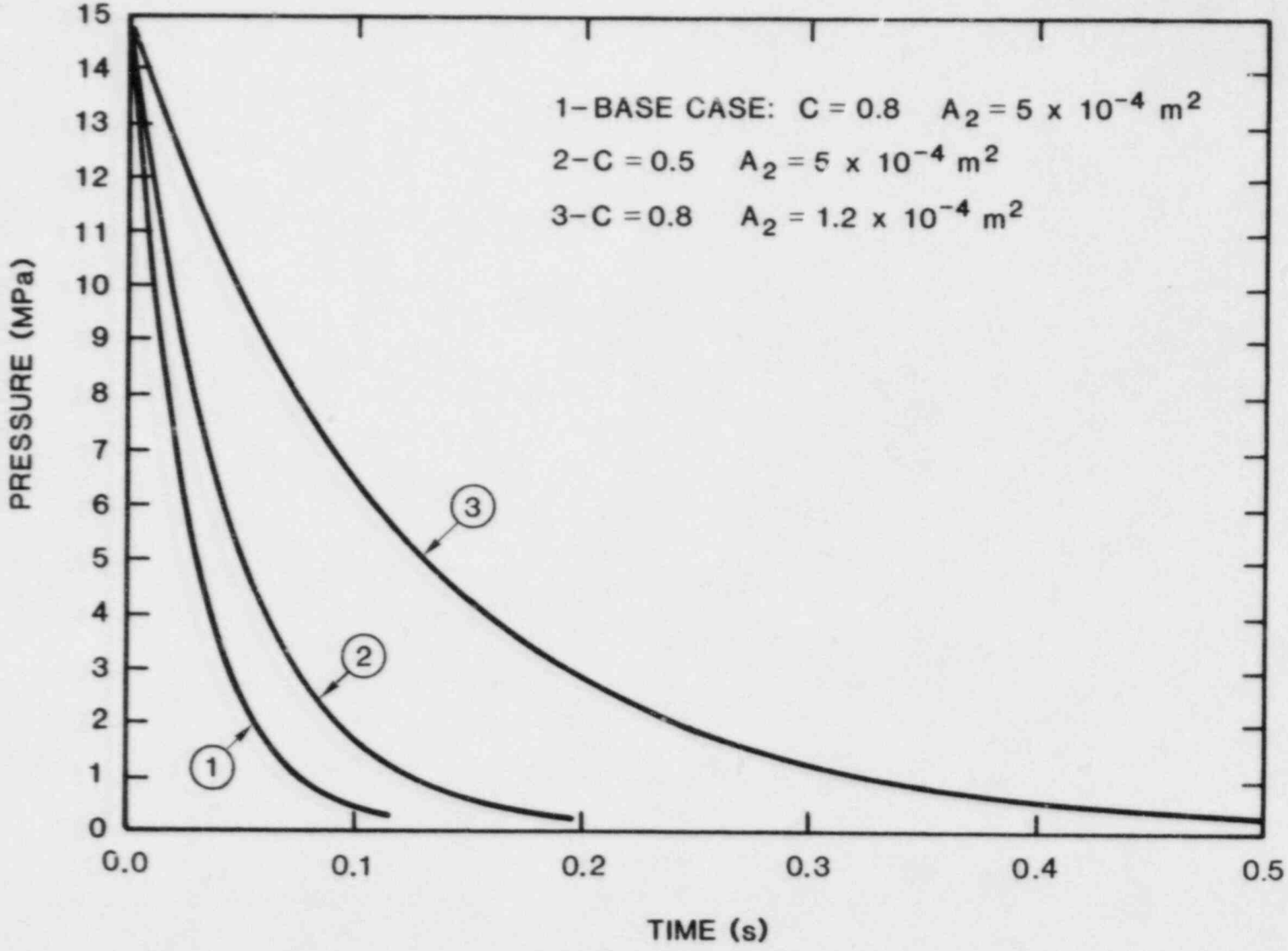

Figure 34a. Calculated SPIT Pressure Vessel Blowdown History for Variation in Orifice Size and Discharge Coefficient

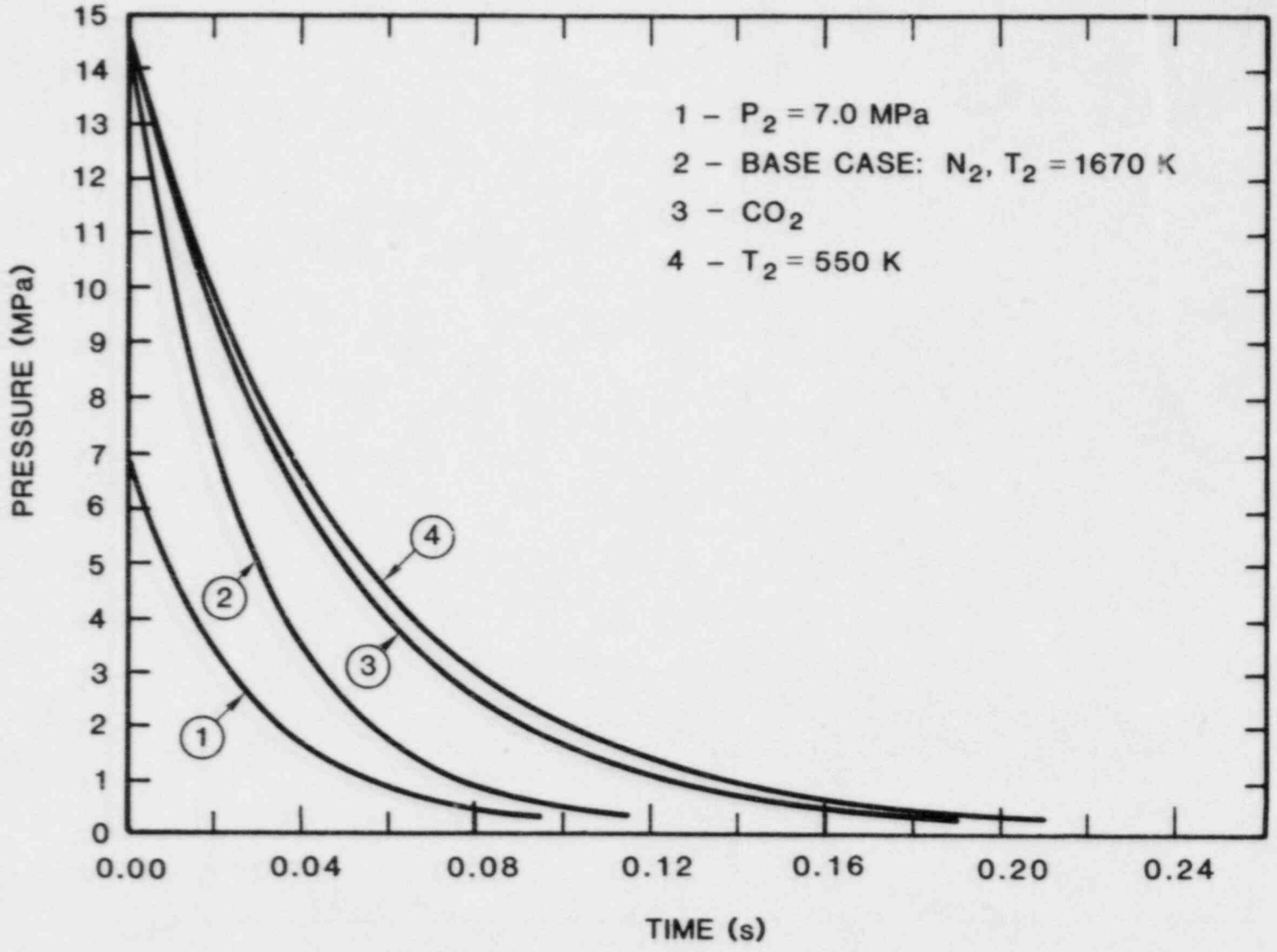

Figure 34b. Calculated SPIT Pressure Vessel Blowdown History for Variation in Gas Pressure, Species and Temperature

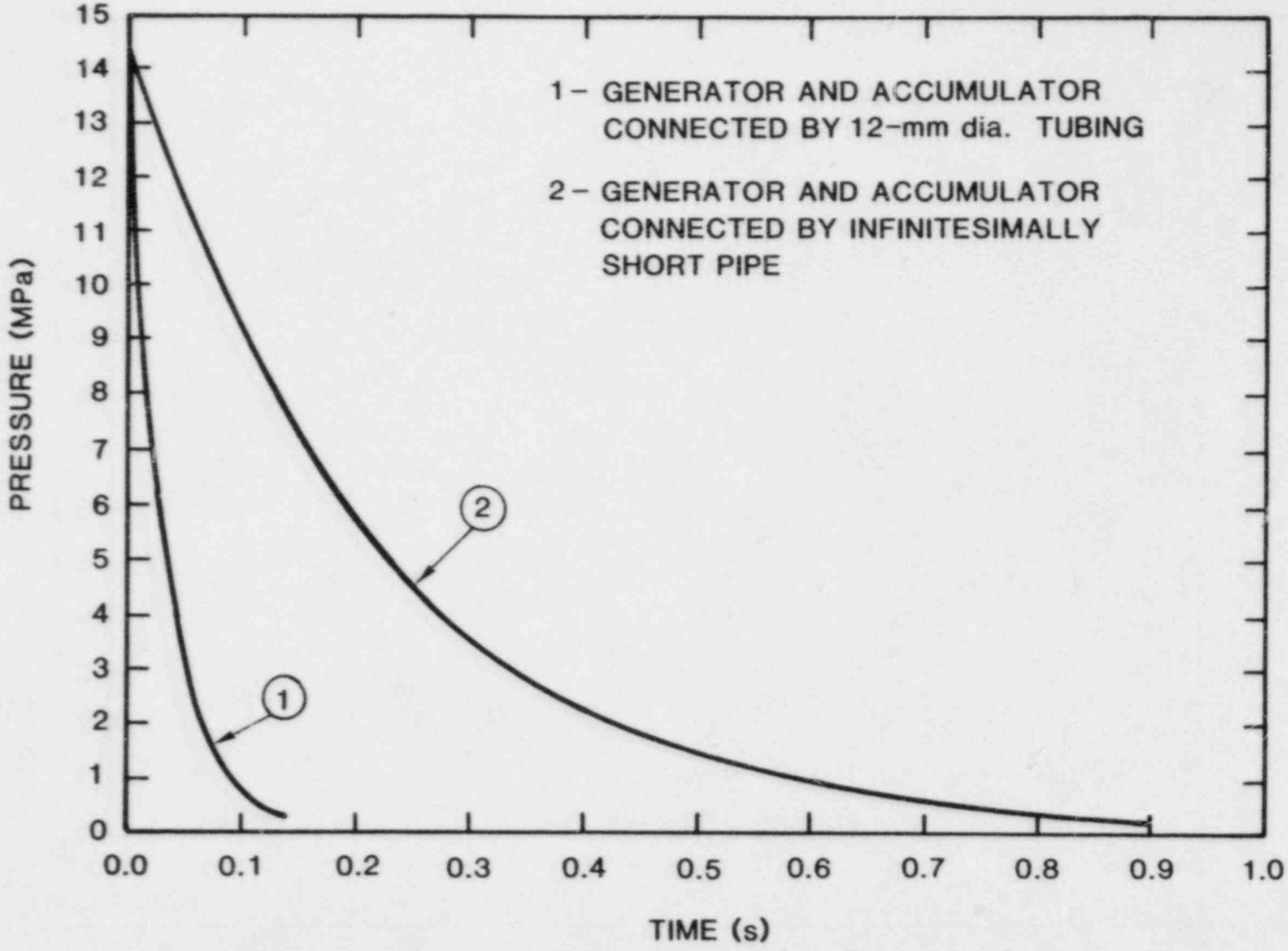

Figure 35. Effect of System Volume on Blowdown History for Variation in the Interconnecting Piping

filter, preventing a rapid discharge of the accumulator. Likewise, the large orifice in the melt generator prevents significant additional pressurization after blowdown by the flow of gas from the accumulator. An equilibrium pressure of just under 2 atms is maintained until the accumulator is discharged. The implication of these results is that the accumulator volume should not be included in calculations involving a blowdown of the system volume.

Considering the generator volume alone gives an approximate 1/40 linear scaling ratio to the Zion primary system volume. This means that the SPIT apparatus may underpredict the phenomena that are dependent on the duration of the blowdown sequence. The ZPSS analysis of the primary system blowdown indicates that approximately 40 seconds are required for equilibration in a transient sequence (P_o = 17.0 MPa). This analysis is influenced, however, by a time-dependent variation in the breach diameter, and the composition of the gases (steam and hydrogen). In order to maintain the proper time scaling, the SPIT blowdown should last approximately 2 seconds. This time interval is far greater than what is predicted from the flow analysis. Efforts are underway to improve the flowpath from the accumulator to the generator in order to overcome the present limitation.

APPENDIX C

Jet Stream Heat Loss

During the melt ejection process, the temperature of the stream is governed by the energy losses that occur during the propagation through the air. Energy is lost from the jet stream by radiative and covective heat transfer to the environment. The energy losses can be estimated by assuming the jet stream acts like a small surface totally enclosed by the surroundings at ambient temperature. The net rate of energy exchange (q) may be expressed as:

$$q = \varepsilon A_{stream} \sigma \left(T_s^4 - T_{sur}^4 \right) + h_c A_{stream} (T_s - T_{sur})$$

where:

ε = emissivity of melt

A_{stream} = surface area of jet

σ = Stefan-Boltzman constant

T_s = jet surface temperature

T_{sur} = temperature of surroundings

h_c = convective film coefficient

Performing an energy balance on the entire jet geometry shows that the energy stored is equivalent to the net energy change in the system:

$$\dot{E}_{in} - \dot{E}_{out} = E_{stored}$$

The $\dot{E}_{in}$ term represents the mass influx into the system as jet ejection continues; the $\dot{E}_{out}$ term is the loss due to radiation and convection from the surface. Calculations can be performed by defining a control volume represented by the cross-sectional area of the jet of an incremental length. In this manner, the $\dot{E}_{in}$ term can be neglected by assuming no net heat or mass transfer from adjacent control volumes. The energy loss then occurs at the outer boundaries exposed to the ambient atmosphere. Thus,

$$\dot{E}_{out} = -\dot{E}_{stored}$$

where the minus sign represents a decrease in the initial stored energy. This equation can be expressed in terms of the jet stream parameters as follows:

$$\varepsilon A_s \sigma \left(T_s^4 - T_{sur} \right) + h_c A_s \left(T_s^4 - T_{sur} \right) = - \rho c_p \left(A_{cs}\, dx \right) \frac{dT}{dt}$$

where:

dx = incremental length

ρ = density

c_p = specific heat

t = time

A_{cs} = cross-sectional area of the jet = $\frac{\pi D^2}{4}$

A_s = exposed surface area of the jet = $\pi D\, dx$,

D = the average diameter

Rearranging to remove common terms:

$$\frac{dT}{dt} = - \frac{4}{D \rho c_p} \left[\varepsilon \sigma \left(T_s^4 - T_{sur}^4 \right) + h_c \left(T_s - T_{sur} \right) \right]$$

This equation represents the change in temperature as a function of time for an incremental control volume within the melt jet. The equation assumes that, at a given point in time, the dimensions of the jet and the properties of the material are fixed. To determine the temperature of the stream as a function of time, the relationship of D, ε, c_p and h_c with time must be known.

The discussion of the previous SPIT tests (Appendix A) showed that the melt stream may diverge, so that the diameter at any point is a function of propagation distance. If the cone angle remains constant, then the dx term in the control volume scheme must decrease with propagation distance in order to maintain a constant mass. Taking this behavior into account and assuming constant density causes the area terms to take the form:

$$A_{cs} = \frac{\pi D(x)^2}{4}$$

$$A_s = \pi D(x) dx$$

the term D(x) is given as:

$$D(x) = D_o + 2(x \tan \theta)$$

where:

D_o = diameter at aperture

x = propagation distance

Θ = melt stream half-angle

For the initial portion of the stream, including the front face of the propagating jet, the exposed surface area becomes:

$$A_s' = \pi D(x)dx + \frac{\pi D(x)^2}{4}$$

The jet is then characterized using two different equations, one for the initial portion and another for the remainder of the jet. The two equations can be solved numerically using a forward differencing representation of the time derivative of the form:

Initial Stream Portion:

$$T_s^{i+1} = - \frac{\Delta t \left(4 + \frac{D(x)}{dx}\right)}{\rho c_p} \left[\varepsilon\sigma\left(T_s^{i4} - T_{sur}^4\right) + h_c \left(T_s^i - T_{sur}\right)\right] + T_s^i$$

Main Stream Portion:

$$T_s^{i+1} = - \frac{4\Delta t}{\rho c_p} \left[\varepsilon\sigma\left(T_s^{i4} - T_{sur}^4\right) h_c \left(T_s^i - T_{sur}\right)\right] + T_s^i$$

the superscripts represent the time step interval as given by:

$$t = i\Delta t: \; i = 1 \text{ to } P$$

Δt is established by:

$$\Delta t = x/PV_{jet}$$

where:

V_{jet} = velocity of the jet stream (assumed to be constant)

x = total propagation distance

P = total number of increments

The equations are then solved independently by initializing T_s, T_{sur}, ε, P, c_p, h_c and dx to give T_s^{i+1} for each case. A second dx value is then calculated using the constant control volume size and an assumed expansion angle (θ). The process continues by setting T_s^i equal to the just calculated T_s^{i+1} in the above equations and a new set of T_s^{i+1} values are obtained. The procedure is continued until the sum of the dx_i increments is equal to the total propagation distance.

A parametric study was performed using the above procedure to assess the extent of temperature loss that could be expected from the SPIT experiments. The procedure involves varying the values for emissivity, initial melt temperature, velocity, film coefficient and cone angle to determine the influence of each factor. The base case for the calculations is:

$$T_s^{i=0} = 3000 \text{ K}$$

$$T_{sur} = 300 \text{ K}$$

$$\varepsilon = 0.8$$

$$h_c = 20{,}000 \text{ W/m}^2\text{K}$$

$$\theta = 12^\circ$$

The range of values for the five variables considered is given in Table 25.

TABLE 25
Parametric Values for Jet Temperature Calculations

Variable	Initial Value	Range Low	Range High
$T_s^{i=1}$	3000 K	2500 K	3500 K
T_{sur}	300 K	300 K	
	0.8	0.5	0.8
Velocity	45 m/sec	2.8 (Gravity)	76
Film Coefficient	20,000 W/m^{2}K	1000	50,000
Cone Angle	12°	0°	20°

Calculations were made for separate situations wherein the base case was modified to exercise one variable over its entire range. The results of the calculations are given in the form of non-dimensionalized relations for graphical comparison:

Non-dimensional Temperature:

$$T^* = \frac{T_s(t) - T_{sur}}{T_s(\emptyset) - T_{sur}}$$

Non-dimensional Distance:

$$X^* = \frac{V\Delta t}{x}$$

where:

$T_s(t) = T_s \qquad i = 1 \text{ to } P$

$T_s(\emptyset) = T_s$

Figures 36 through 38 present the results of the jet-temperature calculations. Figure 36 shows the influence of the initial melt temperature. The largest energy loss is associated with the highest melt temperatures because of the larger thermal potential. The spread between the lowest and highest cases is less than 0.5%. Figure 37 shows how the melt stream emissivity affects the energy loss term. Changing the value from 0.8 (baseline) to 0.3 causes approximately a 0.5% increase in the calculated temperature ratio (compare curves 1 and 3 in Figure 37). Figure 37 also shows how the cone angle of the stream changes the ratio between surface area and volume. A larger angle will give a proportionally larger surface area and consequently enhance the loss terms. Curves 2 and 4 in Figure 37 demonstrate the calculated response to the extremes in the cone angle selection. The fourfold difference in the cone angle gives less than 0.5% change in the calculated temperature response. The results of Figure 37 suggest that the emissivity and cone angle variations are also not signficant contributors to the temperature losses of the melt jet.

The velocity range considered in Figure 38 represents the expected values extending from the lowest, gravity-driven case to the opposite situation where the generator is above the normal system operating pressure. For the parameters of the SPIT apparatus, the range of velocities varies from 2.8 m/sec (gravity only) to over 70 m/sec. The calculated temperature results given show that the gravity driven case has almost a 5% change in temperature. This behavior is caused principally by the longer time required to traverse the distance. The lower bound velocity for the pressure-driven melt in the SPIT tests, 21 m/sec, shows less than a 1% deviation in the non-dimensional temperature ratio.

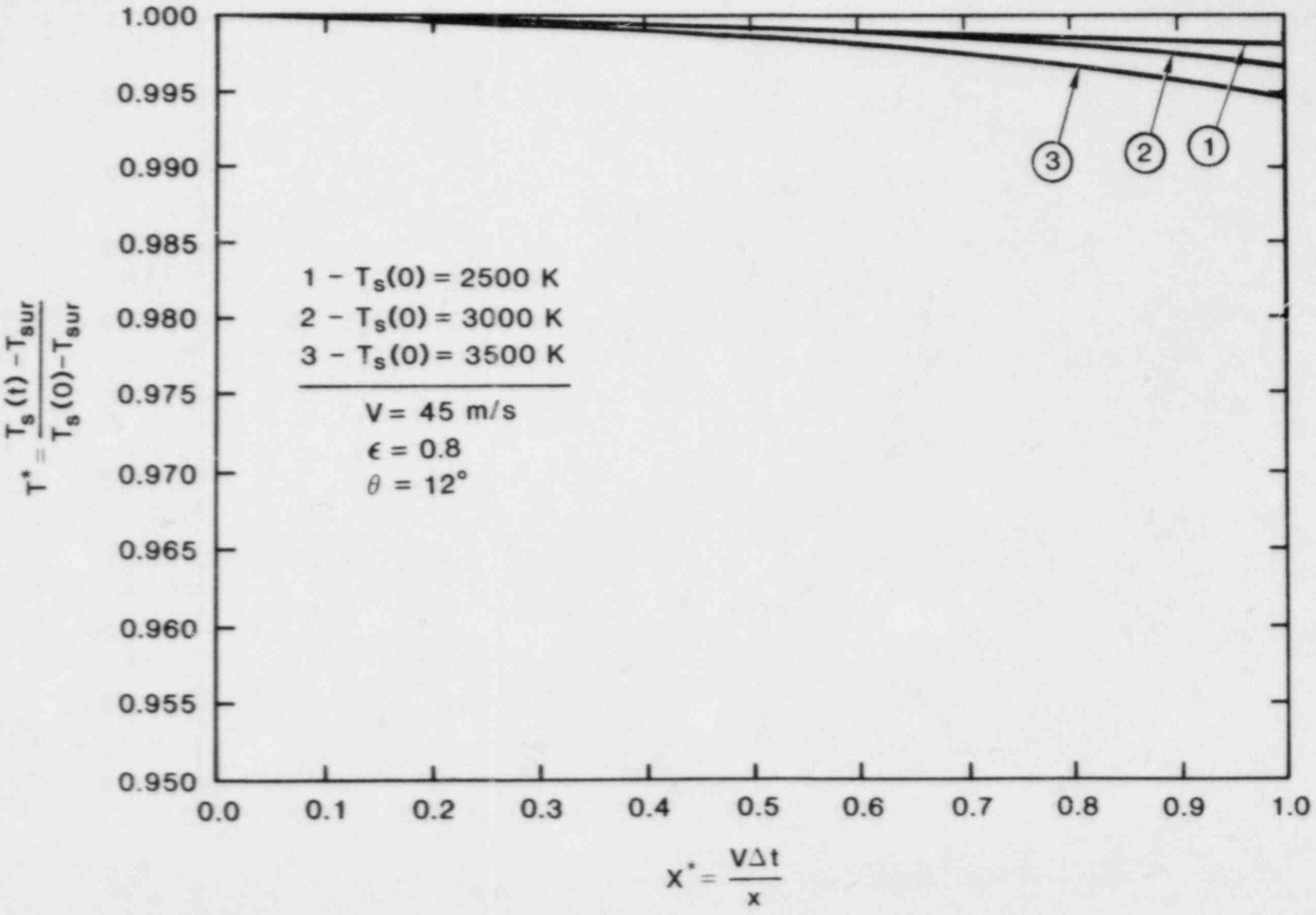

Figure 36. Calculated Jet Temperature as a Function of Initial Temperature

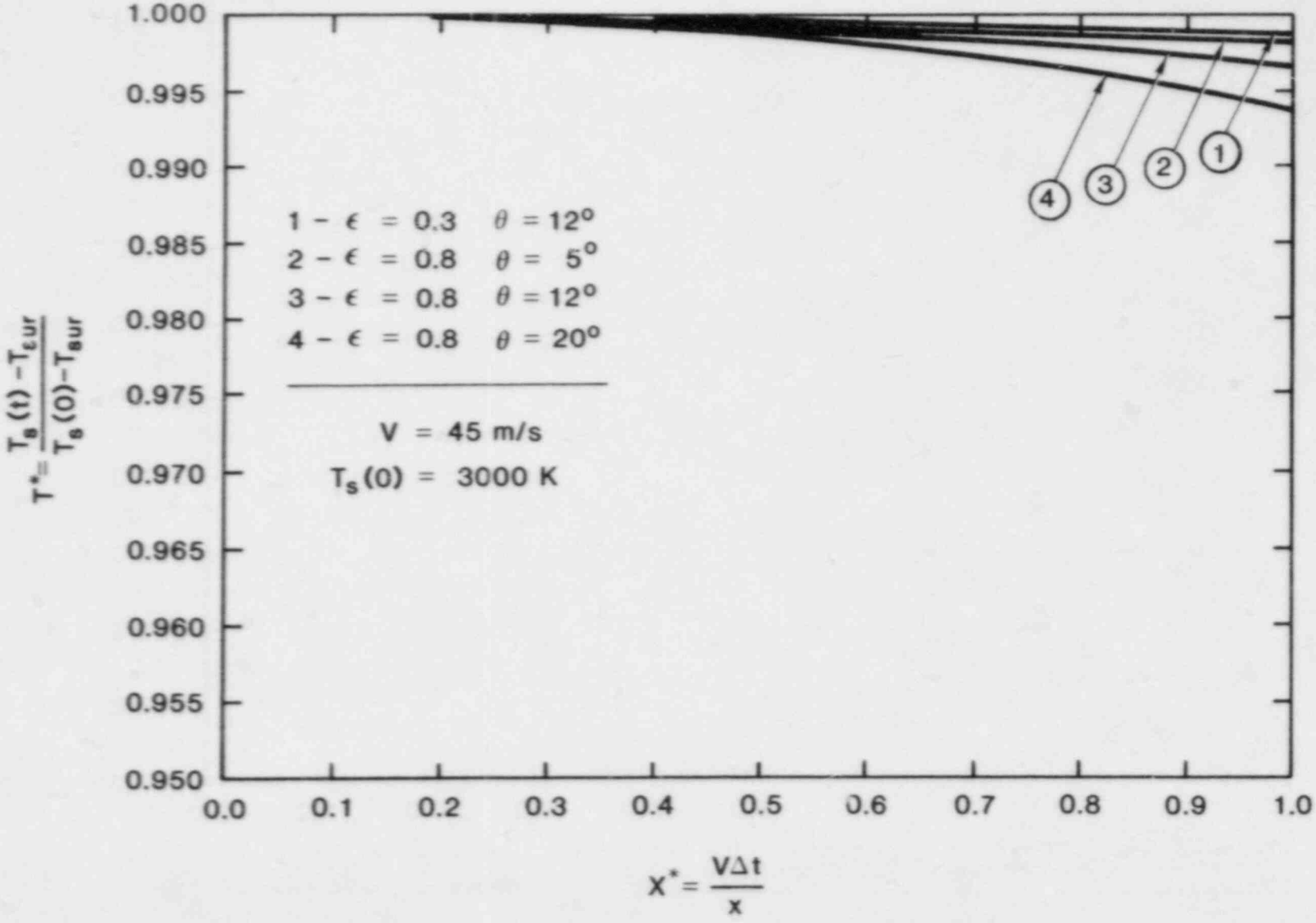

Figure 37. Calculated Melt Jet Temperature as a Function of Emissivity and Cone Angle

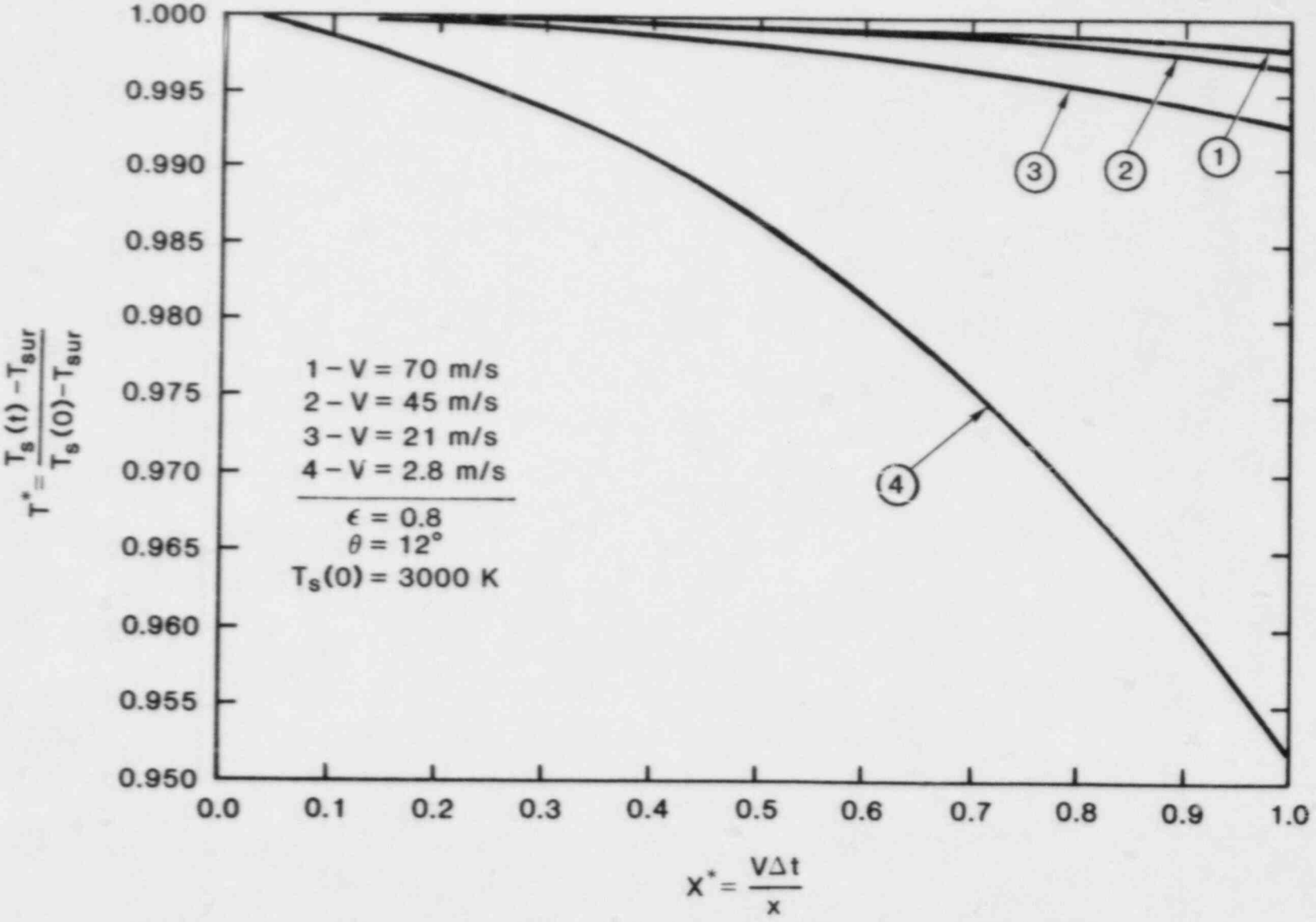

Figure 38. Calculated Melt Jet Temperature as a Function of Jet Velocity

Varying the convective film coefficient from 1000 to 50,000 w/m^2 causes less than 0.5% change in the non-dimensional temperature ratio.

The results of the energy loss calculations indicate that the jet stream temperature will not change significantly for distances up to 0.45 meter. This conclusion means that measuring the temperature at any point in the stream during the experiment will give an accurate estimate of the jet temperature.

APPENDIX D

Frequency Response of Embedded Thermocouples

The response of embedded thermocouples is dependent on the ability of the devices to follow the rapidly changing temperature history. Ref. 37 suggests that the time response of an intrinsic thermocouple can be determined from the expression:

$$t_{95} = \frac{t^* R^2}{\alpha}$$

where:

t_{95} = time required to reach 95% of the steady-state EMF

R = radius of the thermocouple junction (assumed to be spherical)

α = thermal diffusivity of substrate (graphite)

t^* = dimensionless time

The dimensionless time can be estimated by the relationship:

$$t^* = 5380\ e^{-8.52a}$$

the parameter a is a thermal property given by:

$$a = \left[1 + \left(\frac{(k \rho c)_{wire}}{(k \rho c)_{substrate}} \right)^{1/2} \right]^{-1}$$

where:

k = thermal conductivity

ρ = density

c = specific heat

The expression for t^* is accurate to a few percent in the range:

$$0.3 \leq a \leq 0.7$$

For the case of a small diameter type k thermocouple placed in a graphite calorimeter element:

$$a = 0.89$$

$$t^* = 2.7$$

$$t = 0.004 \text{ sec}$$

The result shows that the sensor will respond to a step-change in temperature in times less than the response of the recording instrumentation.

For thermocouples embedded in the concrete used to form the test cavity, the parameters are:

$$a = 0.2$$

$$t^* = 934$$

$$t = 11 \text{ sec}$$

The very low thermal conductivity of concrete increases the response of the sensor significantly. This behavior means that the thermal pulse is being conducted along the sheath of the thermocouple, away from the sensing location. The concrete also has the effect of slowing the isotherm velocity in depth, so that the seemingly long response time may be adequate for the deeper placed sensors.

APPENDIX E

Error In Melt Velocity Measurement

Melt velocity along the cavity floor and up the inclined keyway will be measured using detectors constructed to give sequential resistance changes. Average velocity can be determined using the equation:

$$V_i = \frac{x_i}{t_i}$$

where:

V_i = average velocity during the ith interval

x_i = distance between two consecutive fingers

t_i = time interval between voltage steps

The error in the velocity is then:

$$\frac{EV_i}{V_i} = \left[\left(\frac{Ex_i}{x_i} \right)^2 + \left(\frac{Et_1}{t_1} \right)^2 \right]^{1/2}$$

where EZ represents the uncertainty in parameter Z.

The error in x_i is the variation in the center-to-center spacing for an element based on the mean value (x_i) and the total number of fingers on the element (n):

$$x_i = \frac{\sum_{j=1}^{n} x_{ij}}{n}$$

$$(EX_i)^2 = \frac{(x_{i1} - x_i)^2 + (x_{i2} - x_i)^2 + \cdots + (x_{in} - x_i)^2}{n - 1}$$

$$= \sum_{j=1}^{n} \frac{(x_{ij} - x_i)^2}{n - 1}$$

The term $(Ex_i)^2$ represents the variance for a single element; the uncertainty for all sensors used in the apparatus can be based on the "pooled variance" given by the expression:

$$(Ex_i)^2_{pooled} = \frac{(n_1 - 1)\ (Ex_1)^2 + (n_2-1)\ (Ex_2) + \cdots + (n_k-1)\ (Ex_k)^2}{(n_1-1) + (n_2-1) + \cdots + (n_k - 1)}$$

where n_1, n_2, $\cdots$, (n_{k-1}), n_k represent the number of fingers on each sensor. If all the sensors have the same number of elements (k), then the above equation reduces to:

$$(Ex_i)^2_{pooled} = \frac{(Ex_1)^2 + (Ex_2)^2 + \cdots + (Ex_k)^2}{k}$$

Evaluating the above equations for an arbitrary selection of 6 sensors (k = 6) yields the following numerical values:

$$(Ex_i)^2_{pooled} = 1.384 \times 10^{-4} \text{ cm}$$

$$(x_i)^2_{mean} = \sum_{i=1}^{6} (x_i)^2 = 0.5116 \text{ cm}$$

and

$$\left(\frac{Ex_i}{x_i}\right)^2 = \frac{(Ex_i)^2_{pooled}}{(x_i)^2_{mean}} = 2.706 \times 10^{-4}$$

The uncertainty in the time interval can be found as the absolute error for a given time increment or as a percentage of full scale. It is convenient to assume the latter, so that the uncertainty in a given velocity is applicable at all velocities. For the device employed to record the velocity sensor output, the uncertainty is given as $\pm$ 1 units for the entire sample period. Therefore, for 4096 samples (number of time samples for the instrument) in a period:

$$\left(\frac{Et_i}{t_i}\right)^2 = \left(\frac{1}{4096}\right)^2 = 5.96 \times 10^{-8}$$

Substituting the results of the calculations above into the equation for the error in velocity:

$$\frac{EV_i}{V_i} = \left[\left(2.706 \times 10^{-4} + 5.96 \times 10^{-8}\right)\right]^{1/2}$$

$$= 1.64 \times 10^{-2} = 1.64\%$$

The above analysis indicates that the melt velocity determined by the sensors is reasonably accurate. The assumption must be made that the melt is well behaved and that shorting of the elements occur in consistent, sequential manner.

REFERENCES

1. Rasmussen, N., et al., Reactor Safety Study: An Assessment of Accident Risks in U.S. Commercial Nuclear Power Plants, WASH-1400, NUREG-75/014, Washington, D.C., 1975.

2. Lewis, H., et al., Risk Assessment Review Group Report to the U.S. Nuclear Regulatory Commission, NUREG/CR-0400, 1978.

3. Rogovin, M., Three Mile Island: A Report to the Commissioners and the Public, NUREG/CR-1250, 1979.

4. Zion Probabilistic Safety Study, Commonwealth Edison Co., Chicago, IL., 1981.

5. Tarbell, W.W., and Bradley, D.R., Sustained Concrete Attack by Low-Temperature, Fragmented Core Debris, SAND82-2476, NUREG/CR-3024, Sandia National Laboratories, Albuquerque, NM (in press).

6. Powers, D., and Arellano, F., Large-Scale, Transient Tests of the Interaction of Molten Steel with Concrete, SAND81-1753, NUREG/CR-2282, Sandia National Laboratories, Albuquerque, NM, January 1982.

7. Perinic, D., et al., Concrete Crucible Tests with Thermite Melts, NRC Translation 669, Nuclear Research Center, Karlsruhe, KFK 2572, July 1979.

8. Wooten, R.O., and Avci, H.I., MARCH Code Description and User's Manual, NUREG/CR-1711 (BMI-2064), Battelle Columbus Laboratories, October, 1980.

9. Bordelon, F.M., and Murphy, E.T., WCAP-8327 Containment Pressure Analysis Code (COCO), July 1974.

10. Final Safety Analysis Report for the Zion Nuclear Power Station.

11. Catton, I., Memorandum to Jim Meyer, USNRC, February 2, 1982.

12. Blander, M., et al., Solubility of Noble Gases in Molten Flourides II. In the LiF-NaF-KF Eutetic Mixture, J. Phys. Chem. 63 1154 (1959).

13. Pilch, M., et al., Acceleration Induced Fragmentation of Liquid Drops, NUREG/CR-2247, Univ. of Virginia, 1981.

14. Sitharamayya, S., and Subba Raje, K., Canad. J. Chem. Eng. 47 365, 1969.

REFERENCES (Continued)

15. Knief, R.A., Nuclear Energy Technology Hemisphere Publishing Corp, McGraw-Hill Book Co, 1981.

16. Powers, D.A., and Arellano, F.E., Direct Observation of Melt Behavior During High Temperature Melt/Concrete Interaction, SAND81-1754, NUREG/CR-2283, Sandia National Laboratories, Albuquerque, NM, January, 1982.

17. Incropera, F., and DeWitt, D., Fundamentals of Heat Transfer, John Wiley & Sons, Inc., New York, NY, 1981.

18. Blackwell, F.B., User's Manual for the Sandia One-Dimensional Direct and Inverse Thermal (SODDIT) Code, Sandia National Laboratories. Albuquerque, NM, (in press).

19. Doebelin, E.O., Measurement Systems: Application and Design, McGraw-Hill Book Co., New York, NY, 1966.

20. Abramovich, G.N., The Theory of Turbulent Jets, translation by Scripta Technica, The MIT press, Cambridge, MA, 1963.

21. Radiography in Modern Industry, 4th ed., Eastman-Kodak Co., Rochester, NY, 1980.

22. Beck, J.V., Non-Linear Estimation Applied to the Non-Linear Inverse Heat Conduction Problem, Int'l. Heat Mass Transfer (13) 703, 1970.

23. Powers, D.A. and Arrellano, F.E., Erosion of Steel Structures by High-Temperature. SAND81-1755, NUREG/CR-2284, Sandia National Laboratories, Albuquerque, NM, June 1983.

24. Touloukian, Y.S., et al., Thermophysical Properties of Matter, IFI/Plenum, Vol. 13, 1977.

25. Hameed, R. et al. " A New Rotating Course Particle Sampler", Aerosol Soi and Tech., Vol 2 (1983).

26. Powers, D.A. and Brockmann, J.E., Release of Fission Products and Generation of Aerosols Outside the Primary System, Appendix C of BMI 2104, Vol I, Battelle Columbus Laboratories, (In Press).

27. Strategy of Experimentation - Revised Edition, E.I. duPont de Nemours & Co., Inc., Wilmington , DE., October, 1975.

28. Bradley, R.H., Witte, L.C. "Explosive Interaction of Molten Metals Injected Into Water" Nuclear Science and Engineering 48, 1972.

REFERENCES (Continued)

29. Chou, P.E., and Hopkins, A.K., Eds., Dynamic Response of Materials to Intense Impulsive Loading, published by Air Force Materials Laboratory, Wright-Patterson AFB, Ohio, August 1972.

30. Handbook of Chemistry and Physics, 46th ed., Chemical Rubber Co., Cleveland, OH, 1965.

31. Sutherland, H.J., and Hagen, S., Acoustically Measured Penetration Profiles for a Molten Metallic Pool into River-Stone Concrete, SAND82-0676, NUREG/CR-2634, Sandia National Laboratories, Albuquerque, NM, December 1982.

32. Buxton, D., and Benedick, W.B., Steam Explosion Efficiency Studies, SAND79-1399, NUREG/CR-0947, Sandia National Laboratories, Albuquerque, NM, November, 1979.

33. Beckwith, T.G., et al., Mechanical Measurements, 3rd ed., Addison-Wesley Publishing Co., Inc. Reading, MA, 1982.

34. Moffat, R.J., "How to Specify Thermocouple Response", ISA Journal, 203, June, 1955.

35. Mark's Standard Handbook for Mechanical Engineers, 8th ed., McGraw-Hill Book Co., 1979.

36. Taylor, Sir Geoffrey, The Instability of Liquid Surfaces When Accelerated In A Direction Perpendicular to Their Planes, I, Proc. Royal Society, 201 (1950) 192-6.

37. Keltner, N.R. and Bickle, L.W., "Intrinsic Thermocouple Measurement Errors", presented at ASME-AICHE Heat Transfer Conference, St. Louis, MO, Aug. 1976.

DISTRIBUTION:

Division of Technical Information
and Document Control
NRC Distribution Contractor
U. S. Nuclear Regulatory Commission
15700 Crabbs Branch Way
Rockville, MD 20850
250 copies for R7

U.S. Nuclear Regulatory Commission (16)
Office of Nuclear Regulatory Research
Washington, DC 20555
Attn: O. E. B ssett
B. S. Burson
R. T. Curtis
C. N. Kelber
J. Larkins
T. Lee (5)
M. Silberberg
R. W. Wright
T. Walker
W. Pasedaq
M. Jankowski

U.S. Nuclear Regulatory Commission (4)
Office of Nuclear Regulatory Regulation
Washington, DC 20555
Attn: L. G. Hulman
P. Easky
J. Rosenthal
J. Mitchell

U.S. Department of Energy (2)
Albuquerque Operations Office
P. O. Box 5400
Albuquerque, NM 87185
Attn: J. R. Roeder, Director
Operational Safety Division
D. K. Nowlin, Director
Special Programs Division
For: C. B. Quinn
D. Plymale

U.S. Department of Energy
Office of Nuclear Safety Coordination
Washington, DC 20545
Attn: R. W. Barber

Electric Power Research Institute
3412 Hillview Avenue
Palo Alto, CA 94303
Attn: R. Vogel
R. Sehgal

Professor T. Theofanous
Purdue University
School of Engineering
West Lafayette, IN 47907

Dr. R. Henry
Fauske & Associates
16W070 West 83rd Street
Burr-Ridge, IL 60521

M. L. Corradini
Nuclear Engineering Dept.
University of Wisconsin
Madison, WI 53706

I. Catton
UCLA
Nuclear Energy Laboratory
405 Hilgard Avenue
Los Angeles, CA 90024

Brookhaven National Laboratory (4)
Department of Nuclear Energy
Building 820
Upton, NY 11973
Attn: R. A. Bari
T. Pratt
G. Greene
T. Ginsberg

Professor R. Seale
Department of Nuclear Engineering
University of Arizona
Tucson, AZ 85721

Oak Ridge National Laboratory (2)
P. O. Box Y
Oak Ridge, TN 37830
Attn: T. Kress
S. Hodge

K. Holtzclaw
General Electric - San Jose
Mail Code 682
175 Kurtner Avenue
San Jose, CA 95125

Argonne National Laboratory
9700 S. Cass Avenue
Argonne, IL 60439
Attn: D. Pedersen

Cathy Anderson
Nuclear Safety Oversight Commission
1133 15th St., NW
Room 307
Washington, DC 20005

Battelle Columbus Laboratory (3)
505 King Avenue
Columbus, OH 43201
Attn: P. Cybulskis
R. Denning
J. Gieseke

J. E. Antill
Berkeley Nuclear Laboratory
Berkeley GL 139 PB
Gluocestershire
United Kingdom

W. G. Cunliffe
Bldg. 396
British Nuclear Fuels, Ltd.
Springfields Works
Salwick, Preston
Lancs
United Kingdom

Reactor Development Division (4)
UKAEA - Atomic Energy Establishment
Winfrith, Dorchester
Dorset
United Kingdom
Attn: R. G. Tyror, Head
T. Briggs
R. Potter
A. Nichols

Projekt Nucleare Sicherheit (3)
Kerforschungszentrum Karlsruhe
Postfach 3640
75 Karlsruhe
Federal Republic of Germany
Attn: J. P. Hoseman
Albrecht
H. H. Rininsland

Mr. G. Petrangeli
Direzione Centrale della Srcurezza
Nucleare e della Protezione Sanitaria (DISP)
Entre Nazionnle Energie Alternative (ENEA)
Vrale Regina Margherita, 125
Casella Postale N. 2358
I-00100 Roma A.D., ITALY

Dr. K. J. Brinkman
Reactor Centrum Nederland
P.^. Box 1
1755 ZG Petten
THE NETHERLANDS

Mr. H. B^iriot, Chief
Department LWR Fuel
Belgonucleaire
Rue de Champde Mars. 25
B-1050 BRUSSELS, BELGIUM

Dr. S. Saito
Japan Atomic Energy Research Institute
Takai Research Establishment
Tokai-Mura, Naku-Gun
Ibaraki-ken
JAPAN

Wang Lu
TVA
400 Commerce, W9C157-CK
Knoxville, TN 37902

M. Fontana
Director, IDCOR Program
Technology for Energy, Inc.
P. O. Box 22996
10770 Dutchtown Rd.
Knoxville, TN 37922

H. J. Teague (3)
UKAEA
Safety and Reliability Directorate
Wigshaw Lane
Culcheth
Warrington, WA3 4NE
United Kingdom

Dr. Fran Reusenbach
Gesellschaft fur Reaktorsicherheit (GRS mbH)
Postfach 101650
Glockengasse 2
5000 Koeln 1
Federal Republic of Germany

S. J. Niemczyk
Union of Concerned Scientists
1346 Connecticut Avenue, N.W.
S.1101
Washington, DC 20036

M. Jankowski
IAEA
Division of Nuclear Reactor Safety
Wagranerstrasse 5
P. O. Box 100
A/1400 Vienna, Austria

3141 C. M. Ostrander (5)
3151 W. L. Garner (1)
6000 E. H. B^ckner

6400 A. W. Snyder
6410 J. W. Hickman
6420 J. V. Walker
6420 J. B. Rivard
6421 T. R. Schmidt
6422 D. A. Powers (5)
6422 F. E. Arellano
6422 J. E. Brockmann (5)
6422 R. M. Elrick
6422 E. R. Copus
6422 J. E. Gronager
6422 T. M. Kerley
6422 D. A. Lucero
6422 A. L. Ouellette, Jr.
6422 E. Randich
6422 A. R. Taig
6422 W. W. Tarbell (5)
6423 P. S. Pickard
6425 D. R. Bradley
6425 W. J. Camp
6425 M. Pilch (5)
6425 A. Suo Anttila
6425 W. Frid
6427 M. Berman
6430 N. R. Ortiz
6440 D. A. Dahlgren
6442 W. A. Von Riesemann
6449 K. D. Bergeron
6450 J. A. Reuscher
6454 G. L. Cano
7530 T. B. Lane
7537 N. R. Keltner
7537 T. Y. Chu
7537 R. U. Acton
7537 B. F. Blackwell
8424 M. A. Pound

NRC FORM 335 (2-84) NRCM 1102, 3201, 3202

U.S. NUCLEAR REGULATORY COMMISSION

BIBLIOGRAPHIC DATA SHEET

SEE INSTRUCTIONS ON THE REVERSE

1. REPORT NUMBER (Assigned by TIDC, add Vol. No., if any)
NUREG/CR-3025
SAND82-2477

2. TITLE AND SUBTITLE
High Pressure Melt Streaming (HIPS) Program Plan

3. LEAVE BLANK

4. DATE REPORT COMPLETED
MONTH: APRIL YEAR: 1984

5. AUTHOR(S)
W. W. Tarbell
J. E. Brockmann
M. Pilch

6. DATE REPORT ISSUED
MONTH: JUNE YEAR: 1984

7. PERFORMING ORGANIZATION NAME AND MAILING ADDRESS (Include Zip Code)
Sandia National Laboratories
P. O. Box 5800
Albuquerque, NM 87185

8. PROJECT/TASK/WORK UNIT NUMBER

9. FIN OR GRANT NUMBER
NRC Fin. No. A1218

10. SPONSORING ORGANIZATION NAME AND MAILING ADDRESS (Include Zip Code)
Division of Accident Evaluation
Severe Accident Assessment Branch
U. S. Nuclear Regulatory Commission
Washington, D. C. 20555

11a. TYPE OF REPORT
R7

b. PERIOD COVERED (Inclusive dates)

12. SUPPLEMENTARY NOTES

13. ABSTRACT (200 words or less)

The Zion Probabilistic Safety Study (ZPSS) envisions accident sequences that could lead to failure of the reactor vessel while the primary system is pressurized. The resulting ejection of molten core material into the reactor cavity followed by the blowdown of steam and hydrogen is shown to cause the debris to enter into the containment region.

The High Pressure Melt Streaming (HIPS) program has been developed to provide an experimental and analytical investigation of the scenario described above. One-tenth linear scale models of the Zion cavity region will be used to investigate the debris dispersal phenomena. Smaller-scale experiments (SPIT-tests) are also used to study high-velocity jets, jet-water interactions, and 1/20th scale cavity geometries. Both matrices are developed using a factorial design approach.

The document describes certain aspects of the ZPSS ex-vessel phenomena, the experimental matrices, test equipment, and instrumentation, and the program's analytical efforts. Preliminary data from SPIT testing are included.

14. DOCUMENT ANALYSIS - a. KEYWORDS/DESCRIPTORS
High Pressure Ejection/Thermite/Jets/Aerosol Generation/ Reactor Safety/Debris Dispersal/PRA

b. IDENTIFIERS/OPEN-ENDED TERMS

15. AVAILABILITY STATEMENT
unlimited

16. SECURITY CLASSIFICATION
(This page) unclassified
(This report) unclassified

17. NUMBER OF PAGES

18. PRICE

☆U.S. GOVERNMENT PRINTING OFFICE: 1984—576-035 / 4389